Study of the temporal distribution of X-ray flares from the supermassive black hole Sgr A*

Auteur : Finociety, Benjamin
Promoteur(s) : Mossoux, Enmanuelle
Faculté : Faculté des Sciences
Diplôme : Master en sciences spatiales, à finalité approfondie
Année académique : 2018-2019
URI/URL : http://hdl.handle.net/2268.2/6993

Study of the temporal distribution of X-ray flares from the supermassive black hole Sgr A*

Master thesis presented by:
Benjamin FINOCIETY

to be graduated in:
Master in Space Sciences

Academic year 2018-2019
Defense on July, 2019

Master thesis supervised by:
Mrs. MOSSOUX Enmanuelle

Members of jury:
M. GROSSO Nicolas
M. HUTSEMEKERS Damien
Mrs. MOSSOUX Enmanuelle
M. RAUW Gregor

University of Liège, Faculty of Sciences
Department of Astrophysics, Geophysics and Oceanography

Acknowledgements

First of all, I would like to thank a lot my supervisor, Enmanuelle Mossoux. She was very free to help me, especially with coding issues, and to discuss about the methods or results. She also took time to read carefully this work and help me to improve the contents. She gave me a good view of observational studies by teaching me the way to collect and reduce data from X-ray space telescopes and then to analyse them with dedicated tools and software such as XSPEC or DS9. I also would like to thank her for giving me the possibility to participate to a study about a supermassive black hole which is an object really fascinating.

I also thank Nicolas Grosso, Damien Hutsemékers and Gregor Rauw for having accepted to be part of the Board of Examiners and for taking time to read my Master Thesis.

I do not want to forget to thank my family for supporting my choices concerning my studies with this "double degree" between my engineering school, École Centrale de Nantes, and the University of Liège and also for encouraging me to pursue with a PhD in astrophysics.

Finally, I thank my friends and Sylvie that showed enthusiasm to understand what I did during this Master thesis, to read parts of my work and with who it was always a pleasure to discuss about all kind of things to make some breaks and to spend time with. I think about Alexis, Grégoire, Vincent met during these two last years but also about some friends in France such as Yassine, François, Adrien and Dylan.

Contents

List of Figures

List of Tables

List of Acronyms

ACIS	Advanced CCD Imaging Spectrometer (CXO)
ALMA	Atacama Large Millimeter Array
ARF	Ancillary Response File
CALDB	Chandra Calibration Database
CCD	Charge Coupled Device
CCF	Current Calibration File
CIAO	Chandra Interactive Analysis of Observations
CND	Circumnuclear accretion Disk
CXO	Chandra X-Ray Observatory
DSO	Dusty S-cluster Object
EPIC	European Photon Imaging Camera (XMM-Newton)
FWHM	Full Width at Half Maximum
GTI	Good Time Interval
IC	Inverse Compton
MJD	Modified Julian Date
MOS	Metal Oxide Semi-conductor (XMM-Newton)
NIR	Near Infrared
NRF	Non-thermal Radio Filaments
ODF	Observation Data File
PPS	Pipeline Processing Subsystem
PSF	Point Spread Function
QPO	Quasi Periodic-Oscillation
RIAF	Radiatively Inefficient Accretion Flow
RMF	Redistribution Matrix File
SAS	Science Analysis System
SED	Spectral Energy Distribution
Sgr	Sagittarius
SGR	Soft Gamma Repeater
S/R	Signal-to-Noise Ratio
SNR	Supernova Remnant
SSC	Synchrotron Self-Compton
UTC	Coordinated Universal Time
VLA	Very Large Array
VLBA	Very Long Base Array
WR	Wolf-Rayet
XMM	X-ray Multi-Mirror telescope
XRT	X-Ray Telescope (Swift)

Chapter 1

Overview of the Galactic Centre and Sgr A*

In this first part, I present the object of study of this Master Thesis. I begin by introducing the Milky Way, the Galactic Centre and the close environment of the supermassive black hole Sgr A* in Section 1.1. Then, in Section 1.2, I describe the physical characteristics of Sgr A*. In Section 1.3, I present the quiescent state of the black hole in an electromagnetic point of view, while in Section 1.4 I focus on the variable emission, introducing the notion of flares. Section 1.5 presents the object named DSO/G2, which may have an influence on the activity of Sgr A* and two transients X-ray sources which have an impact on the several observations at the beginning of the year 2016. Finally, in Section 1.6, I set the context of my Master Thesis and develop its interest.

1.1 The Milky Way and its centre

1.1.1 Global properties of the Milky Way

Our solar system is embedded in a barred spiral galaxy named the Milky Way. The Milky Way is composed of several constituents: the galactic halo, the galactic disk and the galactic bulge which includes the Galactic Centre (Figure 1.1). The halo is a large spheroidal structure around the disk and the bulge containing globular clusters, dwarves galaxies and the oldest stars in the galaxy.

The disk is a flat structure which contains about 90% of the visible matter. This part has a diameter of about 100 kly (30 kpc) for a thickness of about 1 kly (300 pc; Amôres et al. 2017) but a recent work suggests that the disk could be actually much larger and could have a diameter of at least 52 kpc (López-Corredoira et al., 2018). The disk is generally thought to consist of four major arms and two smaller arms. One of them is the Orion arm enclosing the solar system, at a distance of about 8 kpc from the centre of the galaxy. The arms are mainly star formation regions (Russeil, 2003) composed of hydrogen (HI, HII and H_2) and helium. Some metals can be found as the interstellar medium is enriched by supernovae explosions.

The bulge is the central part of the galaxy. It has a radius of about 10 kly (3 kpc) and contains about 5% of the visible mass, mostly old stars. It is difficult to observe because of the presence of dust in the galactic plane (see subsection 1.1.3).

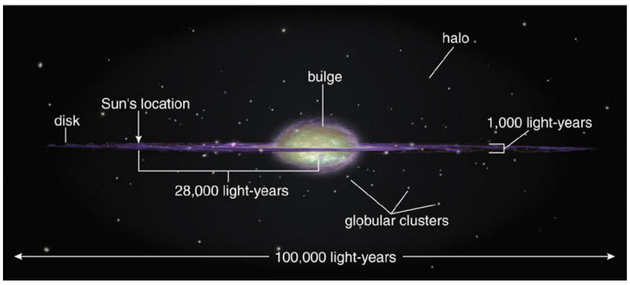

Figure 1.1: Schematic view of the Milky Way.

1.1.2 A brief history

At the end of the 1910's, Harlow Shapley studied the distances and distribution of 69 globular clusters. He deduced that the Sun is not at the centre of our galaxy. He estimated that the Galactic Centre is located in the Sagittarius (Sgr) constellation at a distance of about 13 kpc from the Sun (Shapley, 1918).

In 1930, Robert Trumpler compared the diameter distance and the photometric distance of globular clusters. Since the two distances were different, he deduced that the interstellar medium contains a huge quantity of matter such as free atoms or dust grains which absorb the light. Moreover, this matter is concentrated in the galactic plane which makes it impossible the observation of the Galactic Centre (Trumpler, 1930).

Few time after, in 1932, the engineer Karl Jansky was performing experiments on electronic noise in the atmosphere at the Holmdel Radio Laboratories of Bell Telephone Laboratories. He discovered an electromagnetic wave which seems to come from a fixed point in the Sagittarius constellation (Jansky, 1933). It was actually the first observation of the Galactic Centre.

In 1959, Frank Drake made the first radio map of the Galactic Centre. This map covered a $5° \times 5°$ area in which he distinguished bright regions corresponding to the galactic nucleus (Drake, 1959).

Balick & Brown (1974) detected a strong radio emission in a region centred on the galactic nucleus and of a radius equal to one parsec. They associated this to a compact radio source at the centre of the galaxy. This source was then named Sgr A* by Brown (1982) when he studied the jets coming from the source in order to distinguish it from the other components in the Galactic Centre. The named is composed of two parts. The first one is "Sagittarius A" (Sgr A) since the location of the source is in the Sagittarius A region. The second is the asterisk which was used to indicate that Sgr A* is an exciting source for the cluster of HII regions around it, just like the asterisk is used to show the excited state of an atom.

1.1.3 The extinction towards the Galactic Centre

It is not easy to observe the Galactic Centre. Indeed, the dust in the interstellar medium is responsible of extinction, which is a combination of scattering and absorption of light. Extinction causes a decrease of the observed flux of distant objects according to the following formula:

$$A_\lambda = -2.5\ \log_{10}\left(\frac{I(\lambda)}{I_0(\lambda)}\right) = 1.086\,\tau_{\mathrm{ext}}(\lambda) \tag{1.1}$$

Where A_λ is the extinction in magnitude at the wavelength λ, $I(\lambda)$ and $I_0(\lambda)$ are the observed intensity and emitted intensity at the wavelength λ, respectively. $\tau_{\mathrm{ext}}(\lambda)$ is the optical depth at the wavelength λ. From the Equation (1.1), the ratio between the number of received photons and the number of emitted photons is $10^{-A_\lambda/2.5}$.

In the visible, it is impossible to observe the centre of our galaxy. The extinction at 550nm (A_{V}) is about 30 mag (Becklin & Neugebauer 1968; Rieke et al. 1989). That is to say that we receive one photon for 10^{12} emitted. Thus, the pathway between us and the Galactic Centre is nearly totally opaque to visible light.

Infrared light is not so readily obscured by dust as visible light. Indeed, Fritz et al. (2011) have computed the extinction in different bands in the infrared. For the H-band (1.64 μm), they found that towards Sgr A*, $A_{\mathrm{H}} = 4.21 \pm 0.10$. About one photon is observed in this band for hundred emitted. They also showed that in the infrared, the longer the wavelength, the smaller the extinction.

For long wavelengths, that is to say in submillimetre and radio ranges, the galaxy is nearly transparent to all photons and that is why the Galactic Centre was first detected in these domains. Hence, the source seems to emit more photons at these wavelengths, this is called the interstellar reddening.

Although the short wavelengths suffer from the extinction, the Galactic Centre becomes again accessible at X-ray wavelengths, since they can penetrate the gas and dust that block the visible light. For that, energies higher than about 1 keV are required (Morris & Serabyn, 1996).

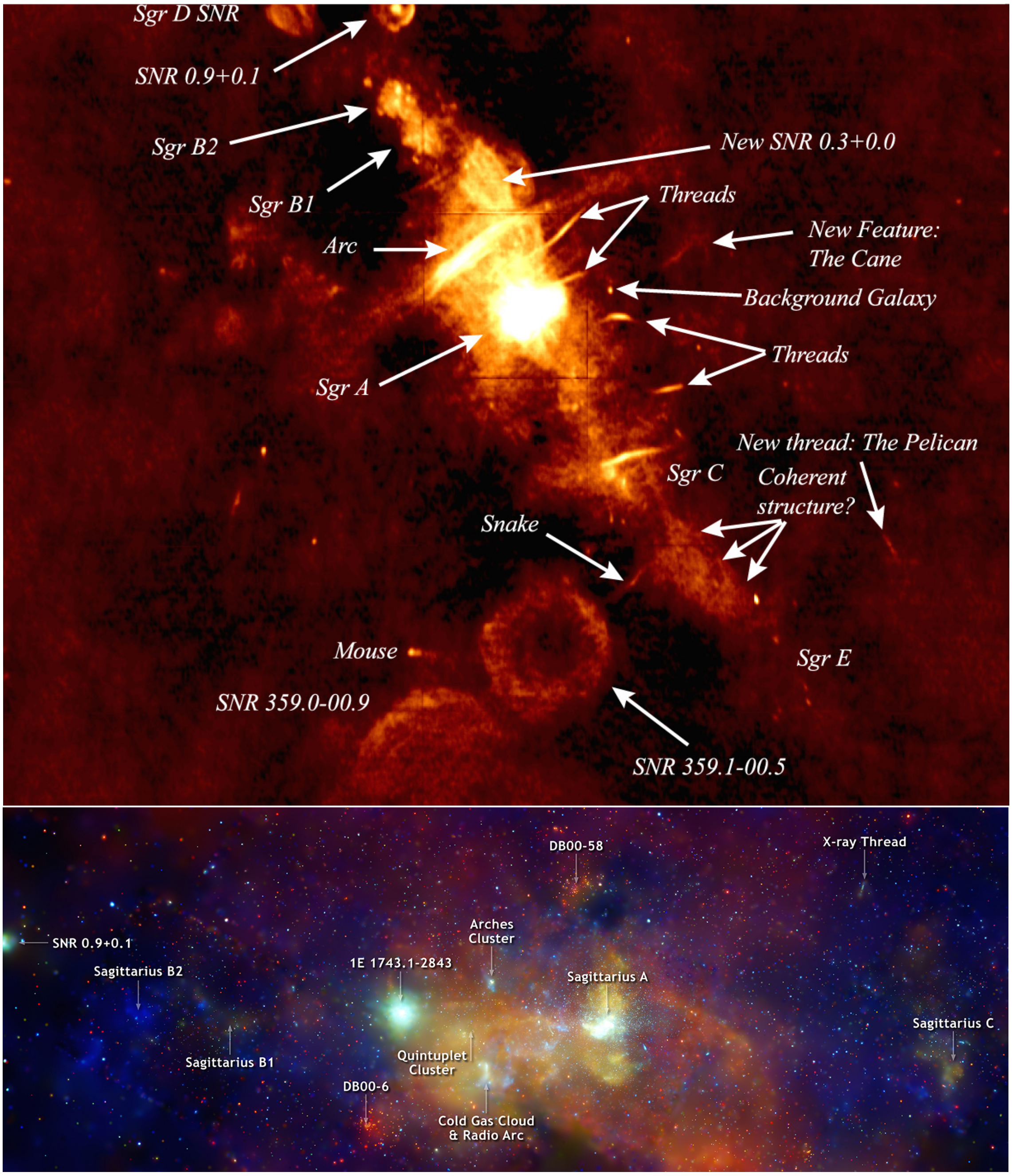

Figure 1.2: *Top panel*: Radio image (λ = 90cm) of the Galactic Centre (Kassim et al., 1999). *Bottom panel*: Chandra image, where red is for 1-3 kev, green for 3-5 keV and blue for 5-8 keV (credits: NASA/CXC/U-Mass/D. Wang et al.). We have to note that the images are not at the same scale and not aligned, but we can easily find the same features to compare.

1.1.4 The close environment of Sgr A*

One of the most clear view of the Galactic Centre was made by Kassim et al. (1999) with the Very Large Array (VLA) in the radio domain at 330 MHz over an area of 2°× 2°(top panel of Figure 1.2). On this image it is possible to see many structures. The brightest one is Sgr A, which hosts the supermassive black hole (SMBH) Sgr A*. Several regions of star formation, or molecular clouds are also visible such as Sgr B2, Sgr C and Sgr D. In addition, many non-thermal emission sources are present, such as supernova remnants (SNR), pulsars or non-thermal radio filaments (NRFs). It is thought that the NRFs are produced by the synchrotron emission

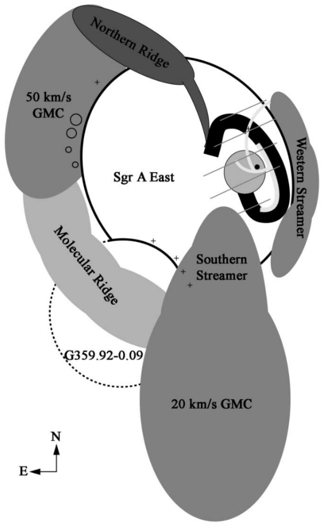

Figure 1.3: Schematic view of the Sgr A complex as seen in the plane of the sky (Herrnstein & Ho, 2005). For the details of this figure, see subsection 1.1.4.

due to the motion of relativistic electrons around the magnetic field perpendicular to the galactic plane, and then trace the large-scale magnetic field in the central region of the Galaxy (Yusef-Zadeh et al., 1984). Other filaments were discovered afterwards with low inclination with respect to the galactic plane, which does not support the previous interpretation. Instead, models of jets created by embedded young stars in star forming regions were proposed to explain the origin of the NRFs (Yusef-Zadeh et al. 2004; Yusef-Zadeh & Königl 2004).

Depending on the wavelength at which we observe the Galactic Centre, we do not see exactly the same components. Figure 1.2 shows two illustrative images of the Galactic Centre. The top panel image has been made in radio while the bottom panel image has been made by the space telescope Chandra in X-rays between 1 and 8 keV. On each image, one can clearly see Sgr A, which is one of the brightest components. However, in X-rays the molecular clouds Sgr B1, Sgr B2 and Sgr C are fainter than in radio. Clusters of stars are more luminous in X-rays, such as the Quintuplet or the Arches clusters as well as the centre of supernovas, such as SNR 0.9+0.1 which is very bright in X-rays.

We will now focus on the Sgr A complex which hosts our privileged target, the SMBH Sgr A* (black dot in Figure 1.3). One part is called Sgr A West (light grey strips in Figure 1.3). It is composed of arcs or arms of ionized gaz, located around the Galactic Centre, which have a kind of spiral distribution (Ekers et al. 1983; Lo & Claussen 1983). This gas is surrounded by a ring of dense neutral gas which could correspond to a circumnuclear accretion disk (CND; backward-C shape in Figure 1.3) that injects a part of the interstellar medium into the central region (Güsten et al., 1987). It has been recently proved that the CND acts as a barrier for the central plasma (Mossoux & Eckart, 2018).

Sgr A East (black ellipse in Figure 1.3) is the largest part of the Sgr A complex. It has a shell-type structure with synchrotron emission typical of supernova remnants (Ekers et al., 1983). It has thus been postulated that Sgr A East is a supernova remnant with a long lifetime, that is to say that the explosion might have occurred $10^4 - 10^5$ years ago (Ekers et al., 1983). Maeda et al. (2002) determined that Sgr A East could originate from a type II supernova of a 13-20 $M_\odot$ star dating from 10^4 years. Another SNR named G359.92-0.09 (dotted circle in Figure 1.3) interacts with Sgr A East leading to the kind of bended line at the south east of the latter region (Coil & Ho, 2000).

1.1.5 The distance to Sgr A* and its location

Determining the distance between the Sun and Sgr A*, named R_0 hereafter, is an important challenge because it may be used afterwards to determine other distances. Shapley (1918) evaluated this distance at 13 kpc thanks to his study of globular clusters.

However, in the second part of the 20th century, several studies indicated that the value given by Harlow

Shapley was overestimated. Oort & Plaut (1975) analysed the distribution of RR Lyrae variables close to the Galactic Centre and obtained $R_0 = 8.7 \pm 0.6$ kpc. Another kind of variable stars important for the estimation of distances is the cepheids. These stars are very bright and could be observed at large distances. Their period is a function of their luminosity and this property is used to get the distance. Thanks to that, Caldwell et al. (1992) found that the distance to the Galactic Centre should be $R_0 = 8.5 \pm 0.5$ kpc. From the analyse of globular clusters, it is possible to have an estimation of the distance between the Sun and Sgr A* by assuming that the distribution of the clusters is symmetrical (around the Galactic Centre) and then by finding where the density is the highest. With this method, de Vaucouleurs & Buta (1978), as well as Frenk & White (1982), found $R_0 = 7.0$ kpc and $R_0 = 6.8 \pm 0.8$ kpc, respectively.

Is is also possible to determine the distance to the Galactic Centre using the luminosity of the observed targets. For instance, Ebisuzaki et al. (1984) analysed some X-ray bursts near the Galactic Centre, that they assume to be neutrons stars. Thanks to the luminosity, they derived the distance $R_0 = 7$ kpc. Planetary nebulae luminosity can also be used as an estimator of distances. Indeed, it exists a maximal luminosity of the planetary nebulae corresponding to an absolute magnitude in the [OIII] forbidden line at 500.7 nm. By observing a large sample of planetary nebulae, Dopita et al. (1992) determined $R_0 = 7.6 \pm 0.7$ kpc.

Reid (1993) made a census of the different estimations of R_0 at that time, including the examples cited above among many others (see Table 1.1). He then found that, on average, R_0 can be estimated at 8.0 ± 0.5 kpc. This result is well consistent with more recent values. Using astrometric and spectrocopic measurements of the star with the shortest and best known orbit around Sgr A* (S2 also known as S0-2) with adaptive optics in the near-infrared domain, Eisenhauer et al. (2003) derived $R_0 = 7.94 \pm 0.42$ kpc. Even more recently, the fit of the orbit of S2 including the effects of special and general relativity allows to constrain the distance R_0 to 8.127 ± 0.031 kpc (Gravity Collaboration et al., 2018).

Through a survey with the Very Long Base Array (VLBA) it has been possible to determine the coordinates of Sgr A* in radio: RA(J2000) = $17^h45^m40\overset{s}{.}036$ and Dec(J2000) = $-29°00'28\overset{''}{.}17$ (Petrov et al., 2011). Finally, the determination of the proper motion of Sgr A* shows that it is most likely at rest at the dynamical centre of the Galaxy (Reid et al. 1999; Reid & Brunthaler 2004). This proper motion is equal to $-18 \pm 7\,\mathrm{km\,s^{-1}}$ in the galactic plane and $-0.4 \pm 0.9\,\mathrm{km\,s^{-1}}$ in the perpendicular direction (Reid & Brunthaler, 2004).

Table 1.1: Table of the different estimations of the distance R_0 between the Sun and Sgr A*, grouped by methods (Reid, 1993).

Calibration group	$R_o \pm \sigma_{stat}$ (kpc)
Primary Measurements:	
H_2O Proper Motions	7.2 ± 0.7
Scaled by M_v(RR) = 0.70 mag:	
Globular Clusters	8.0 ± 0.8
RR Lyrae Variables	8.0 ± 0.5
Red Giants	7.9 ± 1.0
Galaxy Modelling	8.7 ± 0.6
Scaled by $\Theta_o = 220$ km s^{-1}:	
Sgr A* Proper Motions	7.7 ± 0.9
OH/IR Stars	8.1 ± 1.1
Using Oort's Constants:	
Nearby Stars	8.9 ± 1.0
Disk Modelling	9.0 ± 1.0
OB Star Calibration:	
OB Stars	9.1 ± 1.0
HI & HII Regions	8.1 ± 0.5
Scaled by LMC $(m-M)_o = 18.47$ mag:	
Cepheids	8.0 ± 0.5
Miras	7.9 ± 1.0
Eddington Luminosity (1.4 $M_\odot$):	
X-ray Sources	7.4 ± 1.0
Miscellaneous:	
Planetary Nebulae	7.6 ± 0.7
M–S Turn-off	9.2 ± 2.2

Notes: This list was established in 1993 and thus does not include more recent studies that can use accurate numerical methods.

1.2 The physical features of the supermassive black hole Sgr A*

1.2.1 The mass of Sgr A*

Genzel et al. (1996) studied the radial velocities of 223 stars in order to determine the mass distribution in the centre of the Galaxy. They found evidence that a compact dark mass concentration centred on Sgr A* exists. The derived mass ranges in $2.5 - 3.2 \times 10^6\,M_\odot$. Still using the radial velocities and proper motion of stars, Genzel et al. (1997) derived a new value for the central mass of $(2.61 \pm 0.35) \times 10^6\,M_\odot$. Since this mass is concentrated inside the smallest stellar orbit they concluded that there is a supermassive black hole at the centre of the Milky Way. Ghez et al. (1998) confirmed this mass studying the proper motions of 90 stars from a central cluster centred on Sgr A*. Indeed, they estimated that the Galaxy hosts a supermassive black hole with a mass of $(2.6 \pm 0.2) \times 10^6\,M_\odot$.

More recently, it has been established that the mass of Sgr A* was in fact underestimated. Indeed, thanks to the astrometric (1995-2007) and radial velocities measurements (2000-2007) of the star S2 Ghez et al. (2008) could give a new estimation: $(4.1\ \pm 0.6) \times 10^6\,M_\odot$.

Gillessen et al. (2009a) studied the orbit of 28 stars around Sgr A*, with among them the star S2. They found that all the orbits were consistent with the presence of a central mass of $(4.31 \pm 0.06|_{stat} \pm 0.36|_{R_0}) \times 10^6\,M_\odot$. The result was then updated to a new value $(4.30 \pm 0.20|_{stat} \pm 0.30|_{sys}) \times 10^6\,M_\odot$ (Gillessen et al., 2009b). S0-102 is a star orbiting Sgr A* with a short period of 11.5 years, which enables Meyer et al. (2012) to constrain the mass to $(4.1 \pm 0.4) \times 10^6\,M_\odot$.

By analysing the speckles on the images and adaptive optics data between 1995 and 2013, especially concerning the two stars S0-38 and S2, Boehle et al. (2016) improved the determination of the SMBH mass: $(4.02 \pm 0.16 \pm 0.04) \times 10^6\,M_\odot$. However, with the fit of the orbit of the star S2 after the detection of gravitational redshift, taking into account special and general relativity effects, it appears that the mass of Sgr A* would be of $(4.106\ \pm\ 0.034) \times 10^6\,M_\odot$ (Gravity Collaboration et al., 2018). In addition, this study improves the features of the orbit of S2 (Figure 1.4), with an eccentricity equals to 0.88473 ± 0.00018, an inclination of $133.817° \pm 0.093°$ and an orbital period of 16.052 years.

All of these studies show evidences that Sgr A* is actually a supermassive black hole.

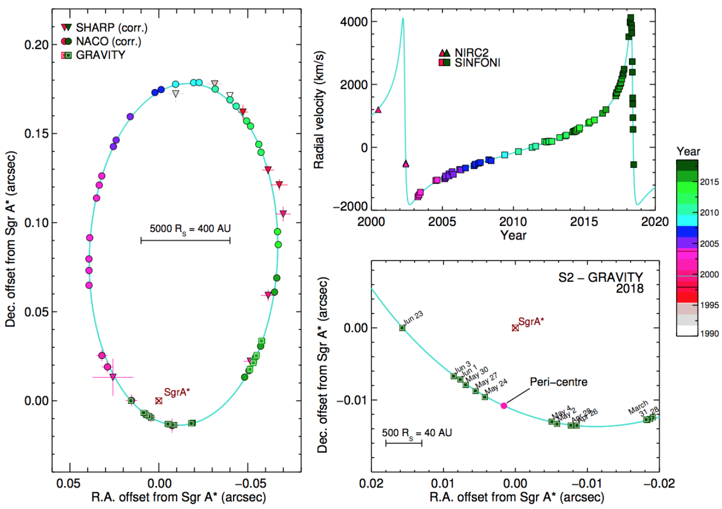

Figure 1.4: Orbit of the star S2 from observations between 1992 and 2018 (taken from Gravity Collaboration et al. 2018). The cyan curve represents the best fit including the effects of special and general relativity. *Left panel*: Projection of the orbit of S2, with the cross indicating the position of Sgr A*. *Upper right panel*: Radial velocity of the star as a function of time. *Bottom right panel*: Zoom on the pericentre of the orbit.

1.2.2 Some scales about Sgr A*

Here is a review of some typical length scales which can characterize the black holes and give ideas about their size.

The Schwarzschild radius

The size of a black hole can be defined by its Schwarzschild radius (Schwarzschild, 1916). It corresponds to the event horizon of the black hole which is the distance at which the escape velocity is equal to the speed of light in the vacuum. Inside this radius, all matter and photons cannot escape from the gravitational field of the black hole. If one considers a particle, with a mass m and a velocity equal to c, the speed of light in vacuum, one can express the Schwarzschild radius R_S by equalizing its kinetic energy and its potential energy. One also defines the gravitational radius R_g as the half of R_S.

$$R_S = \frac{2GM}{c^2}\,\mathrm{m} \approx 0.02\,\frac{M}{10^6\,\mathrm{M}_\odot}\,\mathrm{au} \tag{1.2}$$

$$R_g = \frac{GM}{c^2} = \frac{1}{2}R_S \tag{1.3}$$

Where G is the gravitational constant, M the mass of the black hole, c the speed of light in vacuum and $\mathrm{M}_\odot$ the solar mass. In the case of Sgr A*, we assume a mass of $4 \times 10^6\,\mathrm{M}_\odot$ according to the previous subsection. We find that $R_S = 11.8 \times 10^6$ km ≈ 0.08 au and $R_g = 5.9 \times 10^6$ km ≈ 0.04 au.

The Bondi radius

The Bondi radius R_B (Bondi, 1952) corresponds to the distance where the matter begins to be accreted around the black hole. It is expressed by:

$$R_B = \frac{2GM}{c_s^2} \tag{1.4}$$

Where c_s is the speed of sound in the ambient environment given by $c_s = \sqrt{\gamma kT/\mu m_H}$ with γ the adiabatic index, k the Boltzmann constant, T the temperature, μ the mean atomic weight of the gas and m_H the mass of the hydrogen atom. Assuming that $\gamma = 5/3$ and $\mu = 0.70$, Baganoff et al. (2003) found that $c_s \approx 550\,\mathrm{km\,s^{-1}}$. With a mass of $4 \times 10^6\,M_\odot$ and this speed of sound, one has: $R_B = 0.11$ pc ($2''.8$ or $\sim 10^5\,R_S$).

1.3 The quiescent state of Sgr A*

1.3.1 The energy production mechanism

The gas around Sgr A* has a non-zero angular momentum. Due to that, it orbits around the black hole instead of falling radially towards it. Since the matter is spinning around Sgr A*, the friction between the particles tends to concentrate the gas into a disk.

As the gravitational forces acting on the particles are larger than the friction, we consider that the gas has a keplerian motion. Hence, the disk is in differential rotation which creates heat. The friction then dissipates the kinetic energy of the particles which begin to spiral towards the black hole, increasing the friction and the temperature. Thus, the closer to the black hole the more energetic are the emitted radiations.

In the following, I will use the expression "emission (of radiation) from Sgr A*" instead of saying the emission coming from the matter accreted onto the supermassive black hole.

1.3.2 The Eddington limit

Accretion happens if the gravitational force F_{grav} acting on the matter is larger than the radiation force F_{rad} exerting by the photons through radiation pressure. At the limit where the two forces are equal, we can express the maximum luminosity possible for the black hole which is called Eddington luminosity (Equation (1.5)). We assume that the distribution of matter is spherically symmetric. In addition, we can assume that the matter is principally composed of ionised hydrogen atoms, thus free electrons can cause Thomson scattering. This lead to an appoximation of the mass scattering coefficient $\kappa_\nu \approx \sigma_T/m_H$ where σ_T is the Thomson cross section for electrons and m_H the mass of an hydrogen atom.[1] We thus have:

$$F_{rad} = \frac{L\,\sigma_T}{4\pi r^2 c m_H} \qquad\qquad F_{grav} = \frac{G\,M\,m}{r^2}$$

$$L_{Edd} = \frac{4\pi G c m_p}{\sigma_T} M \approx 1.26 \times 10^{38} \frac{M}{M_\odot} \,\text{erg/s} \approx 3.3 \times 10^4 \frac{M}{M_\odot} L_\odot \tag{1.5}$$

Where, M is the mass of the black hole, r is the distance between the centre of the black hole and the element of mass m, m_p the proton mass, c the speed of light in vacuum and G the gravitational constant. One has to note that m_H has been replaced by m_p in Equation (1.5) since the mass of the proton is much higher than the mass of the electron. The numerical application for Sgr A* gives an Eddington limit of $L_{Edd} \approx 5 \times 10^{44}$ erg/s $\approx 1.3 \times 10^{11}\, L_\odot$, assuming a mass of $4 \times 10^6\, M_\odot$.

The bolometric luminosity is the luminosity obtained considering the totality of the electromagnetic spectrum. The one of Sgr A* has been evaluated to be about 10^{36} erg s^{-1} (Narayan et al. 1998; Yuan et al. 2003). This gives $L_{\rm Bol} \sim 10^{-9}\, L_{\rm Edd}$ (see for e.g. Nowak et al. 2012). With these values, it has been concluded that Sgr A* is a very low-luminosity black hole. If we compare with nearby low-luminosity active galactic nuclei, the ratio between the bolometric luminosity and the Eddington limit for Sgr A* is few orders of magnitude lower (Ho, 1999).

1.3.3 Feeding the black hole

The mass can be converted into energy through the expression $E_{emitted} = \eta M_{acc} c^2$, where η is a coefficient corresponding to the efficiency (equals to one if all the mass is converted) and M_{acc} the mass accreted by the black hole. The luminosity can be linked to the energy by the formula: $L = dE_{emitted}/dt = \eta \dot{M}_{acc} c^2$.
Using the Eddington limit for the luminosity in the previous expression, we obtain the maximum accretion rate possible named Eddington accretion rate, which corresponds to the rate needed to maintain the Eddington luminosity. Setting $\eta = 0.1$ we obtain:

$$\dot{M}_{Edd} = \frac{L_{Edd}}{\eta c^2} \approx 2.2 M_8\, M_\odot/\text{year} \tag{1.6}$$

Where M_8 is the black hole mass expressed in units of $10^8\, M_\odot$. For Sgr A*, we have $\dot{M}_{Edd} = 8.8 \times 10^{-2}\, M_\odot$/year.

In the central region of the galaxy, Wolf-Rayet (WR) stars have been detected in infrared (Paumard et al. 2001, 2006). The wind of these WR stars are thought to be the sources of the matter accreted onto Sgr A*. Purely 3D hydrodynamical simulations, not taking into account the effect of magnetic field, based on 30 orbiting WR stars as sources, allow Ressler et al. (2018) to determine the accretion rate as a function of radius. They extrapolate their results to find an accretion rate of $3.4 \times 10^{-8}\, M_\odot\, \text{yr}^{-1}$ at the horizon of Sgr A*. This is in agreement with radio polarization measurements giving an accretion rate between $2 \times 10^{-9}\, M_\odot\, \text{yr}^{-1}$ and $2 \times 10^{-7} M_\odot\, \text{yr}^{-1}$, depending on the configuration of the magnetic field (Marrone et al., 2007), as well as with previous modelling of accretion around Sgr A* leading to an estimation of about $10^{-8}\, M_\odot\, \text{yr}^1$ (Shcherbakov & Baganoff 2010; Ressler et al. 2017). All these results imply that the accretion rate of Sgr A* is about 10^{-7} times the Eddington accretion rate.

[1] Expressions are obtained from the equations found in Rybicki & Lightman (1979). The radiation force is expressed by unit mass.

1.3.4 Explaining the low luminosity of Sgr A*

Two parameters can impact the luminosity of Sgr A*. The first one is the fraction of matter accreted onto the black hole. As explained in the previous part, it is thought that massive stars in the central region of the galaxy lose mass through their winds which is accreted onto Sgr A*. Simulations have shown that if these winds composed of ionised gas have high angular momentum, the accretion rate will be greatly reduced (Yusef-Zadeh & Wardle, 2010).

The second parameter is the radiative efficiency in the accretion disk. Several models have been examined to explain the emission from Sgr A*. A model of relativistic jets is able to fit the spectrum in the radio domain as well as in X-rays (Falcke & Markoff, 2000). Another model proposed by Blandford & Begelman (1999) is an inflow-outflow model in which the accreted gas could have enough energy to escape from the gravitational potential.

Yuan et al. (2003) explore radiatively inefficient accretion flows (RIAFs) models which correspond to a situation where the accretion rate is reduced at large radii and where the electrons which have a lower temperature allow to radiate away only a very few gravitational potential energy of the gas because of the lack of equilibrium with it. This kind of models seems to be consistent with measurements done thanks to the Atacama Large Millimeter Array (ALMA) (Bower et al., 2018).

A model commonly used is an advection-dominated accretion flow as proposed by Narayan et al. (1998). This kind of flows is characterised by the fact that only a small part of the energy produced through dissipation (due to viscosity), stored and transported towards the centre is radiated. This type of models has already been proposed by Narayan et al. (1995) to fit the spectrum of Sgr A*. In this model, advection was not considered as a perturbation but as a dominant part of the physics of the flow. They succeeded to fit the spectrum from radio to X-ray wavelengths, and found that only 0.1% of the energy was radiated behind R_S (before reaching the event horizon), and thus could reach us, while the other 99.9% fell into the black hole and cannot escape anymore.

The last proposition is linked to the time delays measured between peaks of emission at different radio wavelengths. Yusef-Zadeh & Wardle (2010) report that these delays can be explained by the expansion of hot plasma which is initially optically thick. But, as it expands, the density of electrons decreases and the plasma becomes progressively optically thin at longer wavelengths. This can be seen as an application of a model proposed by van der Laan (1966) to predict the variability of the radio spectrum of extragalactic sources. However, if the expansion of the blob of plasma is subrelativistic, particles cannot escape from the attraction of Sgr A*. On the contrary, if the expansion is relativistic then jets could appear and reduce the accretion onto the black hole (Maitra et al., 2009).

1.3.5 The multiwavelength quiescent emission

It is possible to characterize the energy emitted by the quiescent state of Sgr A* at different wavelengths or frequencies. For that purpose, the spectral index α is used, defined as $S_\nu \propto \nu^\alpha$, where ν is the frequency and S_ν the flux emitted at this frequency. Another quantity is the photon index Γ defined by $N(E) \propto E^{-\Gamma}$, where N(E) is the number of relativistic electrons with an energy between E and E+dE . The two indexes are linked by the relation $\alpha = (1 - \Gamma)/2$. From observations, the spectral energy distribution (SED) can be constructed (Figure 1.5).

In the radio domain (centimetre-millimetre wavelengths) the spectral index has been estimated by using the data from the Very Large Array (VLA) or ALMA, between 1 and 100 GHz especially. Combining data from both radio telescopes, $\alpha = 0.41 \pm 0.03$ while using only the VLA ones, $\alpha = 0.50 \pm 0.07$ (Brinkerink et al., 2015). These results are consistent with those of Loeb & Waxman (2007) and suggest that the emission in this domain is due to synchrotron radiation coming from optically thick plasma (see the short-dashed line in Figure 1.5).

The bulk of the emission from Sgr A* is emitted at submillimetre wavelength, producing what is called the submillimetre peak. The maximum observed luminosity at 350 μm is about 4.6×10^{35} erg s^{-1} (Serabyn et al., 1997). At low radio frequencies, the spectrum is flattened by the presence of non-thermal electrons (dash-dotted line in Figure 1.5) which contain about 1% of the steady state electron energy as suggested by Özel et al. (2000). This part of the spectrum can also been reproduced by models based on isothermal jets coupled to a

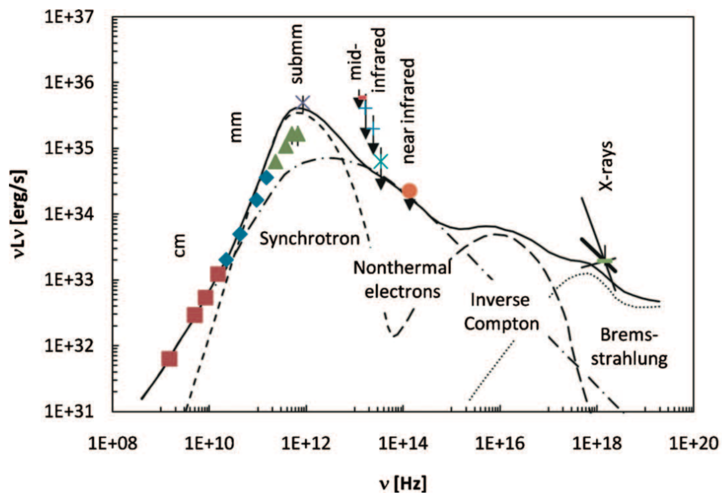

Figure 1.5: Quiescent emission from Sgr A* from radio to X-rays (Genzel et al. 2010 and references therein for the coloured symbols). The coloured symbols represents measurements from radio to mid-infrared. The dashed line shows the submillimetre peak produced by synchrotron emission due to relativistic thermal electrons. It also shows the contribution from possible inverse Compton upscattering at higher energies. The dash-dotted line corresponds to the contribution from non thermal electrons. The dotted line represents the bremsstrahlung emission from hot plasma. The black line is a model of the quiescent emission based on a RIAF model.

two-temperatures accretion flow (Mościbrodzka & Falcke, 2013). Between the submillimetre peak and the mid infrared, the SED drops steeply.

In near infrared, the source is faint and thus difficult to detect. Nevertheless, Sgr A* is detectable between 1.5 and 5 μm. In particular, it appears that the upper limit of the luminosity at 2.2 μm is lower than 2×10^{34} erg s^{-1} (Genzel et al., 2010). A value of -0.64 ± 0.1 for the spectral index in the L-H band has been derived by Witzel et al. (2014a), which is typical of an optically thin synchrotron radiation. Another feature of Sgr A* is that it appears continuously variable in the near infrared.

In X-rays, Sgr A* appears really faint. The luminosity of its steady state has been estimated at about 2×10^{33} erg s^{-1} in the 2-10 keV range (Baganoff et al. 2001, 2003). Above 10 keV, Zhang et al. (2017) found an upper limit for the luminosity $L_{10-79\,\mathrm{keV}} \leq (2.9 \pm 0.2) \times 10^{34}$ erg s^{-1}. The spectrum of the X-ray quiescent state could be fitted either by an absorbed power law model or a thermal bremsstrahlung depending on the observed region. The emission integrated over a region of radius corresponding to the RIAF (about 1" or $2.4 \times 10^5\, R_g$) can be fitted by a thermal bremsstrahlung (Yuan et al., 2003). However, the X-ray emission close to the black hole (distances from Sgr A* lower than $10^3\, R_g$) can be represented by a single power law of spectral index equal to 4.8 (Roberts et al., 2017) which indicates that the bremsstrahlung emission does not dominate in this region. This result is consistent with a recent study from Ma et al. (2019) which deals with the determination of the SED in the same region.

A steady emission at very high energy γ-rays was detected from the direction of the Galactic Centre but it is difficult to disentangle the source which can be Sgr A* as well as Sgr A East for example (Aharonian et al. 2004; Albert et al. 2006).

1.4 The electromagnetic activity of Sgr A*

Occasionally, the emission observed from Sgr A* is enhanced with respect to its quiescent state. These phenomena are visible at all wavelengths from radio to X-rays: they are called flares. In addition, it appears that the variability of the source increases with the frequency (see Figure 1.6).

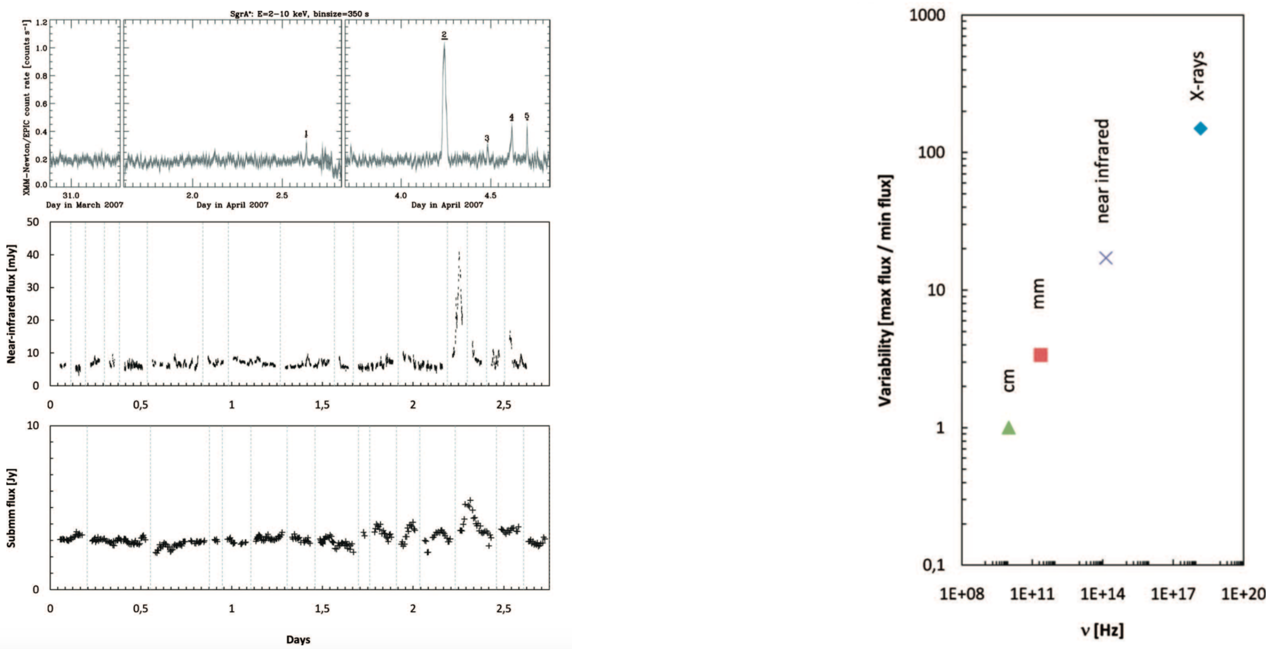

Figure 1.6: *Left panel*: Three light curves of Sgr A*, in the X-ray (top panel), the near-infrared (middle panel) and submillimitre domain (bottom panel) showing the variability of the source (from Genzel et al. 2010). The three light curves do not correspond to the same periods of observations, and none is continuous. These curves show that the variations are more important at high frequencies (X-rays) than at low frequencies (submillimetre), with different time scales. *Right panel*: Maximum variability observed across the electromagnetic spectrum (from Genzel et al. 2010). At cm/mm wavelengths, the ratio between the maximum flux and the minimum one is about the unity while it can reach more than 100 for X-rays.

1.4.1 Variability in radio, submillimetre and near-infrared domains

Since the 1980's, it is known that Sgr A* is variable in the radio domain (Brown & Lo, 1982). The variability of the emission decreases with increasing wavelength. Observations at 2.3 GHz and 8.3 GHz allow Falcke (1999) to derive rms deviation of flux density of 2.5% and 6% respectively. Later, other studies have investigated additional frequencies in radio which showed that the rms variation was of 13%, 16% and 21% at 15 GHz, 23 GHz and 43 GHz, respectively (Herrnstein et al., 2004). For wavelengths between 7 and 20 mm, the amplitude variation can reach 30-40% without periodicity detected (Macquart & Bower, 2006). In the submillimetre regime, the bursts can peak up to a factor two above the quiescent level (Yusef-Zadeh et al. 2006; Trap et al. 2011). It is possible to say if an increase of flux is a flare in these domains only if a counterpart in X-rays or NIR is detected. The typical duration of the flares in submillimetre/radio is about 2 to 2.5 hours (Li et al., 2009) (see the bottom panel in Figure 1.6 for an example of light curve showing a submillimetre flare)

Genzel et al. (2003) reported the observation of several flares in the NIR domain, especially in the H-band (1.65 μm) and K_S-band (2.16 μm) above a quiescent state showing variability. However, statistical studies of the variability of the NIR emission from Sgr A* reveal that the notions of quiescent state and flares in this domain is quite meaningless (Witzel et al. 2012; Meyer et al. 2014) because the emission from Sgr A* is continuously variable in NIR (Do et al., 2009). We nevertheless refer to the bursts of emission in the NIR regime as flares, that can be seen four times per day, with a typical duration of 100 minutes (Shahzamanian et al., 2015) (see middle panel of Figure 1.6 for an example of light curve). They can reach very high value, up to 27 times the median level (Dodds-Eden et al., 2011). Although some observations seem to reveal quasi-periodic oscillation of about 17 min (QPO; Genzel et al. 2003), the variability of Sgr A* in NIR can be modelled by random processes such as red noise which rule out these QPO in a statistical way (Do et al., 2009). Dodds-Eden et al. (2011) showed that the flux distribution can be represented by a lognormal curve at low flux density ($\leq$ 8 mJy) with an additional tail for higher fluxes. This property has been exploited by Genzel et al. (2010) who propose an explanation about the detection of QPO. For them, at low density flux, we detect the red noise like emission while the tail at higher flux could present periodic structures that have been detected by other authors (for instance, Genzel et al. 2003, Trippe et al. 2007). A last property of the NIR flares is that they are polarized. For flares with fluxes above 5 mJy, the degree of polarization lies in the range $10 - 30\%$ with a prefered angle of polarization of $13° \pm 15°$ (Shahzamanian et al., 2015), which could be associated to jets or winds directions of the accretion disk around Sgr A*.

1.4.2 Features of X-ray variability

Sgr A* is also variable in the X-ray domain. We can distinguish the quiescent level from the flares at these wavelengths (see top panel of Figure 1.6 for an example of light curve). Moreover, X-rays are the regime where the flares are the most powerful, that is to say that the maximum variation can be much higher than in NIR or radio (see right panel of Figure 1.6).

The first detection of flares in X-rays was done by Baganoff et al. (2001) who reported the observation of luminosity about 45 times higher than the quiescent one. Since then, lots of other flaring episodes were observed (for instance Porquet et al. 2003, 2008; Nowak et al. 2012; Neilsen et al. 2013; Degenaar et al. 2013, 2015; Mossoux et al. 2015b, 2016; Capellupo et al. 2017; Zhang et al. 2017).

During a campaign with Chandra in 2012, called the X-ray Visionary Project (XVP), Neilsen et al. (2013) detected 39 flares from Sgr A*. They then made analyses which allow to determine some interesting information:

- First, flares last between few minutes up to more than two hours.
- Flares with a luminosity larger than 10^{34} erg s^{-1} have a frequency of $1.1^{+0.2}_{-0.1}$ flares per day. The brightest ones, with a luminosity above 10^{35} erg s^{-1}, are less frequent and occur every 11.5 days. Degenaar et al. (2013) also show that the brightest flares occur every 10-20 days thanks to a Swift campaign.
- About half of the detected flares has a luminosity equal to more than ten times the quiescent state luminosity.
- The brightest flare reaches a luminosity of $\sim 5 \times 10^{35}$ erg s^{-1}, which represents about 250 times the quiescent X-ray emission.
- The luminosity and the energy (fluence) distribution can be described by a power law in the form dN/dL $\propto L^{-1.9\pm0.4}$ and dN/dF $\propto F^{-1.5\pm0.2}$, respectively. Yuan et al. (2018) made statistics on the X-ray flares detected with Chandra between 1999 and 2012. They derived a consistent power law index for the fluence distribution of $-1.73^{+0.20}_{-0.19}$.
- The X-ray emission from Sgr A* can be divided into two parts. The first one is the quiescent emission. The second one is composed of resolved or unresolved flares which are superimposed onto the former part. They estimated that about 10% of the quiescent emission is actually due to unresolved weak flares. Neilsen et al. (2015) went further and suggested that the quiescent state can be modelled by a Poisson distribution while the variable part could be represented by a power law.

However, more recently Mossoux & Grosso (2017) derived new values, especially on the flaring frequency based on the detection of 107 flares. By processing the data obtained between 1999 and November 2015 thanks to three telescopes (XMM-Newton, Chandra and Swift), the intrinsic flaring rate was estimated at 3.0 ± 0.3 flares per day, regardless the luminosity of the flares. In addtion, it appears through this study that the flaring rate of the less luminous and the less energetic flares decreased from mid 2013 while the flaring rate of the most luminous and most energetic ones increased from 2014 August 31. For instance, the frequency of the less luminous flares went from 2.3 ± 0.3 flares per day to 0.7 ± 0.3 while those of the more luminous ones went from 1.6 ± 0.2 flares per day to 5.0 ± 1.5 (see Figure 1.7 for illustration). This work confirms the tendency already mentioned by Ponti et al. (2015) about the increase of the bright flaring rate.

Generally, the spectrum of the flares can be modelled by a power law with a photon index $\Gamma \approx 2$ and a hydrogen column density $N_H \approx 14.3 \times 10^{22}$ cm^{-2} (Porquet et al. 2003, 2008; Nowak et al. 2012; Degenaar et al. 2013; Ponti et al. 2017; Zhang et al. 2017; Yuan et al. 2018).

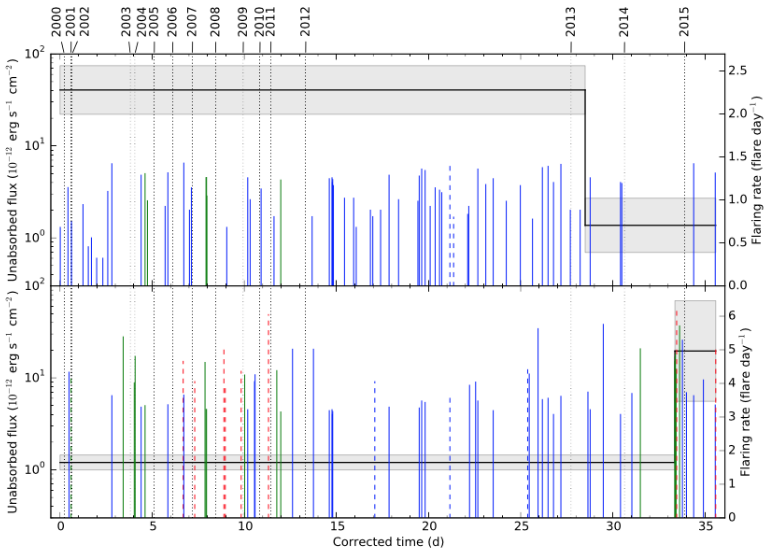

Figure 1.7: X-ray flaring rate from Sgr A* between 1999 and 2015 (Mossoux & Grosso, 2017). The flaring rates were computed using a Bayesian blocks algorithm. These blocks are shown by the thick black lines, with their uncertainty in grey. *Top panel*: Flaring rate obtained for the less luminous flares (flux lower than $6.5 \times 10^{-12}\,\mathrm{erg\,s^{-1}\,cm^{-2}}$). It appears a decay in mid 2013, going from 2.3 flares per day to 0.7 flares per day. *Bottom panel*: Flaring rate obtained for the more luminous flares (flux larger than $4 \times 10^{-12}\,\mathrm{erg\,s^{-1}\,cm^{-2}}$). It appears an increase in mid 2014, going from 1.6 flares per day to 5.0 flares per day.

1.4.3 Mechanisms at the origin of NIR/X-ray flares

It could be interesting to focus on the external mechanisms that can lead to eruptions before exploring the radiative mechanisms producing the emission of radiation.

The first physical mechanism that can explain the origin of the flares is linked to the magnetic field. Indeed, during a magnetic reconnection, the dissipated energy can be transferred to the electrons which will be accelerated to produce a flare via one of the mechanisms described in the following subsection (Yuan et al. 2003; Dodds-Eden et al. 2010; Ponti et al. 2017).

Another possible way to have eruptions is the creation of a plasma wave turbulence in the hot accretion flow, that can be due to an increase in the accretion rate or a magnetic reconnection (Liu et al., 2004).

Tagger & Melia (2006) propose that a Rossby wave instability can produce the NIR/X-ray flares. In this hypothesis, a spot of plasma merges with the accretion disk around the black hole. This perturbs the accretion flow, leading to the development of Rossby vortices. These ones grow during few rotations around the black hole and force the blob of plasma to accrete towards the centre. At this step, the accretion rate is enhanced near the inner edge of the disk during a period of time comparable to the duration of the flares.

The last mechanism that can produce flares is the tidal disruption of small bodies such as comets or asteroids (Zubovas et al., 2012). If these bodies pass close enough to the black hole, they can be decomposed in many fragments. These pieces will interact with the surrounding gas, create shocks and instabilities leading to subsequent flares. Zubovas et al. (2012) determine that bodies larger than 10 km in size are able to create the observed flares in terms of luminosity.

It could be interesting to note that another hypothesis was suggested in the early 2000's by Nayakshin et al. (2004). They propose that stars in the cluster close to Sgr A* would interact twice per orbit with the accretion disk leading to a shock hot enough to cause the large bursts observed in X-rays. However, Zubovas et al. (2012) indicate that this scenario could not be longer supported. In fact, the stellar density is not high enough in the flaring region whose size has been constrained by new observations.

Hotspot models allow to explain the shape of the light curves during bright flares (Karssen et al., 2017). A hotspot refer as a luminous matter blob in orbit around the black hole. This orbiting blob emitted a kind of flash during a finite period of time. During the orbital motion of the blob, this one could pass behind the black hole. Due to the large mass of the black hole, a gravitational lensing effect will affect the observed luminosity from the blob which will be increased. Then, the blob continues its motion on its orbit. As it gets closer to the observer, it will suffer from a Doppler boosting increasing once again its observed luminosity. This model can thus easily explain the double peak shape observed in several bright flares (see Figure 1.8).

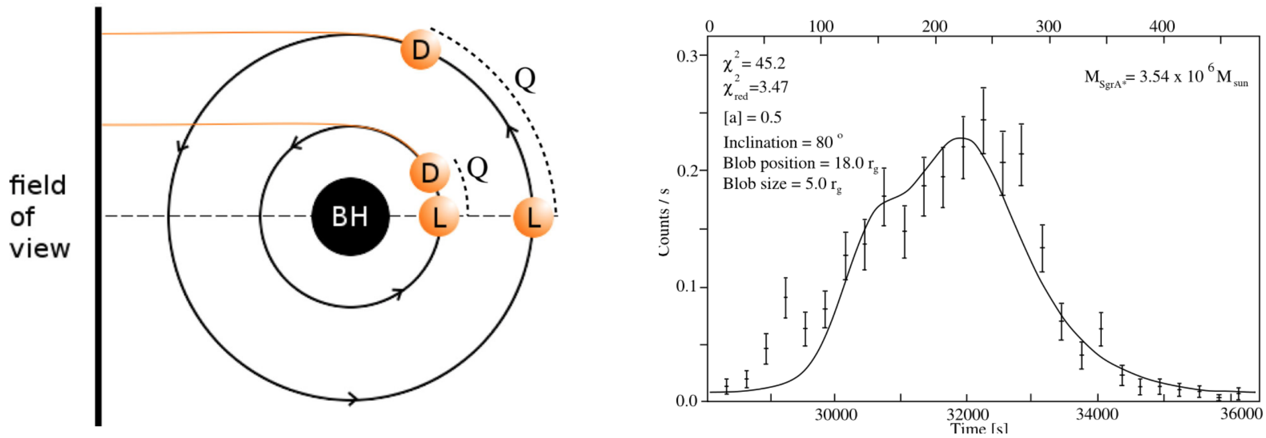

Figure 1.8: Illustration of the hotspot model. *Left panel*: Schematic representation of the blob motion around the black hole to explain the double peak structure of the flares light curves (Karssen et al., 2017). In this sketch, two blobs are represented. The bubbles marked with L indicate the gravitational lensing effect produced behind the black hole. The bubbles marked with D correspond to the Doppler boosting that appears when the blob is moving towards the observer. *Right panel*: Fit of the flare detected by Nowak et al. (2012) with a hotspot model (from Karssen et al. 2017). The asymmetric double peak structure is clearly visible on this fit. We can note that the blob size and its distance to the centre have an impact on the shape of the light curve. On one hand, the further away from the centre the blob is, the more distinct are the two peaks. On the other hand, the larger the blob, the higher the observed flux.

1.4.4 Radiative mechanisms of the flares

Studying flares at different wavelengths can be a probe to evaluate the radiative mechanisms. Several analysis showed that every X-ray flare has a NIR counterpart while the inverse is not true (Genzel et al., 2010). The time delay between the two flares is quasi null while it lasts about 100 minutes to 3 hours before a subsequent flare in the millimetre domain, if this one exists (Genzel et al., 2010).

Works focusing on NIR flares show up that the spectral index of the brightest ones is consistent with a pure optically thin synchrotron radiation mechanism (Bremer et al., 2011). The principal indicator that the NIR flares are due to optically thin synchrotron radiation is the high polarization detected during these events (Trippe et al. 2007; Nishiyama et al. 2009). This emission could be created by relativistic electrons with a Lorentz factor $\gamma \sim 10^{2-3}$ (Genzel et al., 2010).

Concerning the X-ray flares mechanism, several hypotheses are proposed (see left panel of Figure 1.9 for a schematic review). All of them can reproduce the observations (see right panel of Figure 1.9).

- The first possibility is the Synchrotron Self-Compton (SSC) emission (Baganoff et al. 2001; Markoff et al. 2001; Sabha et al. 2010). In this case, the synchrotron photons are scattered by the same population of electrons that emitted them (see upper right panel of the schematic view in Figure 1.9).

- The second possibility is the Inverse Compton (IC) scattering. Yusef-Zadeh et al. (2006) discussed two mechanisms based on the IC process. On one hand, the radio/submillimetre photons are upscattered by the energetic electrons (~ GeV) producing the NIR flares (see bottom left panel on the schematic view in Figure 1.9). On the other hand, it is the NIR-photons that are upscattered by the electrons at the origin of the quiescent radio/submillimetre state of the source (see bottom right panel of the schematic view in Figure 1.9).

- The last hypothesis is the direct synchrotron emission (Yuan et al. 2003; Dodds-Eden et al. 2009). In this case, the emission comes from a population of very energetic electrons (see upper left panel of the schematic view in Figure 1.9). A more recent clue was provided by Ponti et al. (2017) who fitted the spectral slope in NIR and X-ray during a bright flare. This allows them to establish that the radiative mechanism at the origin of this flare is a synchrotron emission with a cooling break. If the process that leads to the acceleration of electrons and then to synchrotron emission takes its energy from the magnetic field, like it is the case during magnetic reconnection, then the magnetic field strength should vary.

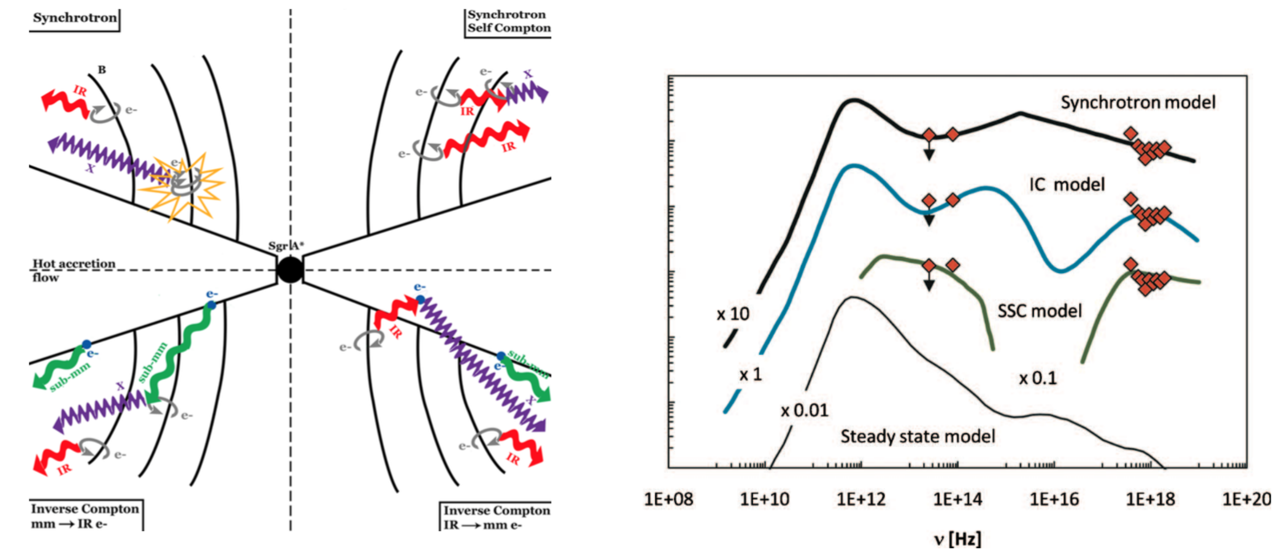

Figure 1.9: *Left panel*: Schematic view of the different possible radiative mechanisms at the origin of the flares (from Mossoux 2016). See text for details. *Right panel*: SED of Sgr A* during simultaneous NIR/X-ray flares (from Genzel et al. 2010). It shows the three emission mechanisms discussed in the text. All globally match the observations in the X-ray and NIR and can therefore contribute to the origin of X-ray flares.

1.5 Interesting objects close to Sgr A*

In this section, I will review briefly few objects located close to Sgr A* which may impact its observation.

1.5.1 The Dusty-S-cluster Object/G2

In the beginning of the 2010's, Gillessen et al. (2012) discovered a new object in orbit about Sgr A* thanks to observations with the VLT. It is named G2 or Dusty-S Cluster Object (DSO). It was first described as a 3 Earth masses cloud made of ionised gas and dust at low temperature (Gillessen et al., 2012). The authors suggested that during the passage at pericentre, the DSO will interact with the hot accretion flow. This interaction should perturb and wipe out the cloud through Kelvin-Helmholtz and Rayleigh-Taylor instabilities. In addition, a shock could be produced in the cloud leading to a quick increase of the temperature, up to $6 - 10 \times 10^6$ K, at the origin of an enhanced emission of X-rays. If the instabilities disrupt the cloud in several fragments, then this emission should be variable.

However, other scenarii are also possible. The DSO could be a pure gas cloud as well as a compact source embedded in a gas cloud (Burkert et al., 2012). This latter possibility seems consistent with observations of this target after its passage to periapse in April 2014 (Witzel et al. 2014b; Valencia-S. et al. 2015). Indeed, in the case of a pure gas cloud, the DSO should be totally disrupted by the tidal interactions with Sgr A* during its closest approach while observations suggest that the DSO has survived. Valencia-S. et al. (2015) concluded that the size of the cloud stays lower than 20 mas while the gaseous model predicts a size about 10 times higher. In addition, they did not observe the Brackett-γ line (emitted by the DSO) blueshifted and redshifted at the same time during the passage at periapse as it would be the case for a pure gas cloud that should be stretched. Moreover, no elevation of the continuum of the X-ray emission has been detected after the passage to periapse (Haggard et al., 2014), as it would be the case if a shock has developed in the cloud (Gillessen et al., 2012). Valencia-S. et al. (2015) proposed that the DSO is then a pre-main-sequence star accreting matter that surrounds it.

Mossoux & Grosso (2017) showed that the faint flaring rate decreased in from 2013, thus before the passage of the DSO to pericentre. Then an increase of the bright flaring rate has been observed from mid 2014, after the passage to periapse. However, the energy saved during the decay of the faint flaring rate could explain the rise of the bright flaring rate without taking into account the inputs of material from the DSO (Mossoux & Grosso, 2017). These observations indicate that the DSO does not have a direct impact on the emission from Sgr A*. However, thanks to magnetohydrodynamic simulations, it has been shown that the brightening of Sgr A* could be increased with a time delay with respect to the passage at pericentre (Kawashima et al., 2017). In fact, the cloud would have an impact on the magnetic field in the accretion flow. The magnetic energy associated would then increase in 5 to 10 years after the passage of the cloud leading to more synchrotron emission. This explains why there is to date no detection of an increase flux in radio as well as in NIR. For the X-ray domain, is has been developed in Section 1.4 that the flares may occur when magnetic reconnection happens, and then could be enhanced when the magnetic field will be amplified 5 to 10 years after the passage of the DSO while the steady emission would not be affected because it originates from further away than the orbit of the DSO (Kawashima et al., 2017).

1.5.2 X-ray sources close to Sgr A*

Some sources close, in projected distance, to the black hole can sometimes have an enhanced emission in X-rays during a finite period of time. If the projected distance between them and the black hole is too small, then the observations of Sgr A* would be contaminated. This will lead to an artificial increase of the quiescent level of Sgr A* and moreover it would be difficult to disentangle the variations of the Sgr A* light curve from those of the transients. Among these possible sources of contamination three have been identified recently:

- In April 2013, Kennea et al. (2013) reported the detection of a gamma-ray burst coming from the same place than a soft X-ray burst observed towards Sgr A*. This indicates that the X-ray burst was actually not a flare from Sgr A* as first thought but an outburst of a new object, called SGR J1745-2900, where SGR stands for Soft Gamma Repeater, at a distance of 2.5 arcsec from Sgr A*. Further study of other bursts from this object provided information about the nature of this object: SGR J1745-2900 is actually a magnetar[2] that entered in a outburst phase in 2013 (Mori et al., 2013). Because of this, it was more difficult to exploit the data collected for the study of the flares from Sgr A*, especially for the faintest ones (Mossoux et al., 2016). Coti Zelati et al. (2017) indicate that the magnetar may have reached its quiescent emission level at the end of 2017 but this estimation is just a lower limit because its quiescent luminosity is unknown. Thus the outburst phase could also end by 10 years.

- At the beginning of February 2016, Reynolds et al. (2016) mentioned the observation of a new active X-ray transient at about 16 arcsec from Sgr A* thanks to the telescope Swift. Since it was impossible, just with this observation, to know if the source was associated with an already known one, they named this object SWIFT J174540.7-290015. After its discovery, it was further studied to determine its location and its nature. At the end of February 2016, Chandra observed this target and it was possible to get a more precise position: RA(J2000) = 17:45:40.664 ± 0.3433, Dec(J2000)= -29:00:15.61 ± 0.3263 (Baganoff et al., 2016). Degenaar et al. (2016b) observed the Galactic Centre at the end of May 2016 and found that the transient was still active. An observation with XMM-Newton allows Ponti et al. (2016) to rule out the hypothesis of a magnetar since its peak luminosity is too high compared to other magnetars at this distance and also because its observed flux showed a variable decay instead of a smooth one as expected for magnetars. They thus proposed that the transient is in fact an accreting X-ray binary with in one

[2] A magnetar is a neutron star with a higher magnetic field than usual neutron stars (up to $10^{14}-10^{15}$ G instead of less than 10^{13} as usual). Their existence has been postulated first by Duncan & Thompson (1992) and can explained the sudden emissions of gamma rays or X-rays like in the case of SGR J1745-2900.

hand a neutron star or a black hole and on the other hand a low mass companion. This assumption is reinforced by the study of the spectrum of the source by Corrales et al. (2017). The authors also found that the source is embedded in a dust-scattering halo.

- In May-June 2016, another X-ray source suddenly rose in luminosity (Degenaar et al., 2016b). It was located at a place where no X-ray source was known and thus named SWIFT J174540.2-290037. Its absorbed flux in the 2-10 keV band reached a value of $(7 \pm 2) \times 10^{-11}$ erg cm^{-2} s^{-1}. Later, thanks to more observations of the source with the UVOT instrument installed on Swift, it has been possible to refine its position: RA(J2000) = 17:45:40.38, Dec(J2000) = -29:00:42.8 (Degenaar et al., 2016a). These coordinates are far enough from other known X-ray sources to conclude that this object was not catalogued before its outburst.

1.6 Context and interest of my Master Thesis

As explained in this Chapter, the supermassive black hole Sgr A* at the centre of our galaxy offers a unique possibility to study the accretion onto such object, especially with low luminosity. In a general way, the study of the X-ray flares from Sgr A* is important in the sense that eruptions are a tool to understand what processes can be at their origin both at a radiative level (synchrotron, inverse Compton process,...) and at a physical level (input of fresh material, disruption of small bodies,...). Through the analyses of the X-ray observations between 1999 and 2015, Mossoux (2016) and then Mossoux & Grosso (2017) revealed that the bright flaring rate increased from 2013 August, while the faint flaring rate decreased one year before. These changes appeared nearly at the same time that the passage to pericentre of the Dusty-S-cluster Object. This passage was thought to have impact on the emission from Sgr A*, but it is likely that the evolution of the flaring rates is not linked to that (Mossoux & Grosso, 2017).

This Master thesis has the aim to pursue these researches by investigating the observations of Sgr A* between 2016 and 2018 carried out by the space telescopes XMM-Newton, Chandra and Swift. The description of these facilities and of the observations will be developed in Chapter 2. My study would allow us to determine if the trend in the flaring rates continues after 2015 or if it was just a short-time change and possibly, to put some constraints on the physical processes at its origin.

Chapter 2

Observational facilities and observations

In this Chapter, I present the three facilities that observed Sgr A* between 2016 and 2018 in X-rays. In Section 2.1, I remind quickly the reasons to use space facilities to observe in X-rays. In Section 2.2 to Section 2.4, I introduce briefly the XMM-Newton Observatory, the Chandra X-ray Observatory and the space telescope Swift as well as the observations of Sgr A* done with them and used in my study.

2.1 The necessity to observe from space

As explained in the first Chapter, it is difficult to see the Galactic Centre due to the presence of matter in the line of sight. It is only possible to observe it in specific wavelengths, mainly radio or X-rays.

In addition, the atmosphere of the Earth also absorbs light at different wavelengths (Figure 2.1). In the radio domain, the atmosphere is quasi transparent: it is thus possible to use ground based telescopes. For instance, the VLA or ALMA have been exploited to study the Galactic Centre. Nevertheless, it is better to build radio telescopes at high altitude to reduce the atmospheric turbulence and to take advantage of a better transparency of the atmosphere. However, it is not conceivable to observe Sgr A* directly from ground in X-rays. Indeed, the upper atmosphere of the Earth blocks the X-ray light (as well as gamma rays or ultraviolet light). Thus, space based telescopes are needed.

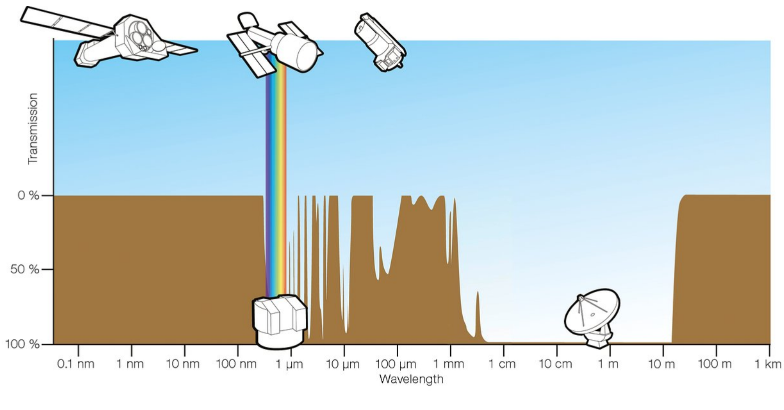

Figure 2.1: Transparency of the atmosphere of the Earth as a function of the wavelength. Credits: ESA/Hubble (F. Granato)

2.2 The XMM-Newton Observatory

2.2.1 Description of XMM-Newton

The following information about the space telescope XMM-Newton come from the "XMM-Newton Users Handbook", Issue 2.16 (ESA: XMM-Newton SOC, 2018b).

XMM-Newton was launched in 1999. It is currently on an eccentric orbit with an inclination of 69° and a period of 47.87 hours. Due to these orbital features, the telescope passes through the radiation belts during its revolution around the Earth which forces to turn off the instruments and to stop the observations about 11 hours during its orbit.

XMM-Newton is composed of three telescopes of 58 concentric mirrors which represent a total effective area of 4650 cm^2 at 1.5 keV. The mirrors at the entrance are paraboloid while those closer to the focal plane are hyperboloid (Figure 2.2). Because X-ray photons are very energetic they can penetrate deep in matter. However, they can be reflected by a mirror if they hit it with a small angle of incidence, that is called grazing incidence. Such an incidence on a parabolic mirror would increase substantially the length of the telescope. Then the configuration in Figure 2.2 allows to reduce the length of the telescope while keeping the required grazing incidence.

Three types of instruments are installed on XMM-Newton:

- European Photons Imaging Cameras (EPIC)
- Reflection Grating Spectrometers (RGS)
- Optical Monitor (OM) for UV/visible imaging and grism spectroscopy

For the study of this Master Thesis, only the EPIC cameras are used. Two types of cameras are onboard. The first type is the pn camera for which the CCDs are back-illuminated. The second type correspond to the two MOS cameras for which the CCDs are front-illuminated. Due to this first difference between the two types of EPIC cameras, the pn has a greater quantum efficiency than the MOS cameras. Other properties are different. For instance: the size of the pixels are not the same ($1''.1 \times 1''.1$ for MOS and $4''.1 \times 4''.1$ for pn), the readout is slower for MOS and the geometry of the chip arrays are also different. However, for the two types the point spread function (PSF) is quite similar. The full width at half maximum (FWMH) of the PSF is of 5" for MOS and of 6" for the pn camera.

It can be worth noting that during the observation of a target, a background arises that can be divided into two parts. The first one is the cosmic X-ray background while the second one is the instrument noise generated by the interactions of energetic particles or photons with the detector and the structure.

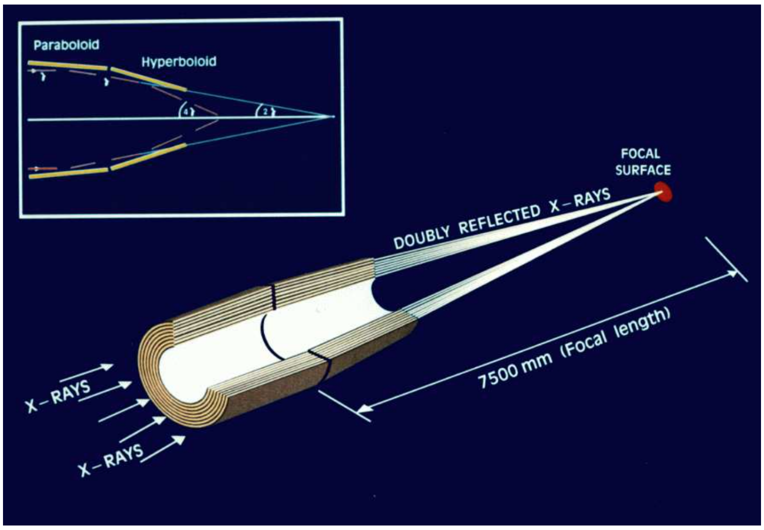

Figure 2.2: Illustration of one mirror assembly onboard XMM-Newton (taken from "XMM-Newton Users Handbook", Issue 2.16, ESA: XMM-Newton SOC 2018b)

2.2.2 Observations of Sgr A* with XMM-Newton since 2016

Only one observation has been done in the direction of Sgr A* between 2016 and 2018. Its characteristics are summarized in Table 2.1. At the date of the observation, the transient SWIFT J174540.7-290015 was very active and it is very likely that the observation of Sgr A* was strongly contaminated by this object.

Table 2.1: Observations of Sgr A* with XMM-Newton since 2016

ObsId	PI Name	Start date (UTC)	End date (UTC)	Exposure (ks)	Instruments
0790180401	Schartel	2016-02-26 16:20:13	2016-02-27 02:36:53	37.0	EPIC (MOS + pn)

2.3 The Chandra X-ray Observatory

2.3.1 Description of the Chandra X-ray Observatory

All the information concerning the space telescope come from The Chandra Proposers' Observatory Guide, Version 21.0 (Chandra X-ray Center et al., 2018).

The Chandra X-ray Observatory (CXO) was launched in July 1999. It is currently on a high eccentric orbit with a period of 63.5 hours during which it spends about 75% of its time above the radiation belts.

The telescope in itself is based on the same principle that the mirror assemblies of XMM-Newton. In the case of Chandra, only one telescope exists and it is composed of four concentric mirrors representing an effective area of 400 cm^2 at 5 keV.

Four instruments are installed onboard the CXO:

- High Resolution Camera (HRC)
- Imaging Spectrometer ACIS
- High Energy Transmission Grating (HETG) which covers the energy range 0.4-10 keV
- Low Energy Transmission Grating (LETG) which covers the energy range 0.08-0.2 keV

The useful instrument for my analyses is the ACIS one. It hosts 10 CCDs (1024 pixels $\times$ 1024 pixels) that are arranged in two ways. The first one is called ACIS-I that is composed of four front illuminated chips while the second is ACIS-S which has four front illuminated chips and two back illuminated ones. ACIS-I has a square shape (16.9 $\times$ 16.9 arcmin) and ACIS-S has a rectangular shape (8.3 $\times$ 50.6 arcmin).

The ACIS instrument has an on-axis effective area of 600 cm^2 at 1.5 keV and a limited spatial resolution due to the size of one pixel, approximately 0.49 arcsec. One can also mention that about 90% of the encircled energy is contained in a circle of radius equal to 2 arcsec centred on the target at 1.5 keV.

2.3.2 Observations of Sgr A* with Chandra since 2016

Several observations of the Galactic Centre have been done with the CXO since 2016. However, I only kept those for which the target Sgr A* was at less than 8 arcmin from the centre of the camera or with an exposure high enough to get information. A very high off-axis angle leads to a PSF of the target that is too large and too deformed.

Between 2016 and 2018, the CXO did sixteen useful observations of Sgr A*, all with the instrument ACIS-S. Table 2.2 summarizes their characteristics.

2.4 Swift

2.4.1 Description of the space telescope Swift

All the technical information about Swift come from The Swift Technical Handbook, Version 14.0 (Swift Science Center, 2017).

The space telescope was launched in 2004. It has currently a low-Earth orbit at an altitude approximately equal to 600 km with an orbital period of about 95 minutes. Hopefully, this orbit would be stable until 2025. The Swift telescope is equipped with three instruments:

- X-Ray Telescope (XRT)

Table 2.2: Observations of Sgr A* with Chandra since 2016

ObsId	PI Name	Start date (UTC)	End date (UTC)	Exposure (ks)	Instrument
18055	Garmire	2016-02-13 08:59:23	2016-02-13 16:26:00	22.7	ACIS-S
18056	Garmire	2016-02-14 14:46:01	2016-02-14 21:44:19	21.8	ACIS-S
18731	Baganoff	2016-07-12 18:23:59	2016-07-13 18:42:51	78.4	ACIS-S
18732	Baganoff	2016-07-18 12:01:38	2016-07-19 12:09:00	76.6	ACIS-S
18057	Garmire	2016-10-08 19:07:12	2016-10-09 02:38:59	22.7	ACIS-S
18058	Garmire	2016-10-14 10:47:43	2016-10-14 18:16:44	22.7	ACIS-S
19726	Garmire	2017-04-06 03:47:13	2017-04-06 12:51:35	28.2	ACIS-S
19727	Garmire	2017-04-07 04:57:18	2017-04-07 13:53:40	27.8	ACIS-S
20041	Garmire	2017-04-11 03:51:22	2017-04-11 13:56:48	30.9	ACIS-S
20040	Garmire	2017-04-12 05:18:22	2017-04-12 14:15:52	27.5	ACIS-S
19703	Baganoff	2017-07-15 22:36:07	2017-07-17 00:01:34	81.0	ACIS-S
19704	Baganoff	2017-07-25 22:57:27	2017-07-26 23:28:30	78.4	ACIS-S
20344	Neilsen	2018-04-20 03:17:44	2018-04-20 12:59:33	29.1	ACIS-S
20345	Neilsen	2018-04-22 03:31:16	2018-04-22 12:57:15	28.5	ACIS-S
20346	Neilsen	2018-04-24 03:33:43	2018-04-24 13:21:29	29.0	ACIS-S
20347	Neilsen	2018-04-25 03:37:23	2018-04-25 14:13:22	32.8	ACIS-S

- UV/Optical Telescope (UVOT) that observes in the range 160-600 nm. In addition, it allows to do grism spectroscopy between 170 and 290 nm.
- Burst Alert Telescope (BAT) which is sensitive between 15 and 150 keV with the aim to detect gamma-ray bursts.

The useful instrument for my study is the first one. It can observe in the range 0.2-10 keV, but it has a low efficiency due to its small effective area (120 cm^2 at 1.5 keV). It covers a field of view of 23.6×23.6 arcmin, with a resolution of 15 arcsec and a PSF of 18 arcsec at 1.5 keV. Like the other facilities described above, the mirror assembly uses the grazing incidence to focus the X-ray photons.

Four readouts modes exist for the XRT, but only three are currently possible on Swift. The first one is called Imaging Mode to produce images. The second one is the Windowed Timing Mode which is useful to have high time resolution but it gives only a one dimensional information. The third mode available is the Photon-Counting Mode to get information over the full field of view.

2.4.2 Observations of Sgr A* with Swift since 2016

Unlike the two other space telescopes, Swift observes regularly the Galactic Centre with its XRT instrument through a daily X-ray monitoring campaign (principal investigator: Nathalie Degenaar). Swift is pointed towards Sgr A* almost everyday, but observations of this target is not possible between November and February when the Galactic Centre is hidden by the Sun. Because it would be too long, I do not list all the useful observations in a table. Indeed, 797 are used in my study spanning between 2016 February 6 and 2018 November 2.

In the case of Swift, the target Sgr A* could be located at more than 8 arcmin from the axis because a good correction would be apply during the data reduction as it will be explained in the next Chapter.

Chapter 3

Data reduction

In this Chapter I describe the data reduction processed on the observations mentioned in Chapter 2. I divide Chapter 3 in three sections, one for each space telescope. Section 3.1 focuses on XMM-Newton, Section 3.2 deals with Chandra and Section 3.3 explains the method used for Swift.

3.1 XMM-Newton

3.1.1 Process

The data corresponding to the observation presented in Chapter 2 are downloaded from the XMM-Newton Science Archive website (`http://nxsa.esac.esa.int/nxsa-web/#home`).

The first step is to organise the different files to be able to apply the same algorithms in case of several observations. It is not mandatory but it makes easier the use of existing tools for analysis. Once the files extracted, two kinds of files are separated: the Observation Data Files (ODF) and Pipeline Processing (PPS) files. The ODF ones gather the data specific to the observation that are useful to reprocess the observation. The PPS ones correspond to photon event files and source lists calibrated with the calibration available at the date of the observation.

The second step is the data reduction which has the aim to provide useful files such as the event list and the Good Time Interval (GTI) in a FITS file. The GTI corresponds to the exposure time of the observation. In an ideal case, the total exposure would be a unique GTI but it can happen that the telescope suffers from high energy radiations (for instance, when the telescope crosses the radiation belts). These radiations could create high noise or in the worst case the observation must be stopped. The time intervals where the level of radiation is too high are thus removed from the GTI.

To reduce XMM-Newton data, some tasks have to be used. I follow the data reduction process given in "Users Guide to the XMM-Newton Science Analysis System", Issue 14.0 (ESA: XMM-Newton SOC, 2018a). I begin to initialise the Science Analysis System version 17.0 (SAS 17.0) with the Current Calibrations Files (CCF) of September 2018. Then I run the tasks *epchain* for the EPIC/pn instrument, or *emchain* for the EPIC/MOS instruments. These tasks create attitude history to convert the position on the CCD on coordinates on the sky and provide the event lists. I filter the events at different levels. The first one is the selection of the patterns. Actually, the origin of the events (X-ray photons, cosmic rays,...) can be determined thanks to the pattern they produce on the CCD. I only keep the ones produced by X-ray photons, that is to say patterns lower than 12 for MOS and lower than 4 for pn (Figure 3.1). The second filter is called flag and corresponds to the rejection of columns or pixels of a CCD. Concerning the pn instrument, I select the FLAG==0 which is the most restrictive one as Mossoux (2016) did. It rejects several pixels (or bad columns) around the bad pixel (or dead column) and near the edges of the CCD which lead to a large loss of photons from the observed source if this one is close to a bad pixel, dead column or edge of the CCD. For MOS, two masks exist: #XMMEA_EM which rejects only the bad pixels, dead columns and edges of the CCD, and #XMMEA_SM which corresponds to an intermediate rejection between #XMMEA_EM and FLAG==0. Following Mossoux (2016) I apply #XMMEA_SM for MOS in my study.

Once these filters applied, I extract the list of soft protons (10 keV- 12 keV) to get the GTI. Then, the filtered

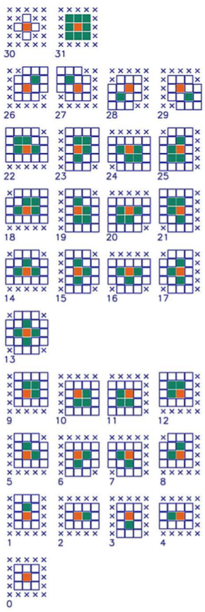

```
                . . .
                . X .
                . . .

. . . . .   . . . . .   . . . . .   . . . . .
. . x . .   . . . . .   . . . . .   . . . . .
. . X . .   . . X x .   . . X . .   . x X . .
. . . . .   . . . . .   . . x . .   . . . . .
. . . . .   . . . . .   . . . . .   . . . . .

. . . . .   . . . . .   . . . . .   . . . . .
. . x . .   . . x . .   . . . . .   . . . . .
. x X . .   . . X x .   . . X x .   . x X . .
. . . . .   . . . . .   . . x . .   . . x . .
. . . . .   . . . . .   . . . . .   . . . . .

. . . . .   . . . . .   . . . . .   . . . . .
. m x . .   . . x m .   . . . . .   . . . . .
. x X . .   . . X x .   . . X x .   . x X . .
. . . . .   . . . . .   . . x m .   . m x . .
. . . . .   . . . . .   . . . . .   . . . . .
```

Figure 3.1: Definition of the patterns for the EPIC/MOS and EPIC/pn instruments (from "Users Guide to the XMM-Newton Science Analysis System", Issue 14.0 (ESA: XMM-Newton SOC, 2018a). *Left panel*: Definition of the patterns for MOS. The red squares correspond to the brightest pixels. The green ones are pixels with a charge above threshold, and the white ones are pixels with a charge below threshold. The crosses are the pixels not impacted by the event. Pattern 0 is for single event, 1-4 are for double event, 5-8 for triple event, 9-12 for quadruple event and 13-21 for quintuple event. *Right panel*: Definition of the patterns for pn. Each row corresponds to a different type of event (from single at the top to quadruple at the bottom). The "X" indicates the brightest pixel, the "m" is the less bright pixel, the "x" are for pixels with a charge above the threshold and "." show pixels not affected by events above threshold.

event lists are obtained rejecting the high background due to the soft protons and selecting the events in the chosen energy range (between 2 and 10 keV) and in the defined regions (see Section 3.1.2).

Finally, it is possible to create the light curve, which corresponds to a temporal histogram of the events, for the background and the source. The last one is then corrected with the task *epiclccorr* which corrects from the background.

3.1.2 Definition of the regions

The process described above allows to get event lists of two regions: one for the source and one for the background. It is thus necessary to create these regions before applying the data filtering. For that purpose, I used the software ds9 in which I defined the two regions following Mossoux & Grosso (2017):

- Source: $10''$-radius circle region centred on Sgr A*
- Background: square region of size $180'' \times 180''$, located at about $4'$ at the North of Sgr A*

The source region corresponds to a fraction of encircled energy of about 50% at 1.5 keV according to the "XMM-Newton Users Handbook", Issue 2.16, 2018 (ESA: XMM-Newton SOC, 2018b). The size of the circle is limited by the presence of other X-ray sources close to the target. As Sgr A* is embedded in a diffuse X-ray emission, the radius of the circle has to be large enough to get as much energy from Sgr A* as possible, but also small enough to avoid contamination by the diffuse emission. This diffuse emission would increase the non-flaring level leading to less efficient detection of flares. It has thus to be stressed that the source region will not contain a pure emission from the target but also from the diffuse emission and other point-like X-ray sources.

The background region is used to estimate the instrumental noise. The background region has to be on the same CCD than the source region and as large as possible to have a better estimation, but X-ray sources have to be excluded. In the case of Sgr A*, it is difficult to choose a annular region around the source region because a lot of X-ray sources are present at that place. This explains the choice of a distant region for the background. In order to avoid the other X-ray sources in the defined square, I used the SAS task named *edetect_chain* that performs the detection of all the X-ray sources in the field of view. Once done, I can remove those located in the backgroundd region (Figure 3.2).

3.2 Chandra

3.2.1 Process

In a general way, the data reduction follows the same scheme for Chandra data than for XMM-Newton data. The differences appear essentially in the software. As for XMM-Newton, the first step is to download the data of the observations presented in Chapter 2 via the Chandra Data Archive website (`http://cxc.cfa.harvard.edu/cda/`). Then, I extracted the files and organized them the same way for each observation to be able to apply the same algorithms to each one.

The data reduction is done thanks to the software named Chandra Interactive Analysis of Observations (CIAO version 4.9) with the Chandra Calibration Database (CALDB 4.7.4). It is not totally the same if a grating HETG is used, but in my case all the observations were done without it. I will thus only explain briefly the method for the case where no grating is used. First, it is necessary to define the extraction regions of the source and the background from which the event lists will be extracted (see Section 3.2.2).

Then, I use a command named *chandra_repro* which creates the event list. When using the function, I specify that I want to take into account the bad pixels and the new calibration of the telescope to create the event lists. Once done, the GTIs are found and I filter the event list as a function of the energy range (500-10000 eV). Finally, it is possible to compute the light curves of the source and the background with the specific properties (GTIs, energy) wanted.

3.2.2 Definition of the Chandra regions

As mentioned, it is needed to create a source and a background region to extract the event lists. Unlike XMM-Newton, both regions are circular and with smaller dimensions. Indeed, the source one is a $1''.25$-radius circle centred on the radio position of Sgr A* while the background one is a $8''.2$-radius circle located at $0'.54$ to the south from Sgr A* where no known X-ray sources are located (Figure 3.2).

According to the Chandra Proposers' Observatory Guide, Version 21.0 (Chandra X-ray Center et al., 2018), the source region corresponds to a fraction of about 90% of encircled energy. Unlike XMM-Newton, Chandra is less sensitive to faint X-ray sources. As a consequence, it is not necessary to look for X-ray sources in the background region because the size of the region is smallest than the one used for XMM-Newton and it is thus less likely to collect photons from faint X-ray sources in this region.

3.3 Swift

3.3.1 Process for data reduction

The observations are found on the NASA High Energy Astrophysics Science Archive Research Center website (`https://heasarc.gsfc.nasa.gov/`).

The first step is to compute the distance between Sgr A* and the centre of the CCD. As the target gets away from the centre, its PSF is deformed and the determination of the distance between them allows the correction of the PSF during the data reduction.

In the case of Swift, the tool used to process the data is named XSELECT, included in the software HEASOFT, version 6.24. I begin to use the function *xrtpipeline* which rejects the bad pixels and performs the data reduction for each observation. Then, the task *xrtlccorr* enables to determine the correction to be applied on the observed count rates because of the bad pixels, vignetting (darkening close to the edges of the CCD) and the deformation of the PSF. In practice, the task computes a correction factor that will be used to correct the observed light curve for each 10 seconds time interval. This factor is larger when the source is off-axis than

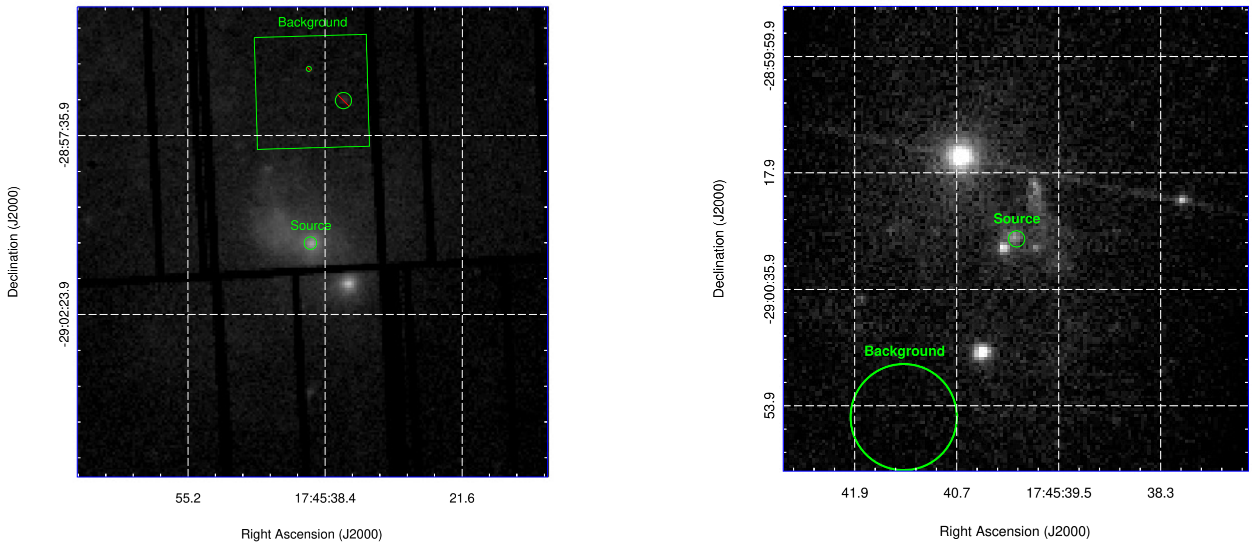

Figure 3.2: Definition of the source and background regions with ds9 software. *Left panel* : Source and background regions for EPIC instruments (observation on 2014 April 02). The green circle corresponds to the source extraction region centred on Sgr A*. The green square is the background extraction region. In this one, green circles containing a red line are visible: they correspond to the X-ray sources removed from the background region. *Right panel*: Source and background regions for Chandra defined with ds9 software (observation on 2016 July 12). The biggest circle corresponds to the background region while the smallest one is the source region centred on Sgr A*.

on-axis and also when the target is located on a bad column or a bad pixel. Mossoux (2016) established that the median correction factor is 2.3 that will be an indication to know if an observation could be analysed further in my study. Finally, I extract the event list from the selected source region.

3.3.2 Definition of the regions

Unlike the two other telescopes, Swift is on a low-Earth orbit and remains inside the radiation belts. As a result, the instrumental noise caused by the flaring protons is negligible. It is thus not necessary to create a background region. The source region is defined by a 10″-radius circle centred on Sgr A*, just like the one used for XMM-Newton.

Chapter 4

Study of the flaring activity

In this Chapter, I explain the results of my study about the flaring activity of Sgr A* during the period 2016-2018. Section 4.1 describes the analyse of the XMM-Newton and Chandra observations, with the description of one important algorithm named Bayesian blocks algorithm. In Section 4.2, I introduce the results from the Swift observations. Then, I explain the method to obtain the intrinsic flare distribution from the observed one in Section 4.3. Finally, I present the evolution of the flaring rate from 1999 to 2018 in Section 4.4 by gathering my data with the ones got in previous studies.

4.1 XMM-Newton and Chandra observations

4.1.1 Description of the Bayesian blocks algorithm

An important algorithm I used for my study is the two steps Bayesian Blocks algorithm described by Mossoux et al. (2015a,b). This algorithm is based on the one proposed by Scargle (1998) then improved by Scargle et al. (2013) to detect statistically significant changes in a time series. It is thus useful to detect flares from Sgr A* during observations (Nowak et al. 2012; Neilsen et al. 2013) as significant changes in the poissonian count rates of the non-flaring level since the data show that the observed emission is not a continuous line with a peak during a flare but rather a continuously variable series in which one needs to detect significant changes in the count rates.

The usual Bayesian blocks method (Scargle 1998; Scargle et al. 2013) consists in the following steps:

- The photon arrival times are associated to the centre of the frame during which they have been detected. If several photons have been recorded during the same frame, we consider that they all have the same arrival time.

- The frames impacted by very high energy particles are removed and all the GTIs are concatenated to get a continuous flux of photons.

- The time sequence is divided into several intervals, or cells. The separation between two consecutive cells (containing at least one photon) is defined in such a way that the distance between it and two consecutive photons is equal. The cells are named Voronoï cells because this division is equivalent to the Voronoï tessellation. The count rate of a cell is then defined as the number of photons inside it divided by the length of the cell.

- All the cell lengths are then multiplied by the corresponding livetime which is lower than 1. The livetime is defined as the fraction of the time during which the CCD is collecting the photons (integration of events). This operation allows the correction of the gaps in the observation due to the CCD readout of the events and leads to an increase in the count rate.

- Then, an iterative process occurs. First, the overall time range is considered and it is determined if it is statistically correct to describe the count rates of all the cells by one block with a constant rate. If not, two blocks are defined with different count rates, separated by what is called "a change point". Then, the algorithm repeats the same thing on each block again and again.

- The stop of the iterative process is determined by the "prior number of change points" (called *ncp_prior* hereafter) which depends on the number of events collected during the observation and on the false positive rate that corresponds to the probability that a change point is actually a false detection.

The result of this process is the most probable division of the time range into several blocks in which the count rate of the photons can be considered as constant (see top and middle panels of Figure 4.1). Typically, if one pulse (flare in the case of my study) is detected in the data, the observation time will be fragmented into at least three blocks: one of low count rate corresponding to the constant emission of all the sources inside the extraction region, one (or more) of high count rate during the burst phase and the last one, after the burst, with a count rate close to the first one.

4.1.2 Calibration of the algorithm

As mentioned, it is needed to determine the best *ncp_prior* to get the optimal segmentation of the time series, with a small probability to detect false change points. In the case of my study, I used a false positive rate p_1 equal to exp(-3.5) as Mossoux et al. (2015b) did. It corresponds to a probability that the found change point is true of 1-p_1=96.98%. However, a flare is generally identified by the presence of two change points (one for the raising flux and one for the decreasing flux to come back at the initial level). Hence, the probability to detect a true flare is $1 - p_1^2 = 99.90\%$. One method to calibrate the *ncp_prior* is to simulate several event lists with a constant count rate on which the Bayesian blocks algorithm will be used with different *ncp_prior* (Mossoux, 2016).

In concrete terms, for each observation, I simulated 100 events lists considering the quiescent level and the same exposure as in the observation. Each of the synthetic event list represents the non-flaring level of the observation that is to say that only a unique Bayesian block is needed to describe it. Then, the Bayesian blocks algorithm is applied on each of the 100 event lists for different *ncp_prior*. In theory, no change point must be detected. However, it can happen that one is found because the *ncp_prior* is not adapted. For each *ncp_prior*, I computed how much change points are detected, that are necessarily false. At the end, I only kept the *ncp_prior* which gives a false positive rate equal to p_1.

4.1.3 The two steps Bayesian blocks algorithm

The two-steps Bayesian Blocks described by Mossoux et al. (2015a,b) has the aim to correct the event lists from the background. This process consists in the following steps:

- First, I applied the Bayesian Blocks algorithm as described previously, on two event lists: the background one and the source (with background) one. I note CR_{bkg} and $CR_{src+bkg}$ the count rates corresponding of the events to the two lists, respectively.

- Then, for each Voronoï cell in the source list, I compute a weight, taking into account the fact that the area of the background region is not equal to those of the source region. To compare both regions, it is thus needed to multiply CR_{bkg} by the surface ratio A, corresponding to the ratio between the area of the source region and the area of the background region. The weight is: $w = CR_{src+bkg} / \left(CR_{src+bkg} - CR_{bkg} \times A \right)$.

- I applied once more the Bayesian Blocks on the corrected source list. It allows to obtain the event list of the target only, with the instrumental background removed (Figure 4.1).

This two-steps Bayesian Blocks is the algorithm I used to detect flares in the XMM-Newton and Chandra observations. I used the same codes developped by Mossoux (2016) in IDL language. Concerning the Swift observations, it is not possible to apply this method because the duration of a flare is generally longer than the duration of an observation. Another method will be adapted in this case as explained in the Section 4.2.

4.1.4 Detection of flares between 2016 and 2018

As described in Section 4.1.2, I first need to calibrate the algorithm for each observation. With the method described to do it, I found that the *ncp_prior* is equal to about 8 for the XMM-Newton observation and is

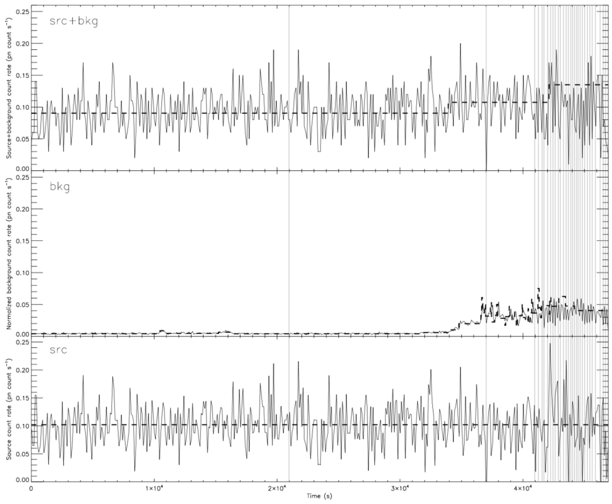

Figure 4.1: Illustration of the two-steps Bayesian Blocks applied on an observation done with XMM-Newton EPIC/pn instrument (taken from Mossoux 2016). The dotted lines on each panel represents the resulting blocks. *Top panel*: Light curve of the initial source region, contaminated by the background. We can distinguish three main blocks. *Middle panel*: Light curved of the background region, with several blocks appearing in particular at the same time than the highest blocks of the first light curve. *Bottom panel*: Light curve of the target only. It is clear that the background has been removed thanks to the process, and the result is just a unique block of constant count rate.

comprised between 9.2 and 9.7 for the Chandra observations. Then, I applied the two-steps Bayesian Blocks on the light curves, which gave me the time of change points and the count rates of the different blocks for each observation. I superimposed the resulting blocks on the light curve to have a visual indicator of the results and check if they are consistent with the shape of the light curves. Figures 4.2 and 4.3 are examples of light curves observed by XMM-Newton and Chandra, respectively. The other light curves can be found in Appendix A.

XMM-Newton observation

Unfortunately, the only observation of Sgr A* with XMM-Newton was a lot polluted by the presence of the active X-ray transient SWIFT J174540.7-290015. It is clear that the event list of the source region will be affected since the region includes the tail of the PSF of this bright object. This leads to an artificial increase of the non-level flaring of Sgr A*. As explained by Mossoux et al. (2015b), the detection of flares is strongly influenced by the non-flaring level and the sensitivity of the instruments. For instance, EPIC/MOS instruments have a lower sensitivity than EPIC/pn one and as a consequence, they can record a lower non-flaring level. Thus, periods of high non-flaring level leads to worse detection of flares, as in the case of an active X-ray transient.

Another problem that appeared is that the observation was made in timing mode deactivating the central CCD of the two MOS instruments. Because of that, no information about Sgr A* can be detected with these instruments and only the EPIC/pn event list can be used for the study. The light curve obtained with this instrument is shown in Figure 4.2.

Although two change points have been found with the two-steps Bayesian Blocks algorithm, one cannot conclude that a flare occurred during the observation. Even the definition of a non-flaring level is difficult in that case, but it is possible to evaluate it to about 3.5 count/s. This is about 30 times the typical value observed in normal conditions, that is to say 0.1 count/s (Mossoux & Grosso, 2017).

Chandra observations

Due to a better angular resolution of the ACIS instruments of Chandra, the X-ray sources at the Galactic Centre are more resolved. As a consequence it observes lower non-flaring level of typically 0.005-0.006 count/s (Mossoux & Grosso, 2017) leading to a better flare detection, even in February 2016 when the X-ray transient

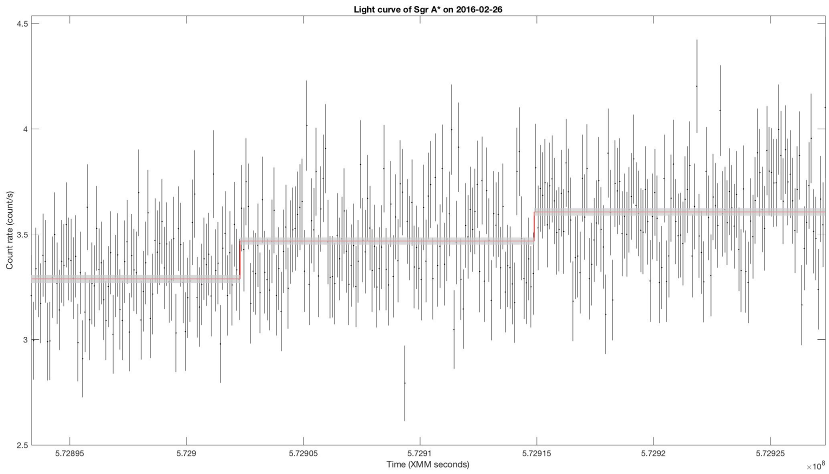

Figure 4.2: XMM-Newton light curve on 2016 February 26. The red line corresponds to the Bayesian Blocks obtained with the algorithm. The grey boxes represent the uncertainties on the value of the blocks count rates. The three boxes most probably reflect the variation from the transient emission than a flare from Sgr A*.

was active. During this month, I can nevertheless see that the non-flaring level was a bit increased (about 0.009 count/s) but that does not really impact the results contrarily to the XMM-Newton case.

During the 16 observations, 9 flares have been detected thanks to Chandra, sometimes several in the same observation. One example of such a light curve is shown in Figure 4.3. This figure illustrates well the fact that even during February 2016, it is possible to detect flare-like variations in the light curve with Chandra. Comparing their features with the ones of the flares found by Mossoux & Grosso (2017) with Chandra allows me to effectively considered them as flares emerging from Sgr A*. Indeed, the characteristics of the detected flares in 2016-2018 are quite similar with several previous identified flares. The properties of the nine flares are gathered in Table 4.1.

Table 4.1: Properties of the flares detected with Chandra in 2016-2018

ObsId	Start Date of the flare (UTC)[a]	End Date of the flare (UTC)[b]	Duration (s)	Non-flaring level (count/s)	Mean count rate (count/s) [c]
18055	2016-02-13 12:14:10	2016-02-13 12:24:07	597	0.0083 ± 0.0009	0.078 ± 0.012
———	2016-02-13 13:00:45	2016-02-13 13:20:23	1178	———————	0.067 ± 0.008
———	2016-02-13 15:40:17	> 2016-02-13 16:15:46	> 2129	———————	0.078 ± 0.006
18731	2016-07-12 22:43:30	2016-07-12 23:17:06	2076	0.0047 ± 0.0003	0.029 ± 0.004
18732	2016-07-18 14:56:24	2016-07-18 15:47:03	3039	0.0047 ± 0.0003	0.017 ± 0.003
20041	2017-04-11 08:23:04	2017-04-11 09:06:59	2635	0.0066 ± 0.0006	0.085 ± 0.006
19703	< 2017-07-15 22:54:42	2017-07-16 00:30:18	> 5736	0.0046 ± 0.0003	0.008 ± 0.002
———	2017-07-16 13:10:52	2017-07-16 13:29:56	1144	———————	0.029 ± 0.005
20346	2018-04-24 05:00:57	2018-04-24 05:42:27	2490	0.0042 ± 0.0004	0.124 ± 0.006

Notes: $^{(a)}$ The sign < indicates that the flare began before the start of the observation; $^{(b)}$ The sign > indicates that the flare ended after the end of the observation; $^{(c)}$ The mean count rate is expressed after subtraction of the non-flaring level.

4.2 Swift observations

4.2.1 The Degenaar's method

For the Swift observations, it seems difficult to use the Bayesian Block algorithm because the number of events recorded during an observation is low and the duration of an observation is generally smaller than the duration of a Sgr A* flare. Instead, Degenaar et al. (2013) proposed another method to be applied in the case of Swift. This method cannot be used on a single observation but on long term monitoring, typically using all the observations done in one year. In this case, a yearly campaign is represented by the mean count rate in each

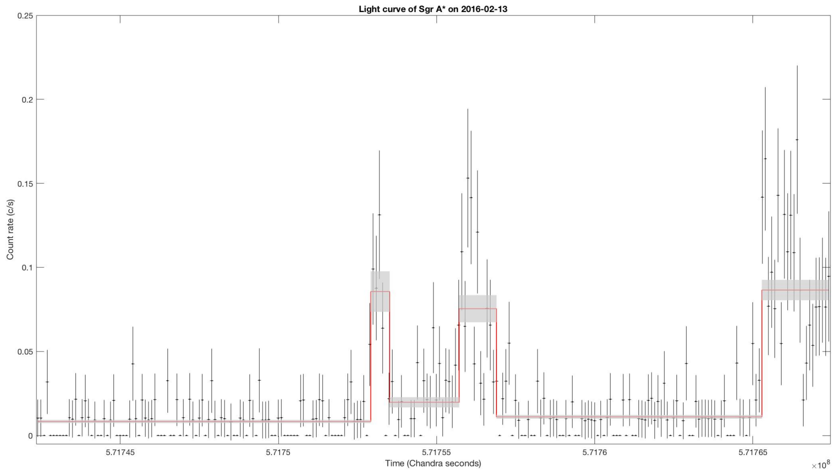

Figure 4.3: Chandra light curve on 2016 February 13. The red line correspond to the Bayesian Blocks with their uncertainties represented by the grey boxes. Three flares occurred during this observation with the last one continuing after the end of the observation.

observation multiplied by the correction factor determined during the data reduction. Then, one can compute the annual mean count rate, which will represent the non-flaring level of the year, and the associated standard deviation σ. If an observation has a mean corrected count rate larger than the non-flaring level plus three times the standard deviation, it is identified as a flare.
Mossoux & Grosso (2017) compared the detection efficiency of the Bayesian blocks algorithm with the Degenaar et al.'s method for a typical Swift observation. It has thus been established that the flares must be shorter than the exposure of the observation or they must have a mean unabsorbed flux of 13.2×10^{-12} erg s^{-1} cm^{-2} to be detected by the Bayesian blocks method. On the contrary, the Degenaar et al.'s method allows a detection efficiency of 100 % for flares with much lower unabsorbed flux (about 7×10^{-12} erg s^{-1} cm^{-2}). Thanks to this analyse, it is justified to use the Degenaar et al.'s method in the case of Swift to detect flares in the present study.

4.2.2 Flaring activity in 2017-2018

I processed the detection of flares with the annual mean count rate as specified by the Degenaar et al.'s method[1]. In 2017, the mean count rate was 0.0255 count/s (associated with a three times standard deviation equal to 0.0397 count/s). In 2018, the values are quite similar: 0.0252 count/s for the mean count rate and 0.0357 count/s for three times the standard deviation.

One last step to firmly confirm the detection of flares is to check the correction factors applied on the observations considered as flares. On 2017 March 07 and 2017 March 23 Sgr A* was located totally on a bad column of the CCD camera. Thus correction factors of 30.5 and 20.4, respectively, were applied on the observations. As a consequence, it was impossible to be sure that these events were really flares and I decided not to include them in my list. Only one event remains for the year 2017. The same work was applied to the year 2018, and the two events can be confirmed as flares since their correction factor is close to 2.3. Table 4.2 summarizes the features of the detected flares on 2017-2018. The flares are shown on the Swift light curves in Figure 4.4 with the label 5 for the one in 2017 and 6, 7 for the ones in 2018. The number of detected flares is consistent with previous studies.

[1]The method was also applied with the median instead of the mean. However, the tests reveal that the mean is more appropriate (see Appendix B for details).

Table 4.2: Properties of the flares detected with Swift in 2017-2018

ObsId	Start Date (UTC)[a]	End Date (UTC)[a]	Non-flaring level (count/s)[b]	Corrected count rate (count/s)[c]	Correction factor
00092395134	2017-06-12 15:59:41	2017-06-12 16:20:52	0.0255 ± 0.0003	0.0964 ± 0.0098	2.17
00093602018	2018-02-17 00:45:29	2018-02-17 01:01:52	0.0252 ± 0.0003	0.0686 ± 0.0098	2.30
00094007131	2018-08-22 19:17:33	2018-08-22 19:29:53	————————	0.0827 ± 0.0121	2.33

Notes: $^{(a)}$ The dates correspond to those of the observation and not of the flare (duration of the flare longer); $^{(b)}$ The non-flaring level correspond to the mean count rate of the year; $^{(c)}$ The corrected count rate corresponds to the mean count rate of the observation multiplied by the correction factor subtracted from the non-flaring level.

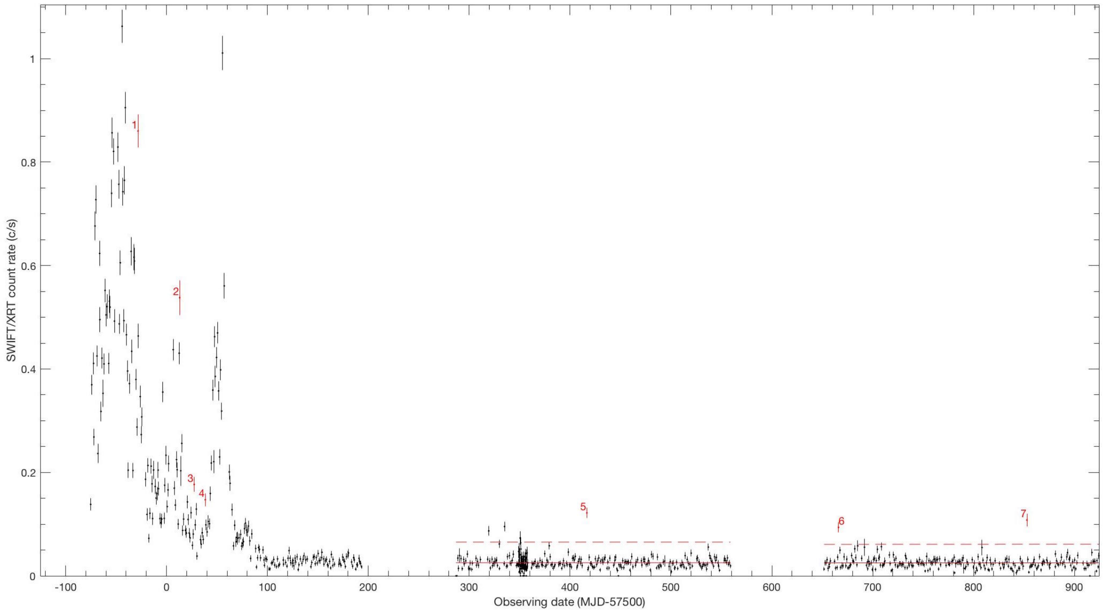

Figure 4.4: Swift light curve between 2016 and 2018. One can clearly see three groups of points corresponding to the campaign of 2016, 2017 and 2018. The red dots with a labelled number correspond to the observations identified as flares. For 2017 and 2018, the red lines are the mean count rates of each year, while the dashed red lines are the 3σ threshold.

4.2.3 Flaring activity in 2016

Concerning 2016, it is clearly impossible to use the same method as for 2017 and 2018 according to the shape of the light curve (left hand-side in Figure 4.4). This shape is due to the contamination of the extraction region by the two X-ray transients presented in Chapter 1. As they were very active during the first part of 2016, the count rates of the Swift observations from Sgr A* were artificially increased with a lot of fluctuations making impossible the use of the Degenaar et al.'s method. The analyse of the year was thus divided into two parts: the period of activity of the transients (before MJD=57600) and the period where the situation came back to normal (after MJD=57600).

For the first part of the year, I extracted events from regions centred on the two transients in order to compare the variations of their light curve with those of Sgr A*. If the flux coming from Sgr A* increases (comparing two consecutive observations) while it is not the case for the curves of the transients, this means that a flare could occurred since the variation would thus be intrinsic to Sgr A*. Nine observations were tagged with this method (red dots in Figure 4.5), but that does not mean that all of them are flares because the fluctuations can be small compare to the mean non-flaring level, undetermined here. In addition, I noticed that sometimes the increase in the light curve of Sgr A* is much higher than the one in the transient light curves. This is the case of especially 7 observations (blue dots in Figure 4.5). For these 16 observations, I checked that the correction factor is valid for a flare detection. This allows me to reject 3 observations (dots tagged 7, 9 and 12). For the 13 remaining observations the count rates have a small correction factor close to 2.3.

However, this approach is a bit arbitrary since I determined 7 potential flares "by hand" with my own opinion of what is a significant increase. It is nevertheless a good starting point to know if we are able to detect some

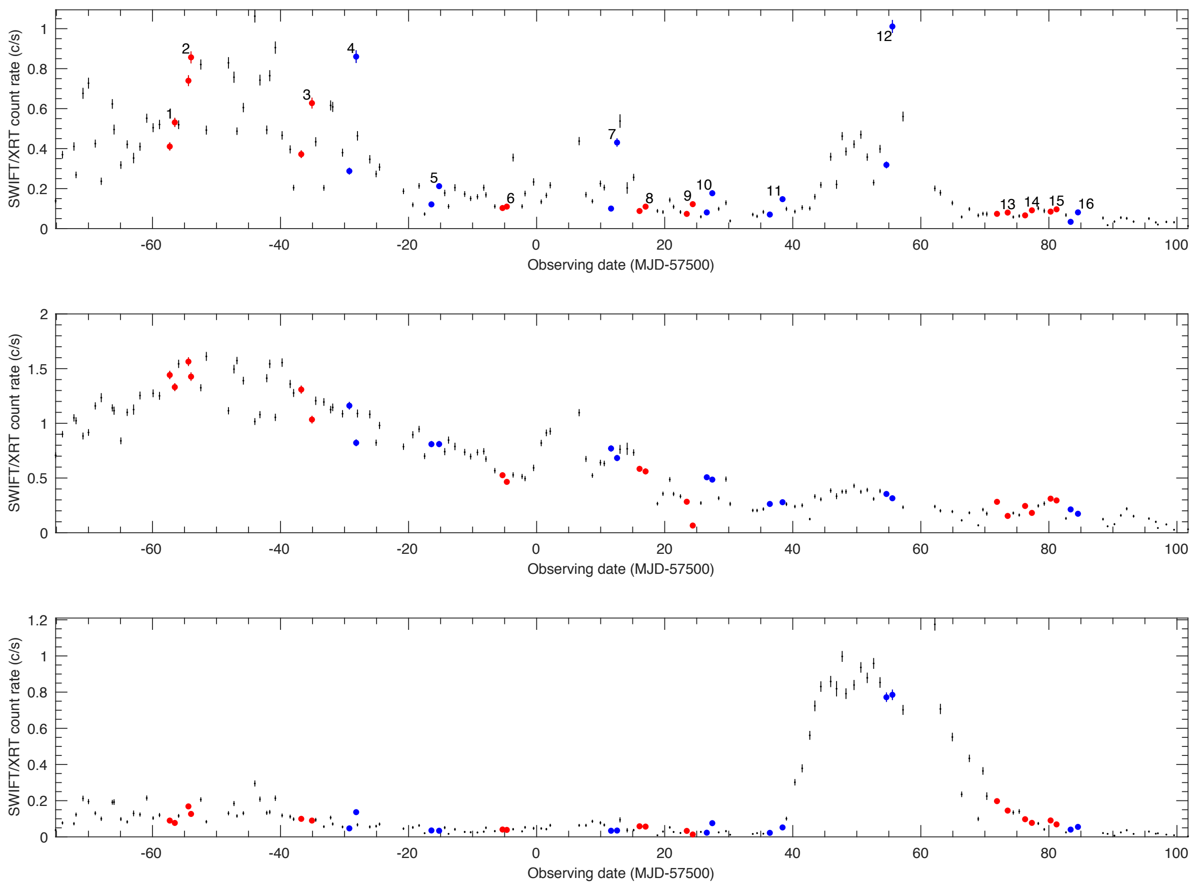

Figure 4.5: Light curves of Sgr A* and the two transients during the first part of 2016. *Top panel*: Light curve of Sgr A*. *Middle panel*: Light curve of J174540.7-290015. *Bottom panel*: Light curve of J174540.2-290037. The red dots represent an increase of flux in the light curve of Sgr A* while at the same time there is a decrease in the light curves of the two transients. The blue dots correspond to increases of flux considered higher in the light curve of Sgr A* than in the two others, but evaluated by hand in first approximation. In each case, the event that would be classified as flare is the second coloured dot (with a labelled number).

flares. A more rigorous way to do that is the following. First, I decided to rule out the observations that have a high correction factor, that is to say larger than 3. Then, I extracted the events of 6 or 7 regions around the transients (Figure 4.6). The centre of each region is at the same distance from the transient than Sgr A*. This allows to have an estimation of the tail of the PSF from the transients at the distance of Sgr A* by computing a count rate averaged for all the regions for each transients at each date and the associated deviation ($\sigma^2_{transient1}$ and $\sigma^2_{transient2}$). I then summed the average light curve of the two transients and used this total mean light curve as a background. I thus subtracted it from the light curve of Sgr A* to get a corrected curve. Finally, I divided the count rates of this new light curve by $\sqrt{\sigma^2_{transient1} + \sigma^2_{transient2}}$ to get the curve in σ units. This is done in order to determine the significance of the differences between the Sgr A* light curve and those of the transients. I then classified as flare the observations where the count rate minus the error is higher than 3. Four observations correspond to this criterion with, among them, three identified in the first approach (Figure 4.7). They are shown in Figure 4.4 in red with the labels 1 to 4. The features of these four events are summarized in Table 4.3. One can note that the uncertainties on the values are high, especially at the beginning of the year because of the presence of SWIFT J174540.7-290015 which had very high count rates (up to 2 count/s).

Concerning the second part of the year 2016, that is to say after MJD=57600 (2016 August 01), the activity of the transients stopped. This allows me to use the Degenaar et al.'s detection method (Figure 4.8). No flare have been detected during that period. The mean count rate during that period was 0.0278 count/s (with 3σ = 0.0244 count/s).

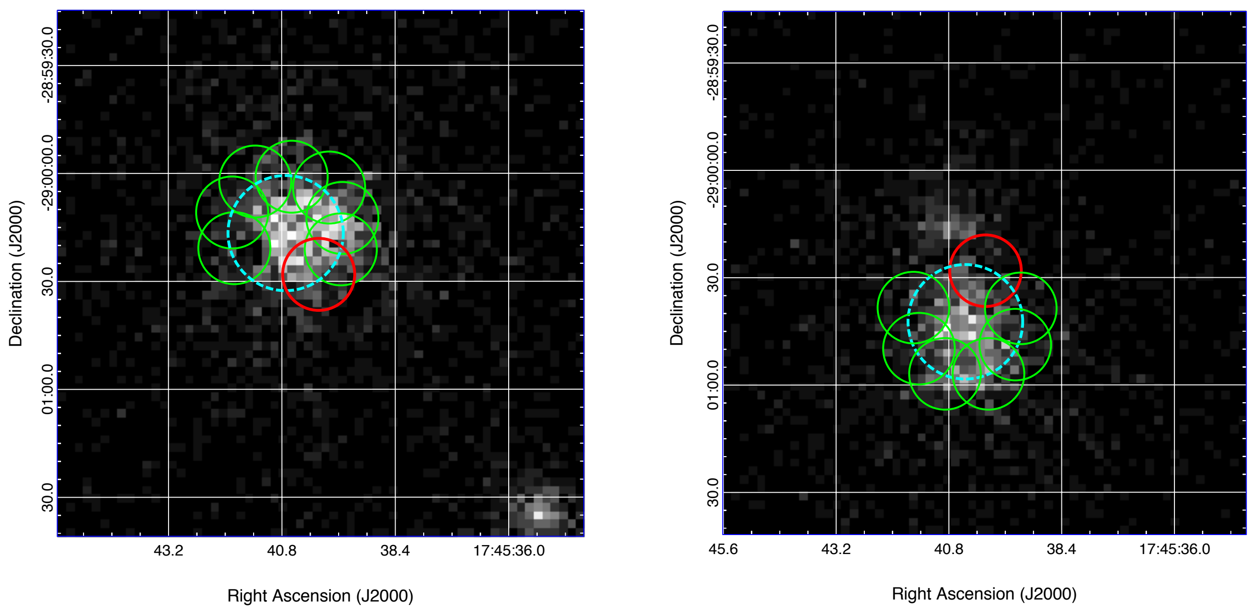

Figure 4.6: Region of extraction to make a background with the transients SWIFT J174540.7-290015 (*left panel*) and SWIFT J174540.2-290037 (*right panel*). The circle in red corresponds to the extraction region centred on Sgr A*. The dashed blue circle is centred on the transient with a radius equal to the distance transient-SgrA*. The green circles are the extraction regions used for the background: they are all at the same distance from the transient than Sgr A* in order to reconstruct the "tail of the PSF".

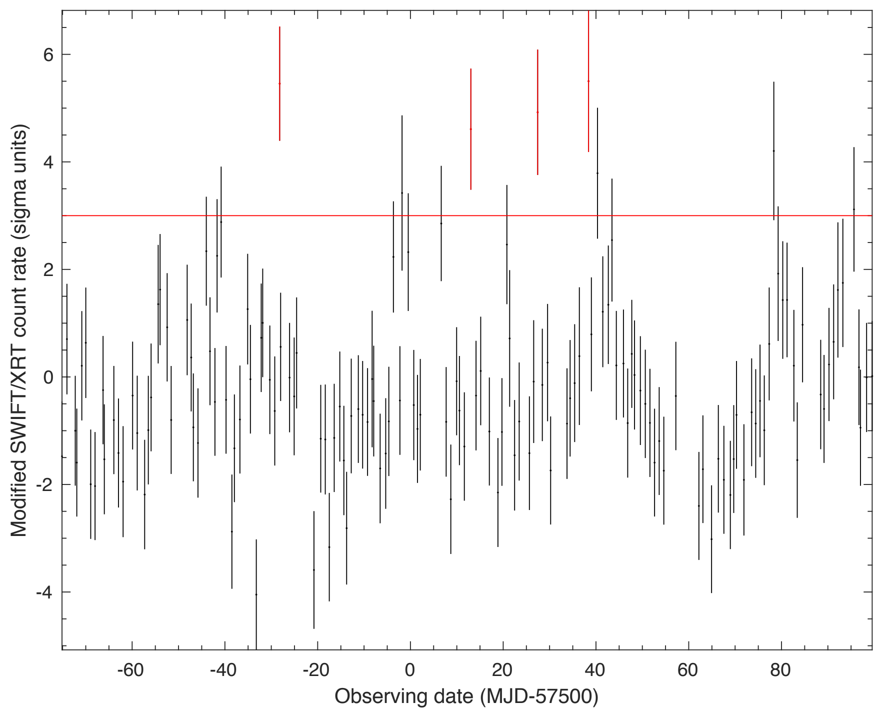

Figure 4.7: Modified light curve of Sgr A*, expressed in σ units after subtraction of the transients background. The red line corresponds to the 3σ threshold. The four red dots are the events identified as flares. Only the second one was not flagged with the first approach.

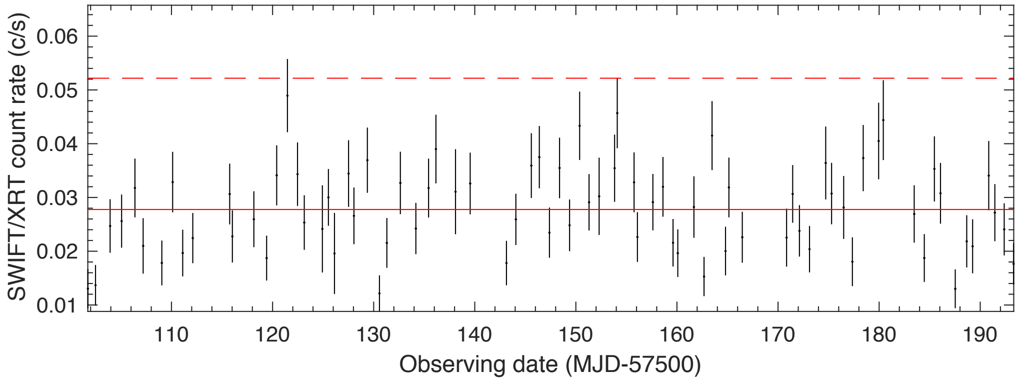

Figure 4.8: Degenaar et al.'s method for the second part of 2016 (after August 01). The red line corresponds to the mean count rate during that period. The red dashed line corresponds to the 3σ threshold. No flare has been detected.

Table 4.3: Properties of the flares detected with Swift in 2016

ObsId	Start Date (UTC)[a]	End Date (UTC)[a]	Non-flaring level (count/s)[b]	Corrected count rate (count/s)[c]	Correction factor
00092201242	2016-03-24 19:29:41	2016-03-24 19:43:54	0.377 ± 0.089	0.483 ± 0.094	2.10
00092236033	2016-05-05 00:36:01	2016-05-05 00:43:53	0.238 ± 0.065	0.300 ± 0.073	2.25
00092236047	2016-05-19 10:23:39	2016-05-19 10:39:40	0.061 ± 0.024	0.116 ± 0.028	2.25
00092236056	2016-05-30 09:42:54	2016-05-30 09:58:54	0.068 ± 0.015	0.080 ± 0.019	2.43

Notes: [(a)] The dates correspond to those of the observation and not of the flare (duration of the flare longer); [(b)] The non-flaring level correspond to the corrected mean count rate of the transient background at that date; [(c)] The corrected count rate corresponds to the mean count rate of the observation multiplied by the correction factor subtracted from the non-flaring level.

4.3 Intrinsic flare density

4.3.1 Probability of flare detection

The detection efficiency of flares depends strongly on the non-flaring level and on the instrument sensitivity. As already mentioned in Section 4.1.4, a high non-flaring level prevents from the detection of small flares. Indeed, the variations of flux will be swamped in the fluctuations of the non-flaring level, and thus would not be considered as significant changes in the flux. All this is linked also to the sensitivity and angular resolution of the instruments which determine the extraction region (nearby sources resolved or not) and the time separation of events.

For each observation, it is thus needed to determine the proportion of flares undetected. For that purpose, simulations are needed. Following Mossoux & Grosso (2017), several event lists are created with a non-flaring level corresponding to the one of the different observations of Chandra and XMM-Newton between 2016-2018[2] and with a Gaussian curve superimposed representing a flare. For each simulation, the flux and duration of the flare are changed in order to reproduce the overall observed ranges. Typically, the simulations are done with 30 different fluxes (between 0.6 and $40.0 \times 10^{-12}\,\mathrm{erg\,s^{-1}\,cm^{-2}}$) and 30 different durations (between 300 and 10.5×10^3 seconds). For each couple flux/duration, the Bayesian blocks method is applied on 100 simulated event lists for a false positive rate of $p_1 = \exp(-3.5)$ and we compute the total number of flares detected, which gives the probability to detect one flare with these properties. The advantage of this method is that the flux and duration of a flare are totally independent of the instrument, and thus only the non-flaring level is important.

At the end, I would like to determine the average detection efficiency of each instrument and each observation computed on the same grid. To do that, the detection efficiencies for each observation (from 1999 to 2018) grouped as a function of their non-flaring level are weighted according to the total exposure time of the corresponding non-flaring level. Then the detection efficiencies are summed to determine the merged local de-

[2]However, the properties of the flares detected with Swift are not enough constrained (duration and flux unknown). That is why the correction of the observed flares distribution will be done from the probabilities of detection of XMM-Newton and Chandra and that explains why I do not include Swift in the merged local detection efficiency.

tection efficiency for a given flare independently of the observing telescope. These merged probabilities of flare detection are shown in bottom left panel of Figure 4.9. One can notice that the 100% detection contour is never reached in the considered simulated grid: this is due to the high non-flaring level viewed by XMM-Newton during 2016.

4.3.2 Observed flares and intrinsic distribution

The next step is to gather the 99 flares detected by Mossoux & Grosso (2017) between 1999 and 2015 with Chandra and XMM-Newton, with the 9 I detected between 2016 and 2018 to compute the observed flare density. The unabsorbed flux is computed from a conversion factor and not with a spectral analyse. This is done to consider all the flares in a homogeneous way while reducing the errors on the measures that could be very high when we fit a spectrum for small flares (few counts). Since no flare has been detected with XMM-Newton, only the conversion factors for Chandra ACIS-S instrument and Swift XRT instrument are needed. Mossoux & Grosso (2017) computed their value: $148.1 \times 10^{-12}\,\mathrm{erg\,s^{-1}\,cm^{-2}/count\,s^{-1}}$ and $293.5 \times 10^{-12}\,\mathrm{erg\,s^{-1}\,cm^{-2}/count\,s^{-1}}$, respectively. Recap charts of all the flares detected between 2016 and 2018 are shown in Appendix C, where the mean unabsorbed fluxes are given.

To determine the observed flares distribution, I follow the Mossoux & Grosso (2017)'s recipe based on the the work from van de Weygaert & Schaap (2009). From the unabsorbed fluxes and durations of the 108 flares detected with Chandra and XMM-Newton since 1999 it is possible to construct the minimum triangulation of the Delaunay tessellation (blue triangles in the top left panel of Figure 4.9). The observed flare density (in flares per unit flux per unit duration) associated to a given flare position, in the diagram duration/unabsorbed flux, is directly related to the number of triangles connected to that position. Actually, the flare density d_i associated to a flare i is computed by: $d_i = 3/\sum_k A_k$, where A_k is the area of the triangle k connected by one of its vertex to the flare i. Then, thanks to a linear interpolation, it is possible to construct the map of the observed flare density $d(x)$ with a color code of density in logarithmic scale (top right panel of Figure 4.9).

To determine the intrinsic flare density (the one really emitted by Sgr A*), I have to correct this observed flare density by the average detection efficiency. If I note $p_{average}(x)$ the average probability to detect a flare located at a point x in the diagram duration/unabsorbed flux (bottom left panel of Figure 4.9), the corrected flare distribution, or intrinsic flare distribution, is $d_{int}(x) = d(x)/p_{average}(x)$, which is thus higher than the observed one. The map of the intrinsic flare density is shown at the bottom right panel of Figure 4.9.

Some comments can be made about these graphs in comparison to the one obtained by Mossoux & Grosso (2017) (Figure 5 of their paper). First, the updated curves of detection probabilities are more squeezed towards the bottom left of the diagram. As the average probabilities are weighted by the exposure, all the observations are taken into account to compute the average detection probabilities. The high non-flaring level observed by XMM-Newton in 2016 has thus a direct impact on the computation of the average flare detection efficiency corresponding to the other non-flaring levels, which is consequently increased. Another comment concerns the observed flare density. The 9 flares that I detected with Chandra have quite moderate duration (between 1000 and 3000 seconds) with rather low mean unabsorbed flux (lower than $12 \times 10^{-12}\,\mathrm{erg\,s^{-1}\,cm^{-2}}$) which explains the increase in the observed density in this part of the map. In a general way, the observed density increased in the left part of the diagram, that is to say for flares with low unabsorbed flux. This trend is thus also reported in the intrinsic flare density. In particular, it is clear that the bottom left part of the map has the highest values. This seems indicate that the X-ray flares coming from Sgr A* are principally of short duration and low unabsorbed flux.

4.4 Study of the X-ray flaring rate

4.4.1 Temporal distribution of the X-ray flares from 1999 to 2018

All the observations from the three telescopes are then combined and the observational gaps between two subsequent observations are removed to create a continuous exposure containing the times of all the observations and especially those of the 123 flares detected. This leads to an exposure of about 119.8 days, which corresponds to 10.35 Ms. This temporal distribution of flares is shown in Figure 4.11. Then, it is needed to correct the temporal flare distribution from the sensitivity bias. For each observation done with XMM-Newton and

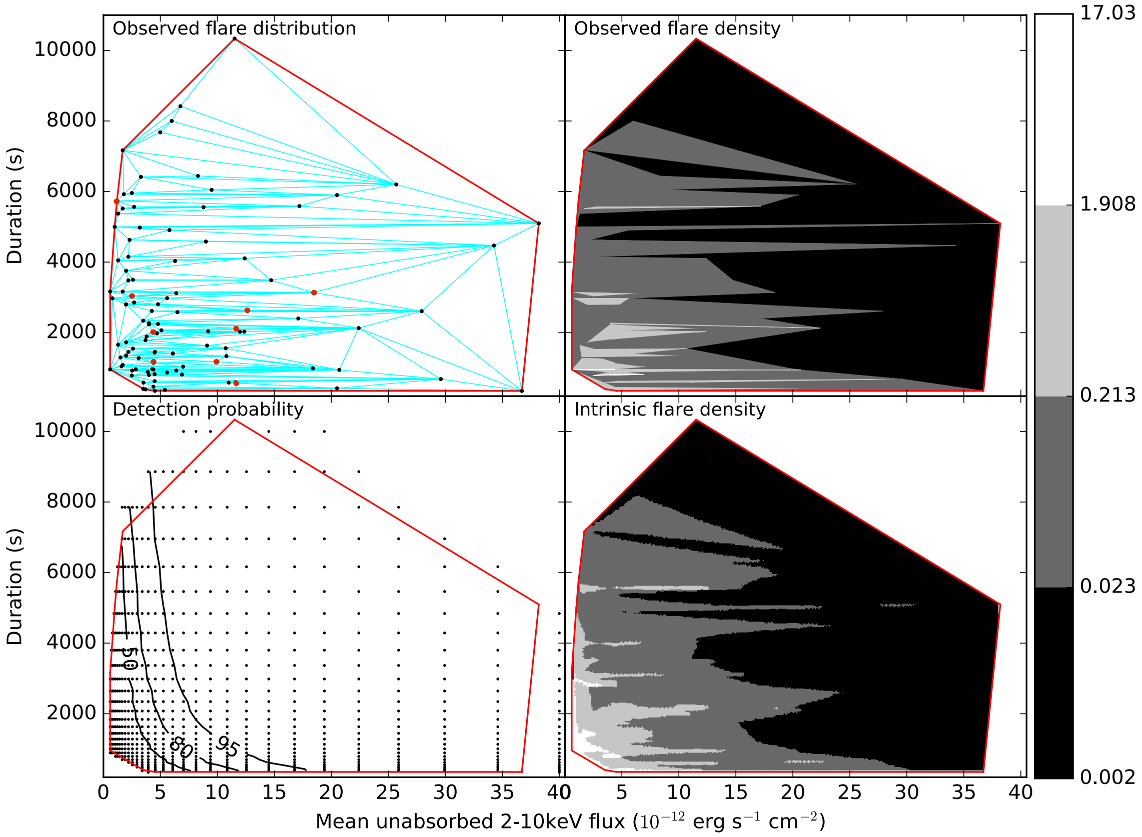

Figure 4.9: Duration-unabsorbed flux distributions of the flares from Sgr A* detected with XMM-Newton and Chandra from 1999 to 2018. *Top left panel*: Observed flare distribution. The black dots correspond to the observed flares before 2016 while the red ones represent the observed flares between 2016 and 2018. The blue lines represent the Delaunay tessellation. *Top right panel*: Observed flare density. The contours are in logarithmic scale with a color code indicated in the right hand side of the figure in units of $10^{10}\,\mathrm{s}^{-1}\,\mathrm{erg}^{-1}\,\mathrm{s\,cm}^{2}$. *Bottom left panel*: Average detection probability of XMM-Newton and Chandra instruments from 1999 to 2018 in percent with the Bayesian blocks algorithm for a false positive rate $p_1 = exp(-3.5)$. The 100% detection contour is not shown because of the quasi null probability to detect a flare by with XMM-Newton in 2016. The dots correspond to the simulation grid (100 simulations for each dot). *Bottom right panel*: Intrinsic flare density corresponding to the observed flare density corrected from the average detection probability. The contours are in the same logarithmic scale than in the top right panel.

Table 4.4: Non-flaring levels for the first part of 2016.

	Edges of the range[a] (count s^{-1})	Non-flaring level (count s^{-1})
Range 1	0 - 0.088	0.044
Range 2	0.088 - 0.179	0.134
Range 3	0.179 - 0.411	0.295
Range 4	0.411 - 1.062	0.737

Notes: [(a)] The edges are defined by the quartiles, which each account for 25% of the observations made before 2016 August 01, as a function of a their count rates. These quartiles are shown in Figure 4.10.

Chandra, the corresponding average flare detection efficiency is computed thanks to the intrinsic flare distribution determined in Section 4.3.2 and the probability of detection of this observation determined in Section 4.3.1. Each point x of the diagram duration/unabsorbed flux of the corresponding non-flaring level corresponds to an intrinsic distribution $d_{int}(x)$ and a detection probability $p(x) \leq 1$. Thus, as mentioned in Section 4.3.2, only a percentage η of the flare intrinsic density is observed. As explained by Mossoux & Grosso (2017), this coefficient is expressed as the ratio between the integral of the intrinsic flare density affected by a weight equal to the considered probability of flare detection and the intrinsic flare density:

$$\eta = \frac{\iint d_{int}(x)\, p(x)\, \mathrm{dx}}{\iint d_{int}(x)\, \mathrm{dx}} \tag{4.1}$$

The determination of the detection probability $p(x)$ for the Swift observations is quite similar to the one done for XMM-Newton and Chandra. For each non-flaring level obtained with Swift, I computed a duration/unabsorbed flux grid with 100 simulated event lists for each point x. Then I applied the Degenaar et al.'s method to detect flares and thus the corresponding detection probability. For the second part of 2016 (after August 01), 2017 and 2018, the non-flaring level is defined as the mean count rate of the considered period. However, the situation is more complex for 2016. For the first part of the year, the activity of the X-ray transients was very fluctuating and it is not possible to determine a unique non-flaring level. Instead, I created four ranges of count rates containing the same number of observations without taking into account the observations with a high correction factor (larger than 3). I first made an histogram, normalized to 1, grouping the observations by bins of count rates before MJD= 57600. At first glance, we see that much more observations have low count rates than high count rates, what was expected. From the histogram, I made a cumulative curve on which I showed up the quartiles. These quartiles allow me to determine the four ranges of count rates containing each 25% of the observations, that is to say 36 or 37 observations by range. The centre of each range will then be used as artificial non-flaring level to establish the probability of flare detection (see Table 4.4 and Figure 4.10 for details of the ranges).

The values of η are shown in Table C.1 of Appendix C. All the values are higher than the ones obtained by Mossoux & Grosso (2017) in their Tables A.1-A.3 because of the non-flaring level observed by XMM-Newton in 2016 and the larger exposures for some levels. Moreover, 9 flares were added to compute the intrinsic distribution which modifies also the old result.

This quantity is then used to correct the observed flaring rate to remove the instrumental dependance. As we do not detect a part of the flares, the real flaring rate should be higher. To reproduce that, it is possible to change all the exposures T using the following expression: $T_{corr} = \eta T$, where T_{corr} is the corrected exposure. Thanks to this operation, I finally get a higher and unbiased flaring rate. Figure 4.12 shows the corrected temporal distribution of flares, without observing gaps, over a total exposure time of 51.3 days instead of 119.8 days. This approach is similar to the operation on the Voronoi cells to take into consideration the livetime during the Bayesian blocks algorithm as seen in Section 4.1.1. It can be noted that the corrected times do not correspond to the one found in Figure 7 from Mossoux & Grosso (2017) because the coefficient η is higher, meaning that less correction has to be applied on the observing times.

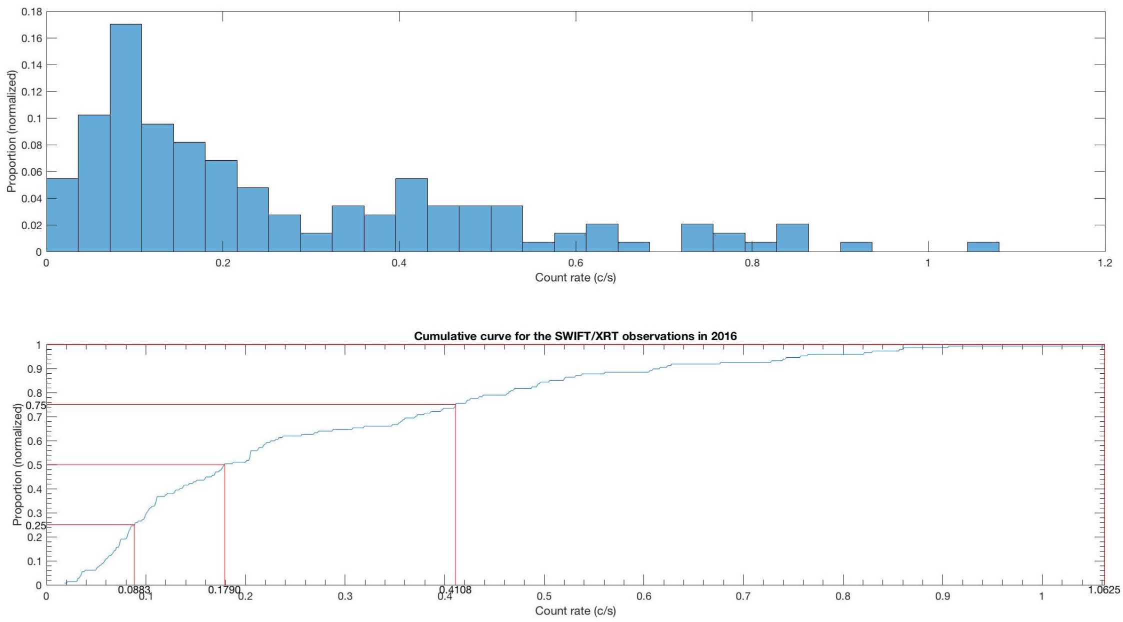

Figure 4.10: Construction of the non-flaring level for the first part of 2016. *Top panel*: Normalized histogram grouping the observations before 2016 August 01 in 30 bins of count rates. *Bottom panel*: Normalized cumulative curve determined from histogram. The central value of each quartile (red) corresponds to the non-flaring level for which I will compute the flare detection probability.

4.4.2 X-ray flaring rate

Once the temporal distribution of the flares is obtained, it is possible to estimate the overall flaring rate of Sgr A* thanks to the Bayesian block algorithm. Then, I will look for the existence of a flux or fluence threshold that could lead to a change in the flaring rate, as done by Mossoux & Grosso (2017).

As for the detection of flares, the distribution of flares must be divided into Voronoï cells containing only one flare. The separation time between two cells is defined as the mean time between the two consecutive flares. Then, the Bayesian blocks method is applied with a false positive rate p_1 equal to 0.05, meaning that the significance of a change point is at least of 95%, and a prior number of change points $ncp\_prior = 7.27$. This last value is computed from the calibration of the algorithm for 123 flares uniformly distributed during 51.3 days. The result of the algorithm is that the flaring rate is constant if one considers all the flares. It corresponds to an intrinsic activity of 2.4 ± 0.2 flares per day. This value is lower than the one estimated by Mossoux & Grosso (2017), even considering the uncertainties. However, it still remains higher than the one obtained by Neilsen et al. (2013) since I did the correction from the sensitivity bias.

I then looked for a flux threshold. I followed the method used by Mossoux & Grosso (2017) to do that. This consists in two approaches. The first one is a top-to-bottom search where one applies the Bayesian blocks on the corrected temporal distribution of flares with a false positive rate $p_1 = 0.05$. If no change point is detected, the flare with the highest flux is removed from the list, while keeping the total exposure time. Then, the Voronoï cells are updated and the Bayesian blocks algorithm is again applied after the new calibration corresponding to the new number of flares done. This iterative process stops when a change point is found or if all the flares are removed from the list. The second approach is called bottom-to-top search and is similar to the first search but instead of removing the flare with the highest flux, I remove the flare with the lowest flux.

The top-to-bottom search detected a change of flaring rate at 36.6 days (corrected) that is to say between the flares of 2013 May 25 and 2013 July 27. This is found with the Bayesian blocks algorithm associated to a false positive rate $p_1 = 0.05$ and to the prior number of change points $ncp\_prior = 6.1$. With this approach, only the 72 less luminous flares remain with a flux lower than $6.4 \times 10^{-12}\,\mathrm{erg\,s^{-1}\,cm^{-2}}$. The resulting Bayesian blocks show a decrease in the flaring rate from 1.7 ± 0.2 to 0.5 ± 0.2 flares per day (top panel of Figure 4.13). The

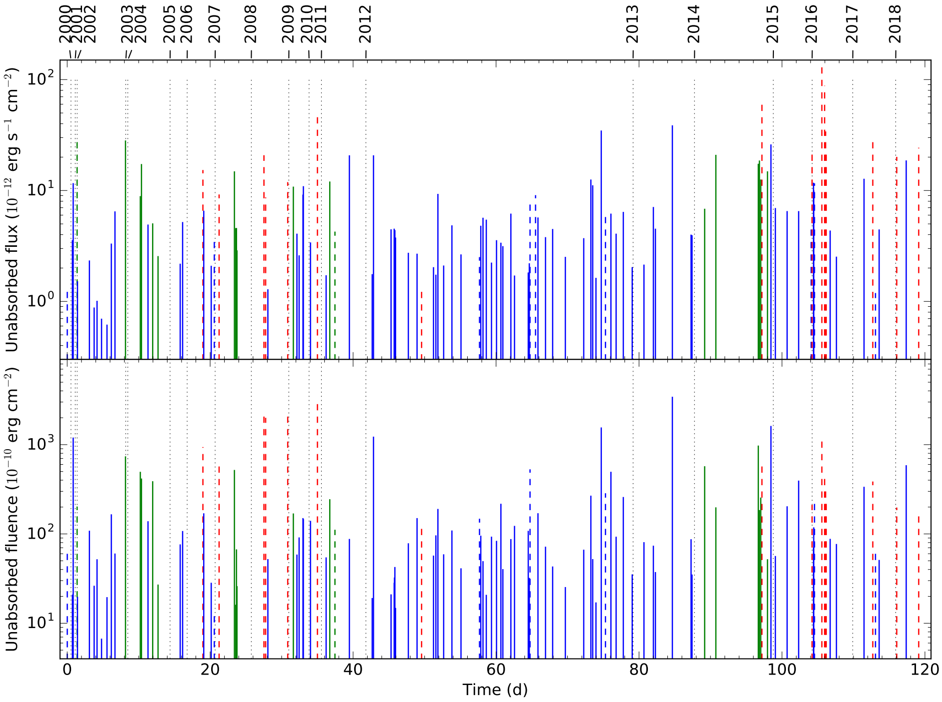

Figure 4.11: Temporal distribution the X-ray flares fluxes and fluences. The vertical lines represent the arrival time of the flares, without observing gaps and with the correction of the average flare detection efficiency. The start time of the first observation of each year is representing by a dotted vertical line. The dashed lines are the flares that started before the beginning of the observation or that ended after the end of the observation. They are thus just lower or upper limits on the flare flux and fluence. Each color corresponds to a telescope: blue for Chandra, red for Swift and green for XMM-Newton. *Top panel:* Mean unabsorbed flux distribution. *Bottom panel:* Mean unabsorbed fluence distribution.

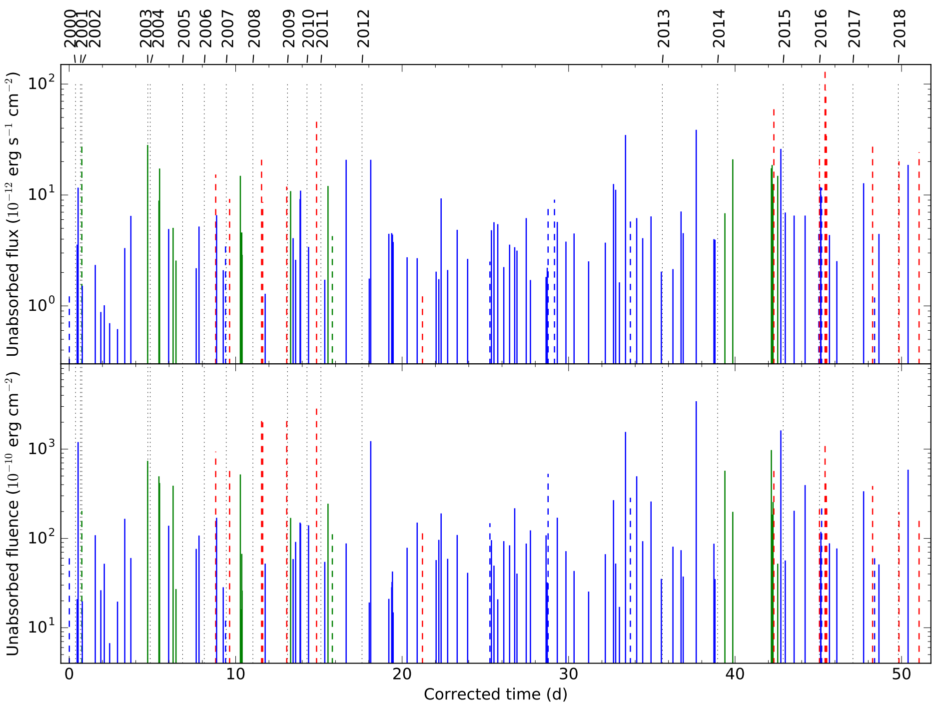

Figure 4.12: Temporal distribution of the X-ray flares fluxes and fluences with corrected observing times. See caption of 4.11 for details.

first block contains 64 of the 72 less luminous flares, while the second block gathers the 8 other flares. Then, the false positive rate is decreased in order to determine the significance of this detection. Until $p_1 = 0.001$ this change is found, leading to a significance of $1 - p_1 = 99.9\%$.

Then, I performed the bottom-to-top search. A change of flaring rate has also been found but at 42.2 days, thus between the two flares observed on 2014 April 02 and on 2014 August 30, for $p_1 = 0.05$ and *ncp_prior* = 7.3. With this method, 52 flares remain with a flux higher than 6.4×10^{-12} erg s^{-1} cm^{-2}. These flares correspond to the most luminous flares. The Bayesian blocks represented in the bottom panel of Figure 4.13 show an increase in the flaring rate from 0.7 ± 0.1 to 2.3 ± 0.5 flares per day. In the first block, there are 31 flares while the second one contains the 21 remaining. By decreasing the value of p_1, I notice that no change point is detected if $p_1 \leq 0.03$. Thus, the probability that the change of flaring rate is not a false one is 97%, a bit less than the one of the top-to-bottom search.

The same study was carried out for the unabsorbed fluences, defined as the flare fluxes times their durations (Figure 4.14). The top-to-bottom search did not reveal any change point for a false positive rate $p_1 = 0.05$ and *ncp_prior* = 6.2, leading to an activity of 2.4 ± 0.2 flares per day. This behaviour is still found when increasing p_1 until 0.5. I can thus conclude that no change of flaring rate occurs, from the point of view of fluence. This result is confirmed by the bottom-to-top search which detects no change point for $p_1 = 0.05$ and *ncp_prior* = 6.2. Hence, considering the fluence, there is no discrimination between the most energetic and the less energetic flares in terms of flaring rate. All the results obtained are summarized in Table 4.5.

Table 4.5: Summary of the change of flaring rate observed between 1999 and 2018

	Top-to-bottom	Bottom-to-top
Flux threshold (10^{-12} erg s^{-1} cm^{-2})	≤ 6.4	≥ 6.4
Number of less and most luminous flares	72	52
Corrected time of change point	36.6	42.2
Date of the change point	2013 May 25 - 2013 July 27	2014 April 02 - August 30
First block (flares per day)	1.7 ± 0.2	0.7 ± 0.1
Second block (flares per day)	0.5 ± 0.2	2.3 ± 0.5
Significance	99.9%	97%
Fluence threshold (10^{-10} erg cm^{-2})	No threshold	No threshold
Block (flares per day)	2.4 ± 0.2	2.4 ± 0.2

4.4.3 Interpretation

My work has the objective to pursue the study of Mossoux & Grosso (2017) and it is thus natural to compare my results with theirs. Actually, my results are a bit different to their work done for the period 1999-2015 although some similarities appear. First, considering the search of a flux threshold, the changes of flaring rate in their study and mine appeared to be quite consistent since the trend remains the same. We can observe a decrease of the faint flaring rate and an increase of the bright one. It has to be noted that the date of the change points do not have to be considered as a strict date because the algorithm is limited by the arrival time of the flares. As a consequence, if only a few flares are detected during a year, the time of change point is determined by a large temporal range. However, the time interval in which the change points are detected are similar for the two studies. Indeed, my top-to-bottom approach gave an interval identical to the one of Mossoux & Grosso (2017) while for the brightest flares, the change of flaring rate occurs in a range whose the upper limit is close to their date. More interesting is the fact that the analyses done in this work do not reveal any change of flaring activity during the search of a fluence threshold which is totally different from what concluded Mossoux & Grosso (2017). An increase of bright flares without increasing fluence seems, at first sight, rather counter-intuitive.

Since there is no discrimination between more and less energetic flares during the period 1999-2018, it can be postulated that no additional matter was included in the accretion flow by the passage of the DSO in April 2014 because the accreted mass is directly related to the energy (see Section 1.3.3). This seems consistent with the fact that the DSO is not a pure gas cloud that would be disrupted and added to the accretion flow. Moreover,

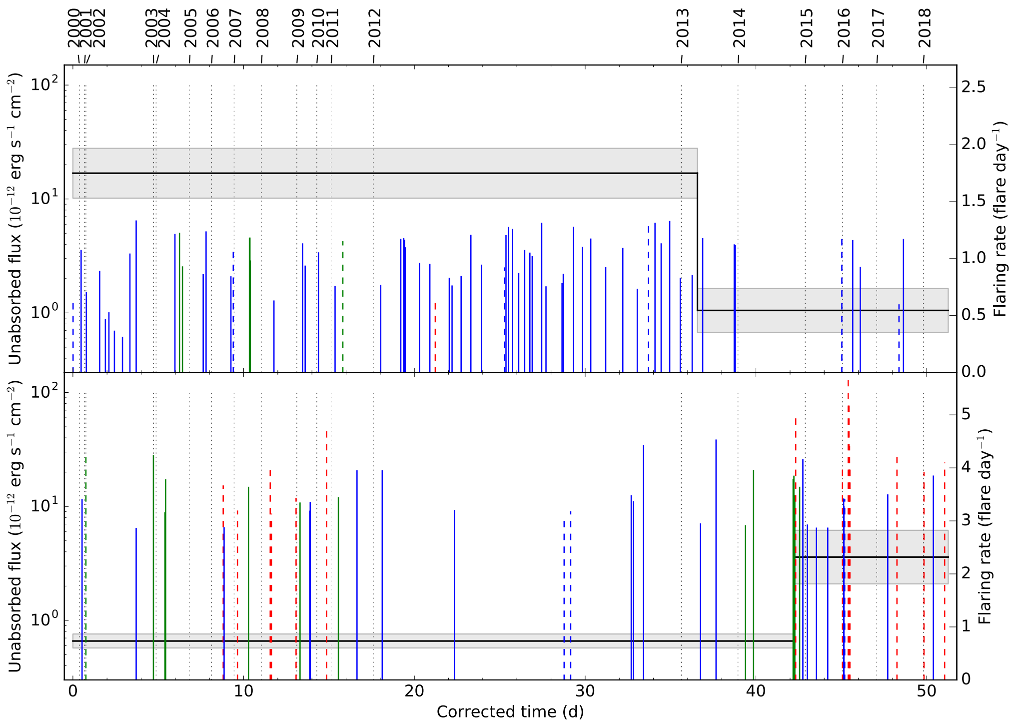

Figure 4.13: X-ray flaring rate from 1999 to 2018 for the less and most luminous flares. This was computed thanks to the Bayesian block algorithm with a top-to-bottom approach (*top panel*) and a bottom-to-top approach (*bottom panel*). The resulting flaring rate are indicated by the black line with their uncertainties represented by the grey boxes. The flux thresholds are given in Table 4.5. See caption of Figure 4.11 for the description of the flares.

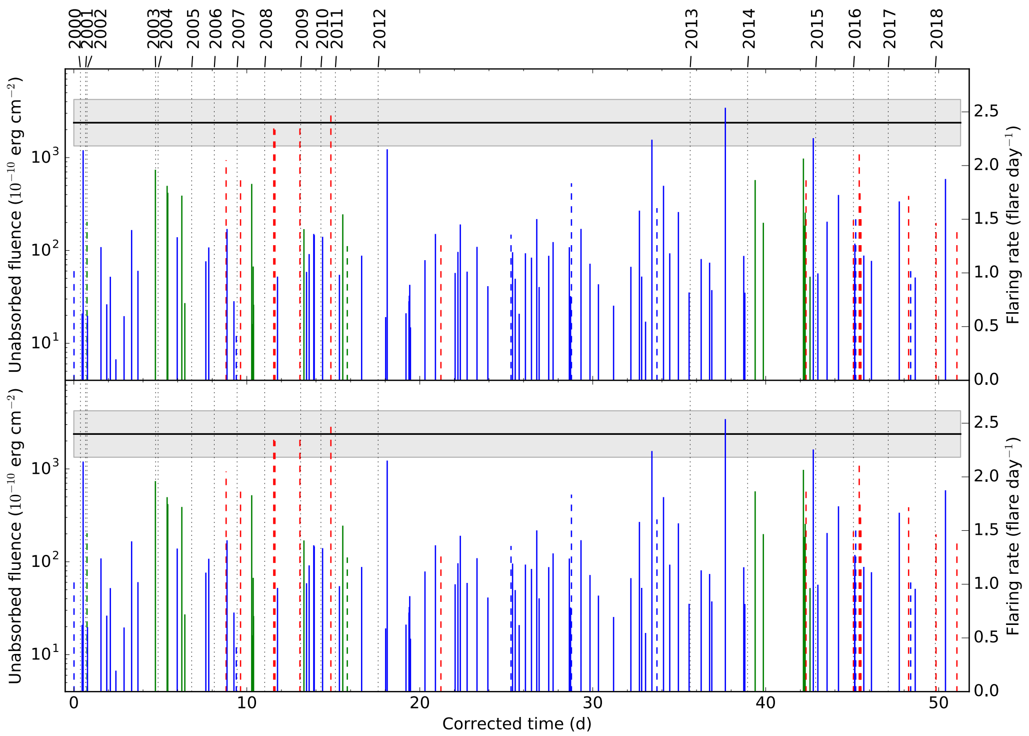

Figure 4.14: X-ray flaring rate from 1999 to 2018 for the less (*top panel*) and most energetic (*bottom panel*) flares. The two graphs are identical because no fluence threshold has been detected, indicating that from this point of view no change in the activity of Sgr A* occurred. See caption of Figure 4.13 for details.

Mossoux et al. (2016) also indicated that if material from the DSO was accreted onto Sgr A*, the increase of flux would appear at the end of 2017 or after, which is clearly not the case. Then, the change of flaring rate concerning the most luminous flares have to be explained rather by a change in the mechanisms that produce the X-ray flares.

In a case of the RIAF model proposed by Yuan et al. (2003), the flare time-scale t_f is related to the accretion time-scale at $10\,R_S$ or by the Alfvén crossing time of magnetic loops in this region. Yuan et al. (2003) made a link between the magnetic field strength and the accretion rate $\dot{M}$ which is directly proportional to the flux F as explained in Section 1.3.3:

$$B \propto \dot{M}^{1/2} \propto F \tag{4.2}$$

These relations illustrate that if B or $\dot{M}$ increases then the flux will increase as well. Hence, a change in the magnetic field strength or in the accretion rate could be a clue to explain why there are more bright flares.

In the case where the flares are produced by synchrotron emission, Yuan et al. (2003) indicated that the flare time-scale should be equal to the synchrotron cooling time t_{cool}, and we find a similar relation between t_f and B:

$$t_f \approx t_{cool} \propto B^{-3/2} \tag{4.3}$$

Assuming that the flares are due to synchrotron emission as it seems indicated by recent studies (Dodds-Eden et al., 2009; Barrière et al., 2014; Ponti et al., 2017), an increase in B will lead to more bright flares with a lower duration. Then the fluence, which is defined as the product between the duration of the flare and its flux, remains almost constant. Previous works suggest that the magnetic field strength seems to play a major role in the creation of bright flares (Ponti et al. 2017; Kawashima et al. 2017). For instance, Kawashima et al. (2017) explained that if the magnetic field is amplified, the luminosity of the X-ray flares will increase if they are due to magnetic reconnection during which the electrons take the amplified magnetic energy to be accelerated. My study seems to go in that direction by indicating that the observed change of flaring rate could be due to a change in the overall magnetic field, assuming a synchrotron emission. Another possibility, still linked to the magnetic field, is that the spatial distribution of flares has changed. For instance, if less flares are created where the magnetic field strength is low (far from Sgr A*) while more flares occur where it is strong (close to the black hole), one could apply the same reasoning to explain Figures 4.13 and 4.14.

Another scenario that could be envisaged is the one of the tidal disruptions of asteroids (Zubovas et al., 2012). In this case, the increase of luminosity is due to the fact that the tidal disruption of asteroids will be accompanied by the creation of emitting particles. However, the asteroids will not modify the accretion rate neither the mass of the accretion disk since the typical mass of an asteroid is about 3 orders of magnitude smaller than the one of the accretion flow (Zubovas et al., 2012). Then the energy, proportional to the mass of the accretion disk, could remain more or less constant (see Section 1.3.3). It seems thus possible via this mechanism to produce flares brighter without significant change in the fluence. From the study of Zubovas et al. (2012) and my results, I can look at the validity of the model to explain the origin of the flares.

First, Zubovas et al. (2012) estimated that the total mass of asteroids per star $M_{a,t}$, close to Sgr A* can be parametrized by a normalization factor m_5 that should be higher but close to 1. The expression of $M_{a,t}$ is then:

$$M_{a,t} = 10^{-5}\, m_5\, M_\odot \tag{4.4}$$

Assuming that we know the stellar tidal disruption rate close to Sgr A*, $\dot{N}_*$, the tidal disruption rate for asteroids whose size is larger than 10 km can be evaluated. It is approximately equal to the product of $\dot{N}_*$ and the number of asteroids per star f_a:

$$\frac{\mathrm{d}N}{\mathrm{d}t} \approx \dot{N}_*\, f_a \approx 0.6 \left(\frac{\dot{N}_*\, m_5}{10^{-5}\ \mathrm{yr}^{-1}}\right) \mathrm{day}^{-1} \tag{4.5}$$

Zubovas et al. (2012) introduced a parameter q to express the differential distribution of asteroids $n(r)$ whose the radius size is comprised between r and $r + \mathrm{d}r$:

$$n(r)\,\mathrm{dr} = n_0 \left(\frac{r}{r_0}\right)^q \tag{4.6}$$

Knowing the luminosity of the flares and the parameters m_5 and q, it is possible to estimate the flaring rate for a given flare luminosity but also to evaluate the size r of the asteroids responsible of the flare:

$$\dot{N} \approx 8\, m_5\, L_{34}^{\frac{q+1}{3}}\ \mathrm{day}^{-1} \tag{4.7}$$

$$r \approx 10\, \xi_1^{-1/3}\, R_{au}^{1/2}\, L_{34}^{1/3}\ \mathrm{km} \tag{4.8}$$

Where L_{34} is the luminosity expressed in $10^{34}\,\mathrm{erg\,s^{-1}}$ units, ξ_1 is the fraction of the mass of the asteroid converted into flares, assumed close to 1, and R_{au} is the distance from Sgr A* where the asteroid is evaporated in astronomical units, assumed close to 1 au.

By equalizing Equation (4.5) and Equation (4.7), I obtain that:

$$\dot{N}_* = 1.33 \times 10^{-4}\, L_{34}^{\frac{q+1}{3}}\ \mathrm{yr}^{-1} \tag{4.9}$$

I first assume that all the flares are due to such a mechanism to determine the parameters m_5 and q consistent with my values. To do that, I first consider the median flux of the observed flares since the distribution is not Gaussian: $F_{median} = 4.99{\times}10^{-12}\,\mathrm{erg\,s^{-1}\,cm^{-2}}$, which corresponds to a luminosity $L_{median} = 3.8{\times}10^{34}\,\mathrm{erg\,s^{-1}}$. In addition, I assume that $\dot{N}_* = 5 \times 10^{-5}\,\mathrm{yr^{-1}}$, which is an intermediate value between the one found by Alexander (2005) and the one proposed by Zubovas et al. (2012). Injecting these values in Equation (4.5) and Equation (4.9), I find $m_5 = 0.8$ and $q = -3.19$. This value of m_5 is a bit lower than the one proposed by Zubovas et al. (2012) but q is well comprised between -4 and -3 as expected by the author.

A change in the size of the asteroids or in the parameters m_5 and q could be responsible of the change of flaring rates. That is what will be developed hereafter.

Size of the asteroids

It is possible to determine the size of the asteroids responsible of the brightest and faintest flares. Since the flux threshold is equal to $6.4 \times 10^{-12}\,\mathrm{erg\,s^{-1}\,cm^{-2}}$ for the two categories, one can apply Equation (4.8) with the corresponding luminosity. This gives that the asteroid should be larger than 17 km to produce the more luminous flares and smaller for the faintest ones.

Parameters m_5 and q

I now investigate how the changes of flaring rate could be explained by a change in the parameters m_5 and q. Actually, I looked for a couple (m_5, q) that could explain the flaring rate of both brightest and faintest flares before the change points and then another couple for the flaring rates after the change points. I thus computed the luminosity corresponding to a given couple (m_5, q) thanks to Equation (4.7) for the four flaring rate. Once done, I obtained a domain in the (m_5, q) space that explains the brightest flares, that is to say with a flux larger than $6.4 \times 10^{-12}\,\mathrm{erg\,s^{-1}\,cm^{-2}}$, or a domain for the faintest ones with a flux lower than this threshold.

For the situation before the change points, the bright flaring rate was about 0.7 flares per day while the faint one was equal to 1.7 flares per day. Using these values, I obtained the two graphs in Figure 4.15. The brightest flares are located above the red dashed line in the left panel while the faintest ones are located below in the right panel. We can see that the two domains intersect, suggesting that both initial flaring rates could be explained with this model for a couple (m_5, q) belonging to this intersection. However, one can see that the values of m_5 and q that I derived for the overall flaring rate do not belong to the intersection of the two domains before the change points. It appears that they are only consistent with the initial brightest flaring rate.

Then, I considered the flaring rates obtained after the change points, that is to say 2.3 flares per day for the brightest one and 0.5 flares per day for the faintest one. I obtained the graphs in Figure 4.16. This time, we can see that the two domains of validity are not intersecting meaning that it is not possible to explain the changes with this model. Indeed, for the brightest ones, one needs to increase both m_5 and q while for the faintest one it is the contrary, one needs to decrease both parameters to values that are not compatible anymore.

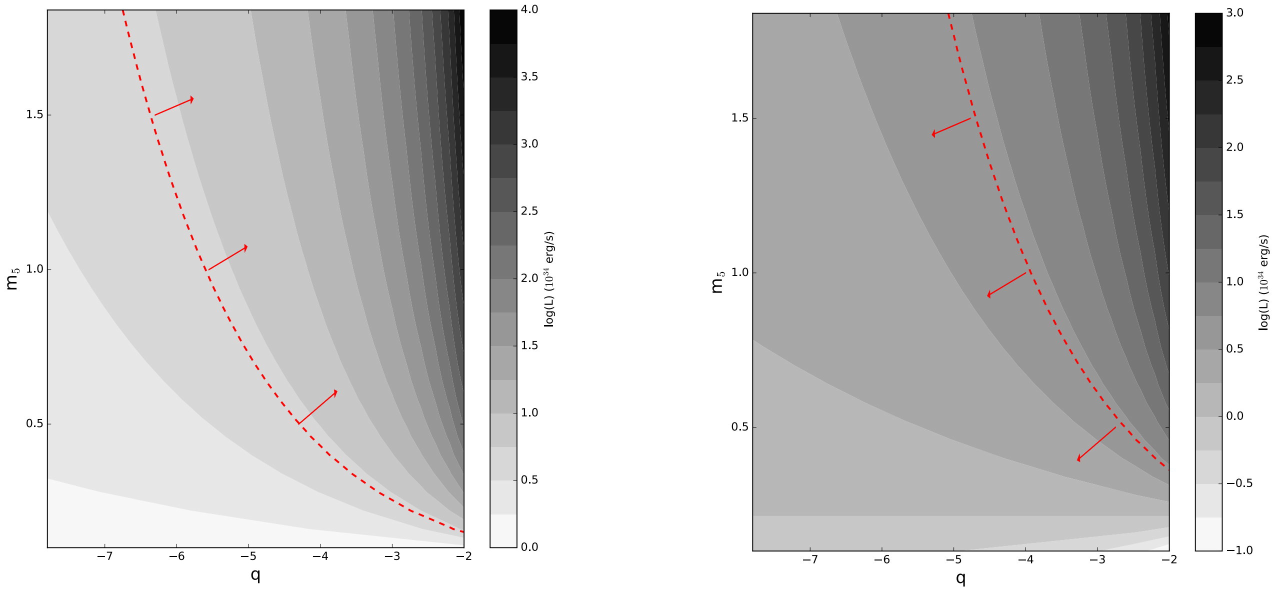

Figure 4.15: Diagrams (m_5, q) before the change points. The red dashed line represents the threshold between brightest and faintest flares. The red arrows indicates what part of the diagram is concerning. Grey scale represents the value of the luminosity in logarithmic scale. *Left panel*: Plot for a flaring rate of $\dot{N} = 0.7$ corresponding to the brightest flares before 2014 April 02. *Right panel*: Plot for a flaring rate $\dot{N} = 1.7$ corresponding to the faintest flares before 2013 May 25.

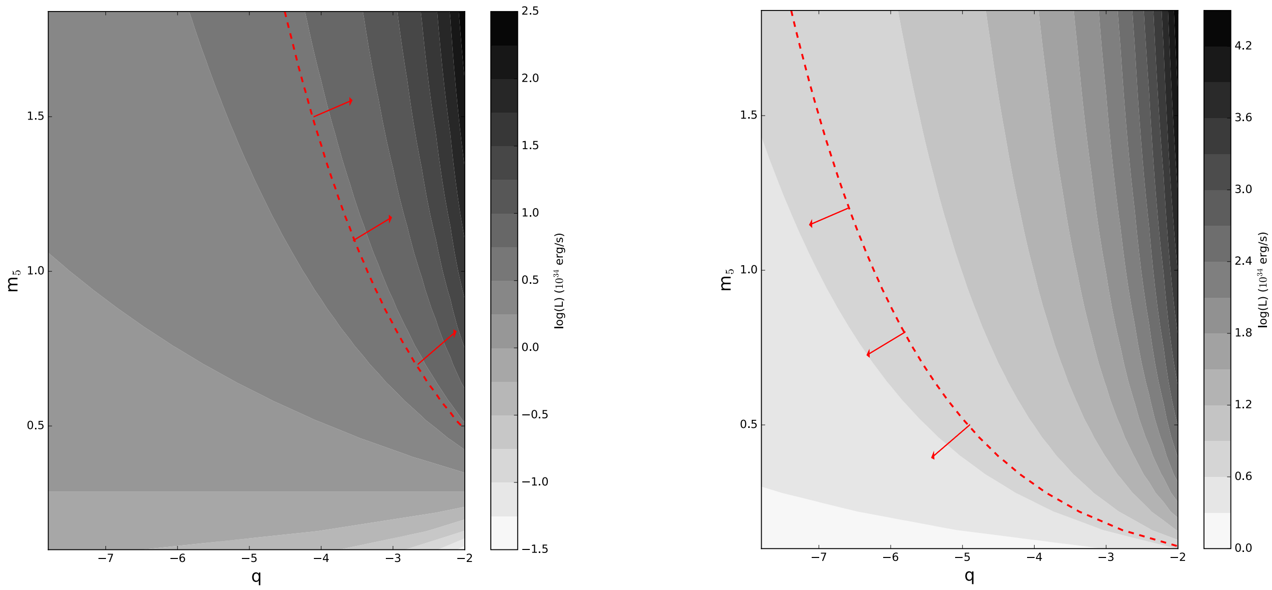

Figure 4.16: Diagrams (m_5, q) after the change points. The red dashed line represents the threshold between brightest and faintest flares. The red arrows indicates what part of the diagram is concerning. Grey scale represents the value of the luminosity in logarithmic scale. *Left panel*: Plot for a flaring rate of $\dot{N} = 2.3$ corresponding to the brightest flares after 2014 August 30. *Right panel*: Plot for a flaring rate $\dot{N} = 0.5$ corresponding to the faintest flares after 2013 July 27.

Chapter 5

Spectral analyses of X-rays flares

This Chapter presents the analyses of the spectra in X-rays. Section 5.1 introduces the basic elements of a spectrum. Then, I describe the method and models used to get the flare spectra in Section 5.2 along with the results for the nine flares detected with Chandra, the two brightest detected with Swift and the search of a change in the hydrogen column density or photon index after the change points in the flaring rate.

5.1 Definitions

A spectrum is an histogram of photons recorded in each spectral channel. The number of channels is not unique, it depends on the instrument. For instance, Chandra has 1024 channels that cover a range of energies from 0.007 to 15 keV while XMM-Newton gets 4096 channels from 0.15 to 15 keV.

The observed spectrum is actually a mix between the emitted spectrum from the source, noted S, the instrument efficiency and the noise from the sensor N. The instrument efficiency depends on two factors: the effective area of the instrument A and the relation between the channel i and the energy (in keV), noted $R(i, E)$. Then, the number of counts observed in the channel i can be expressed:

$$C(i) = T \int_0^\infty R(i, E)\, A(E)\, S(E)\, \mathrm{d}E + N(i) \tag{5.1}$$

The relation $R(i, E)$ is included in a file called the Redistribution Matrix Files (RMFs). In reality, when photons of same energy hit the detector, the number of free electrons generated is not exactly the same, which leads to different recorded energies. The photons have actually a distribution of probabilities of generating a number of these free electrons that are included in the RMFs. In other words, the RMF indicates the channel probability distribution for photons of given energies.

Concerning the effective area A, this last one corresponds to a combination of the collecting surface of the instrument (telescope), the filter transmission, the efficiency of the CCD and the PSF encircled energy fraction. This data are stored in the Ancillary Response Files (ARFs).

5.2 Creation and analyses of the spectra

5.2.1 Flares detected with Chandra

The first step is the creation of the spectra. To extract the ones corresponding to the flares detected with Chandra, I used the software CIAO 4.9 (CALDB 4.7.4). In particular, I used the script named *specextract* in which I specified the source and background regions. In order to correct from the instrumental noise and the diffuse emission around Sgr A*, I chose the same region for the source and the background. However, I restrict the source extraction in a time interval corresponding to the flare duration while the background extraction corresponds to the larger non-flaring period of the observation shifted of 300 seconds from the start or end of a flare. This script also gives the ARF and RMF.

Then, the spectra have to be grouped by bins. One bin is defined when the channel number is high enough to respect a given condition such as a minimum number of counts or a minimum signal-to-noise ratio (S/N) defined as $(C_{src} - C_{bkg} \times ratio)/(C_{src} + C_{bkg} \times ratio^2)^{0.5}$, where *ratio* is the ratio between the exposure time multiplied by the ratio between the regions (background and source+background) and C_{src} and C_{bkg} the number of counts in the source and background spectra, respectively. In this study, if I chose a S/N equal to 3, I get a very low number of spectral bins. That is why I grouped the spectra with the HEASARC task *grppha* with a minimum of 2, 3, 4 or 8 counts per bin depending on the spectrum (see Appendix D).

Once done, I used the HEASOFT task **XSPEC** to fit the spectra and determine some parameters of the flares, such as the photon index and the mean unabsorbed flux. The first step is to initialise the cosmological parameters and the fit parameters (such as the interval). This is done with:

method leven 10 0.01
cosmo 70 0 0.73
xset delta 0.01
systematic 0

Then I loaded the spectrum I wanted to fit as well as the ARM, RMF and the corresponding background spectrum. It is then necessary to reject the unused bins. In particular, I reject the ones that do not fulfil the grouping condition, the ones below 0.2 keV and the ones superior to 10 keV. The next step is the definition of a model to fit the spectrum. I thus followed what Mossoux & Grosso (2017) did that is to say an absorbed power law with scattering by interstellar medium dust. The power law is modelled by **pegpwrlw**. The absorption due to photoionisation by the hydrogen column density N_H along the line of sight is modelled by **tbnew**[1] which is an improved version of the absorption model of Wilms et al. (2000). This new model takes into account the cross sections of the dust, gas and molecules in the ISM (σ_{ISM}) given by Verner et al. (1996) and the abundances provided by Wilms et al. (2000). Typically, this model gives the following relation between the observed spectrum I_{obs} and the emitted one $I_{emitted}$ (Wilms et al., 2000):

$$I_{obs} = e^{-\sigma_{ISM} N_H} I_{emitted} \tag{5.2}$$

The **dustscat** model is used to represent the scattering. This is based on the study of Predehl & Schmitt (1995) that allows to derive a value of the dust scattering optical depth, τ_{scatt}, thanks to ROSAT observations. For their determination of τ_{scatt}, they used the cross sections from Morrison & McCammon (1983) and the abundances from Anders & Ebihara (1982). In the case of **dustscat**, we have $I_{obs} = e^{-\tau_{scatt}} I_{emitted}$ where the dust scattering optical depth is thus of the form (Nowak et al., 2012):

$$\tau_{scatt} = 0.324 \left(\frac{N_H}{10^{22}\,\mathrm{cm}^{-2}}\right)\left(\frac{E}{\mathrm{keV}}\right)^{-2} \tag{5.3}$$

However, Nowak et al. (2012) noticed that these studies predict more metals than the one used in the **tbnew** model. Since metals absorb much more X-ray photons than hydrogen, the fitted hydrogen column density will depend on the choice of abundances and cross sections. Actually, the one predicted by the **dustscat** is 1.5 lower than the one predicted by **tbnew** (Nowak et al., 2012). This has to be taken into account during the fit by forcing that the two computed N_H are linked by a coefficient 1.5.

Finally, for the flares detected with Chandra it is necessary to take into account the pile-up (Nowak et al., 2012). This phenomenon refers as the fact that when several photons hits the CCD during the frame time, they could be recorded as a unique photon of higher energy or are considered as non X-ray photons, thus distorting the spectrum. I then used the pile-up model of Davis (2001). I chose a photon migration parameter $\alpha = 1$ (Mossoux & Grosso, 2017) for a PSF fraction of 95% which corresponds to the source region.

Since **tbnew** and **dustscat** are not present in **XSPEC** by default, I have to load them during the session. Then, I can choose the abundances, cross sections and models with:

abund wilm
xsect vern
model pileup*dustscat*tbnew*pegp

[1] http://pulsar.sternwarte.uni-erlangen.de/wilms/research/tbabs/index.html

The last step is to choose the statistics for fitting the spectrum. Since I have very few bins, it is better to use the Cash statistics (Cash, 1979) than the Chi squared (χ^2) because the distribution would not be represented by a Gaussian function. If I note y_i the bins and M_i the model, the Cash statistics is expressed by $C = 2\sum_{i=1}^{n}(M_i - y_i \log M_i)$ [2]. The choice of this statistics is done through the command **statistic cstat** in **XSPEC**.

Once done, I just had to fit three parameters: N_H, the photon index Γ and the mean unabsorbed flux between 2-10 keV. However, it is better to repeat the **fit** command several times in order to be sure not to be in a local minimum of the function. Then, I computed the uncertainties on the fitted values with **error**. The problem is that when the three parameters are free, the model is not enough constraint and the errors are very large. This explains why in a first approach I set $\Gamma = 2$ and $N_H = 14.3 \times 10^{22}\,\mathrm{cm}^{-2}$ following previous studies (Porquet et al. 2003, 2008; Nowak et al. 2012; Degenaar et al. 2013; Mossoux & Grosso 2017). In addition, this allows me to compare the result (flux only) with the one obtained using the conversion factor mentioned in Section 4.3.2 (Table 5.1) since this factor was computed with these values of N_H and Γ. One can see discrepancies between the two values for the flux, but almost all are consistent within the error bars.

Table 5.1: Comparison of the flare fluxes got by fit or by conversion for Chandra

Start date (UT)	End date (UT)	Converted flux[a] (10^{-12} erg s^{-1} cm^{-2})	Fitted flux[b] (10^{-12} erg s^{-1} cm^{-2})	Adjustment parameter[c]	Relative difference [d] (%)
2016-02-13 12:14:10	2016-02-13 12:24:07	11.55 ± 1.80	$10.36^{+6.72}_{-3.76}$	17.93 (16)	10.3
2016-02-13 13:00:45	2016-02-13 13:20:23	9.92 ± 1.18	$7.61^{+2.14}_{-1.70}$	27.89 (24)	23.3
2016-02-13 15:40:17	> 2016-02-13 16:15:46	11.55 ± 0.89	$9.92^{+2.15}_{-1.75}$	45.53 (40)	14.5
2016-07-12 22:43:30	2016-07-12 23:17:06	4.29 ± 0.59	$1.46^{+0.74}_{-0.57}$	12.46 (5)	66.0
2016-07-18 14:56:24	2016-07-18 15:47:03	2.52 ± 0.44	$1.42^{+0.50}_{-0.42}$	5.13 (12)	43.7
2017-04-11 08:23:04	2017-04-11 09:06:59	12.59 ± 0.89	$11.59^{+2.21}_{-1.81}$	68.77 (68)	7.9
< 2017-07-15 22:54:42	2017-07-16 00:30:18	1.18 ± 0.22	$0.78^{+0.34}_{-0.29}$	4.94 (5)	33.9
2017-07-16 13:10:52	2017-07-16 13:29:56	4.29 ± 0.74	$3.72^{+1.57}_{-1.19}$	8.26 (9)	13.3
2018-04-24 05:00:57	2018-04-24 05:42:27	18.36 ± 0.89	$15.00^{+1.88}_{-1.64}$	203.35 (150)	18.5

Notes: [(a)] The mean unabsorbed flux between 2-10 keV is computed from the count rates obtained with the Bayesian blocks algorithm and converted with the factor 148.1×10^{-12} erg s^{-1} cm^{-2}/count s^{-1}; [(b)] The mean unabsorbed flux between 2-10 keV is obtained from the fit of the spectrum with an hydrogen column $N_H = 14.3\times10^{22}\,\mathrm{cm}^{-2}$ and a photon index $\Gamma = 2$; [(c)] This column shows C and between brackets the number of degrees of freedom; [(d)] This express the discrepancy between the two values of flux: it is computed by $|Flux_{converted} - Flux_{fitted}|/Flux_{converted}$

Then, I set only the value of the hydrogen column density and let free the photon index. The values of the mean unabsorbed flux and of Γ are shown in Table 5.2. Most of the derived photon indexes are larger than 2 but include this value within the errors, that can be very large due to the low number of bins. However, the first and the ninth ones remain higher than $\Gamma = 2$. Concerning the mean unabsorbed fluxes, we see that the values are close to the ones obtained when N_H and Γ were set to a fix value. It has to be noted that for two flares **XSPEC** was unable to compute the errors on the flux and on the photon index, thus I decided not to consider these results (dotted line in Table 5.2).

The spectra of the flares fitted with $\Gamma = 2$ and $N_H = 14.3 \times 10^{22}\,\mathrm{cm}^{-2}$ are shown in Appendix D.

5.2.2 Flares detected with Swift

Because of the small amount of collected photons with Swift, only two spectra have been fitted between 2016 and 2018. They correspond to the two brightest ones detected on 2016. To create the spectra, it is necessary to use the HEASARC task named **XSELECT**. Unlike the software used for Chandra, this one does not create automatically the ARF. It is thus needed to make use of *xrtmkarf*. The RMF are found on the website `http://www.swift.ac.uk/analysis/xrt/rmfarf.php`. With the task **grppha**, the spectra of the source are grouped with a minimum of 1 counts per bin from 0.1 keV. The spectra of the background are associated to the one of the source but not grouped. In the case of these observations, the background region is a annulus around the source region.

Then, the procedure in **XSPEC** is exactly the same than the previous one, but I did not include the pile-

[2]The χ^2 is expressed by $\sum_{i=1}^{n}(y_i - M_i)^2/\sigma^2$, where σ is the errors on the bins.

Table 5.2: Flares fluxes and photon index for a fixed hydrogen column

Start date (UT)	End date (UT)	Photon index[a]	Flux[a] (10^{-12} erg s^{-1} cm^{-2})	Adjustment parameter[b]
2016-02-13 12:14:10	2016-02-13 12:24:07	$4.22^{+1.74}_{-1.50}$	$12.01^{+8.53}_{-4.63}$	11.87 (15)
2016-02-13 13:00:45	2016-02-13 13:20:23	$1.99^{+1.03}_{-0.97}$	$7.61^{+2.19}_{-1.71}$	27.89 (23)
2016-02-13 15:40:17	> 2016-02-13 16:15:46	$2.30^{+0.60}_{-0.59}$	$9.80^{+2.11}_{-1.71}$	44.92 (39)
2016-07-12 22:43:30	2016-07-12 23:17:06	......	....	....
2016-07-18 14:56:24	2016-07-18 15:47:03	$2.34^{+1.35}_{-1.37}$	$1.43^{+0.51}_{-0.42}$	4.96 (11)
2017-04-11 08:23:04	2017-04-11 09:06:59	$1.96^{+0.53}_{-0.52}$	$11.63^{+2.31}_{-1.85}$	68.75 (67)
< 2017-07-15 22:54:42	2017-07-16 00:30:18	$3.69^{+2.68}_{-2.37}$	$0.90^{+1.13}_{-0.38}$	3.54 (4)
2017-07-16 13:10:52	2017-07-16 13:29:56	......	....	....
2018-04-24 05:00:57	2018-04-24 05:42:27	$2.69^{+0.39}_{-0.38}$	$14.87^{+1.83}_{-1.60}$	194.47 (149)

Notes: $^{(a)}$ The photon index and the mean unabsorbed flux between 2-10 keV are obtained by fitting the spectrum with an imposed hydrogen column $N_H = 14.3 \times 10^{22}\,\mathrm{cm}^{-2}$. A dotted line indicates that the errors were not calculable by letting the parameters free; $^{(b)}$ This column shows C and between brackets the number of degrees of freedom.

Table 5.3: Comparison of the two brightest flares detected by Swift in 2016

Start date (UT)	End date (UT)	Converted flux[a]	Fitted flux[b] (10^{-12} erg s^{-1} cm^{-2})	Adjustment parameter[c]
2016-03-24 19:29:41	2016-03-24 19:43:54	141.8 ± 27.6	$146.7^{+18.8}_{-17.7}$	242.7 (243)
2016-05-05 00:36:01	2016-03-24 00:43:53	88.1 ± 21.4	$90.9^{+21.3}_{-19.4}$	79.9 (96)

Notes: The mean unabsorbed flux between 2-10 keV is computed from the count rates obtained with the Bayesian blocks algorithm and converted with the factor $293.5 \times 10^{-12}\,\mathrm{erg\,s^{-1}\,cm^{-2}/count\,s^{-1}}$; $^{(b)}$ The mean unabsorbed flux between 2-10 keV is obtained from the fit of the spectrum with an hydrogen column $N_H = 14.3 \times 10^{22}\,\mathrm{cm}^{-2}$ and a photon index $\Gamma = 2$; $^{(c)}$ This column shows C and between brackets the number of degrees of freedom.

up model. Table 5.3 presents the values obtained for the two flares when the photon index and the hydrogen column density are set to a given value ($\Gamma = 2$ and $N_H = 14.3 \times 10^{22}\,\mathrm{cm}^{-2}$) while Figure 5.1 shows the fits.

Then, I tried to fit the data letting free the three parameters. This gives me the results in Table 5.4 and the fits shown in Figure 5.2. We can see that the errors are quite high for the second flare. In particular, the value of the mean unabsorbed flux seems too high compare to the value found before and the errors on the photon index and N_H are more than 100% of the value. Nevertheless, the parameters of the two flares seem consistent with the converted flux and the studies of Nowak et al. (2012) or Ponti et al. (2017) indicating that they are truly emitted by Sgr A*.

Table 5.4: Parameters of the two brightest flares detected with Swift in 2016

Start date (UT)	End date (UT)	N_H[a] (10^{22} cm^{-2})	Photon index[a]	Flux[a] (10^{-12} erg s^{-1} cm^{-2})	Adjustment parameter[b]
2016-03-24 19:29:41	2016-03-24 19:43:54	$10.6^{+3.2}_{-2.6}$	$2.94^{+0.86}_{-0.73}$	$124.3^{+59.7}_{-29.8}$	190.8 (241)
2016-05-05 00:36:01	2016-03-24 00:43:53	$20.7^{+21.9}_{-13.4}$	$1.9^{+2.6}_{-1.9}$	$128.3^{+57.0}_{-56.8}$	76.3 (94)

Notes: $^{(a)}$ The hydrogen column density, the mean unabsorbed flux between 2-10 keV and the photon index are obtained via the fit of the spectrum with an hydrogen column $N_H = 14.3 \times 10^{22}\,\mathrm{cm}^{-2}$; $^{(b)}$ This column shows C and between brackets the number of degrees of freedom.

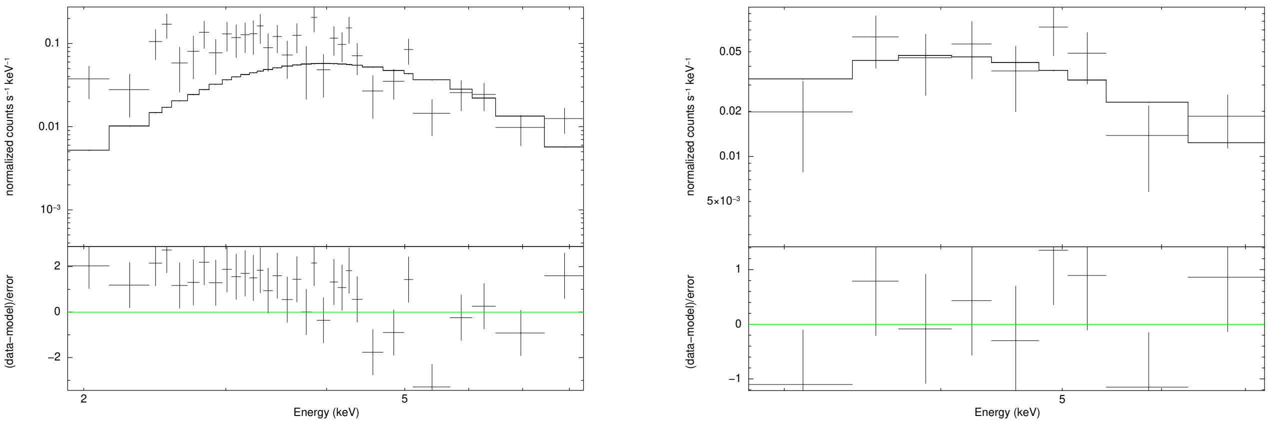

Figure 5.1: Fit of the two brightest flares detected with Swift with $N_H = 14.3 \times 10^{22}$ cm^{-2} and $\Gamma = 2$ imposed. The spectra are grouped with a minimum of 10 counts per bin for clarity but the model is the one described in the text. *Left panel*: Fit of the flare occurring on 2016 March 24. *Right panel*: Fit of the flare occurring on 2016 May 05.

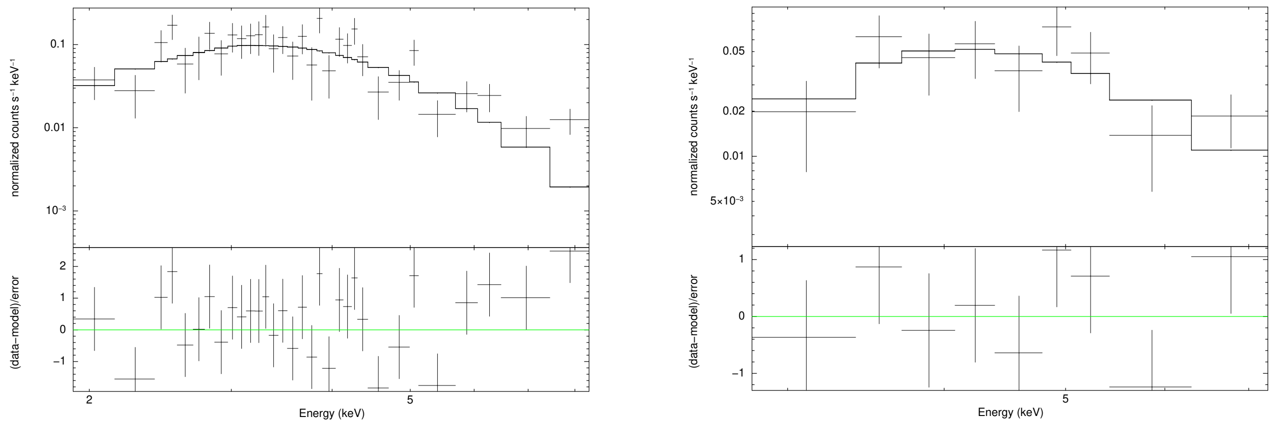

Figure 5.2: Fit of the two brightest flares detected with Swift with N_H, Γ and the flux let free. The spectra are grouped with a minimum of 10 counts per bin for clarity but the model is the one described in the text. *Left panel*: Fit of the flare occurring on 2016 March 24. *Right panel*: Fit of the flare occurring on 2016 May 05.

Table 5.5: Parameters N_H and Γ obtained with global fitting

	Overall				Increase				Decrease			
	Before $\leq$ 2013-09-14		After $\geq$ 2014-03-10		Before $\leq$ 2014-04-02		After $\geq$ 2014-08-30		Before $\leq$ 2013-10-28		After $\geq$ 2013-10-28	
N_H (10^{22} cm^{-2})	$13.87^{+0.92}_{-0.32}$		$16.32^{+1.00}_{-2.88}$		$14.30^{+0.70}_{-0.40}$		$13.44^{+3.35}_{-1.19}$		$18.90^{+10.5}_{-6.97}$		$13.15^{+12.7}_{-7.16}$	
Γ	$1.81^{+0.14}_{-0.10}$	$1.86^{+0.09}_{-0.09}$	$2.52^{+0.64}_{-0.53}$	$2.21^{+0.18}_{-0.18}$	$1.89^{+0.12}_{-0.11}$	$1.87^{+0.09}_{-0.09}$	$2.09^{+0.54}_{-0.31}$	$2.18^{+0.19}_{-0.19}$	$2.33^{+1.99}_{-0.99}$	$1.78^{+0.23}_{-0.23}$	$1.67^{+2.24}_{-1.55}$	$2.48^{+1.23}_{-1.36}$

Notes: The grey cells indicate that the hydrogen colum density N_H is set to 14.3×10^{22} cm^{-2}. The dates correspond to the first and last flare of the group. Two flares were detected on 2013 October 28, the first one is included in the "before" column while the second one is included in the "after" column concerning the decrease.

5.2.3 Global fitting of the flare spectra

A last analyse was done to study the variation of the hydrogen column density N_H and the photon index Γ before and after the change points identified in Section 4.4.2. Considering the flares identified with XMM-Newton and Chandra from 1999 I grouped their spectra with a minimum S/N equal to 2 and I kept only the ones with at least 3 bins. The objective is to fit several spectra at the same time with the model defined previously for Chandra imposing the same N_H and Γ for the flares considered. The results are shown in Table 5.5.

In a first approach, I considered all the flares without discrimination on the flux. I separated the ones detected before the first change point from the ones detected after. I let N_H and Γ free. Before the change point, this gives an hydrogen column density consistent with the admitted value of 14.3×10^{22} cm^{-2} and a photon index close to 2. After, one can observe a slight increase in the two parameters but considering the error bars, this remains inside the ones of the first part. However, imposing the value of the hydrogen column leads to an increase in the photon index after the change point but with smaller errors.

The same work has been done considering the brightest flares, that is to say with a mean unabsorbed flux greater than 6.4×10^{-12} erg s^{-1} cm^{-2}. 20 spectra were considered before the change point and 9 after. Once again, we observe a slight increase in the photon index whether the hydrogen column density is set or not. However, we do not see a significant change in the value of N_H if this one is let free during the fit.

Finally, I repeated this work with the faintest flares, with a flux lower or equal to 6.4×10^{-12} erg s^{-1} cm^{-2}. Before the change point, 26 spectra are considered and we found that N_H is a bit high compared to 14.3×10^{22} cm^{-2} but the error bars are also large thus this last value remains within the errors. After the change point, only two spectra remains which leads to high uncertainties. The N_H decreases to a closer value but still with large errors. One thing looking surprising is that the photon index decrease if I let N_H free whereas it increases if N_H is fixed. In all cases, the value $\Gamma = 2$ is comprised in the errors obtained with the fit.

It could be noted that a change in the photon index after the change point detected for the flaring rates could be in agreement with the scenario of tidal disruption of asteroids. Indeed, this change can reveal an evolution of the electron distribution that could be caused by the asteroids.

Chapter 6

Conclusion

The goal of this Master thesis was to pursue the work initiated by Mossoux & Grosso (2017) about the temporal distribution of the X-ray flares coming from the supermassive black hole Sgr A* at the centre of the Milky Way. To do that, I first had to become acquainted with the target and especially with its quiescent and flaring emission in X-rays but also in other wavelengths such as NIR since flares can be observed in both and could be related to each other. I thus devote time to deal with the subject in depth through literature in order to have a good understanding of the actual knowledge and of the issue.

Then I collected the data of three space telescopes (XMM-Newton, Chandra and Swift) concerning Sgr A* between 2016 and 2018. I had to do some researches about these telescopes to understand their differences that have a direct impact on the data reduction but also on the analyses that follow. Thanks to dedicated tools I reduced the X-ray observations to get the corresponding event lists and light curves of the target.

Once the light curves created for XMM-Newton and Chandra observations, I searched for X-ray flares in the observations. I thus used the two-steps Bayesian blocks algorithm developed by Mossoux et al. (2015a,b), based on the original Bayesian block algorithm proposed by Scargle (1998) then improved by Scargle et al. (2013), which performs an automatic detection of significant changes in a temporal series while correcting the series from the background. Concretely, the algorithm divide the time series into several blocks of different count rates that allows to identify significant increases of flux corresponding to flares. Unluckily, two X-ray transients were active during the first part of 2016 that contaminated the only XMM-Newton observation of Sgr A* I used. However, I detected 9 flares in the 16 observations done by Chandra.

The detection of flares for the Swift observations is different due to the fact that the telescope observes almost daily the Galactic Centre but only for short durations, generally less than the one of a flare. In a normal case, where no X-ray sources are active close to the black hole in projected distance, we can apply the method proposed by Degenaar et al. (2013). It consists in computing the mean count rate of each observation, then to compute the mean count rate of a yearly campaign with its associated standard deviation. An observation for which its mean count rate minus its standard deviation is higher than the yearly mean count rate plus three times the yearly standard deviation is considered as a flare. This has been applied for the period between 2016 August 01 and 2016 November 01, as well as for the years 2017 and 2018. Thanks to this method, one flare has been detected in 2017 and two others in 2018. However the presence of active transients in the first part of 2016 has forced me to get around the problem by other means. I thus compared the significance of the Sgr A* observations mean count rates with the tail of the PSF of the very bright transients. This allows me to detect four flares. A total of 16 flares have been detected between 2016 and 2018 thanks to Chandra and Swift observations.

The last steps were to gather these flares to the ones detected between 1999 and 2016 by Mossoux & Grosso (2017) to compute the intrinsic distribution of flares and then to analyse the flaring rate of the more luminous, more energetic, less luminous and less energetic flares without instrumental biases. After correction of the sensitivity bias on the concatenated observational exposures, the Bayesian blocks algorithm was applied to the arrival times of the flares to detect any significant change of flaring rate. A top-to-bottom approach and a bottom-to-top approach have been considered to distinguish less luminous from more luminous flares as well as less energetic from more energetic ones. An increase of the bright flaring rate (flux larger than $6.4 \times 10^{-12}\,\mathrm{erg\,s^{-1}\,cm^{-2}}$) was detected in 2014 while a decrease of the faint one (flux lower than

$6.4 \times 10^{-12}\,\mathrm{erg\,s^{-1}\,cm^{-2}}$) was detected in 2013, which is consistent with the previous study of Mossoux & Grosso (2017). However, regarding the fluence, no change has been detected. That means that we cannot discriminate less and more energetic flares on the basis of the flaring rates. The fact that the energy of flares globally does not change is another clue that could indicate that the DSO was not disrupted during its passage to periapse as mentioned by Valencia-S. et al. (2015).

If the flares are created via synchrotron emission, the change in the flux distribution can be explained by a reorganisation of the spatial distribution of the flares, that is to say that more flares occurs where the magnetic field strength is high (close to the black hole). Another mechanism has been investigated, which is the one proposed by Zubovas et al. (2012) based on the tidal disruption of asteroids. In that case, asteroids will create a population of energetic electrons that will emit X-rays. Then, the change of flaring rate in this model would imply that more large asteroids (larger than 17 km) are disrupted from 2014 although it seems difficult to understand how it is possible. I also showed that this model cannot totally reproduce my results since the changes of flaring rates cannot be explained by a change in the total mass per asteroid and/or a change in the differential distribution of asteroids.

In addition, I performed spectral analyses of the flares detected with Chandra from 2016. I learnt how to extract the spectra of the source and then I used the **XSPEC** software to fit the spectra in order to determine in a first approach the flux of each flare by imposing the hydrogen column density and the photon index thanks to values derived by previous studies (Porquet et al. 2003, 2008; Nowak et al. 2012; Degenaar et al. 2013; Mossoux & Grosso 2017). Then, I let the photon index and the mean unabsorbed flux between 2-10 keV free to compare the value of the photon index with the literature. Globally, my results are consistent with a value of 2 for the photon index as expected. The spectrum of the two brightest flares detected with Swift in 2016 were also fitted to check the value of the flux, the hydrogen column density and the photon index. The results obtained allow to confirm that these flares are actually Sgr A* flares and are not emitted by the active X-ray transients. Finally, a slight increase of the photon index of the flares has been observed after the change of flaring rates for both brightest and faintest flares, which seems indicate a change in the distribution of the energy of the electrons.

My work thus bring new information that could be important for the study of flares from Sgr A*. I first confirm the trend of an increase of bright flaring rate with a decrease of the faint one. In addition, I show that the overall energy of flares does not change which is consistent with the fact that the DSO survived to its passage to periapse. Finally, the changes detected do not rule out the synchrotron emission as origin of X-ray flares, if the magnetic field strength of the accretion disk has changed for instance. It could be interesting to continue this study in the coming years to see if the changes of flaring rate are still present or if the situation come back to the initial state but also to put more constraints on the models of Sgr A* flaring activity that should be able to explain the change of flaring rates in terms of fluxes and the fact that the fluence of the flares does not evolve but also the spectral features.

Bibliography

Aharonian, F., Akhperjanian, A. G., Aye, K.-M., et al., Very high energy gamma rays from the direction of Sagittarius A*, A&A, 425, L13. 2004

Albert, J., Aliu, E., Anderhub, H., et al., Observation of Gamma Rays from the Galactic Center with the MAGIC Telescope, ApJL, 638, L101. 2006

Alexander, T., Stellar processes near the massive black hole in the Galactic center [review article], Physics Reports, 419, 65. 2005

Amôres, E. B., Robin, A. C., & Reylé, C., Evolution over time of the Milky Way's disc shape, A&A, 602, A67. 2017

Anders, E. & Ebihara, M., Solar-system abundances of the elements, Geochimica Cosmochimica, 46, 2363. 1982

Baganoff, F. K., Bautz, M. W., Brandt, W. N., et al., Rapid X-ray flaring from the direction of the supermassive black hole at the Galactic Centre, Nature, 413, 45. 2001

Baganoff, F. K., Corrales, L. R., Neilsen, J., et al., Chandra Position of Galactic Center X-ray Transient Swift J174540.7-290015, The Astronomer's Telegram, 8746. 2016

Baganoff, F. K., Maeda, Y., Morris, M., et al., Chandra X-Ray Spectroscopic Imaging of Sagittarius A* and the Central Parsec of the Galaxy, ApJ, 591, 891. 2003

Balick, B. & Brown, R. L., Intense sub-arcsecond structure in the galactic center, ApJ, 194, 265. 1974

Barrière, N. M., Tomsick, J. A., Baganoff, F. K., et al., NuSTAR Detection of High-energy X-Ray Emission and Rapid Variability from Sagittarius A* Flares, ApJ, 786, 46. 2014

Becklin, E. E. & Neugebauer, G., Infrared Observations of the Galactic Center, ApJ, 151, 145. 1968

Blandford, R. D. & Begelman, M. C., On the fate of gas accreting at a low rate on to a black hole, MNRAS, 303, L1. 1999

Boehle, A., Ghez, A. M., Schödel, R., et al., An Improved Distance and Mass Estimate for Sgr A* from a Multistar Orbit Analysis, ApJ, 830, 17. 2016

Bondi, H., On spherically symmetrical accretion, MNRAS, 112, 195. 1952

Bower, G. C., Broderick, A., Dexter, J., et al., ALMA Polarimetry of Sgr A*: Probing the Accretion Flow from the Event Horizon to the Bondi Radius, ApJ, 868, 101. 2018

Bremer, M., Witzel, G., Eckart, A., et al., The near-infrared spectral index of Sagittarius A* derived from Ks- and H-band flare statistics, A&A, 532, A26. 2011

Brinkerink, C. D., Falcke, H., Law, C. J., et al., ALMA and VLA measurements of frequency-dependent time lags in Sagittarius A*: evidence for a relativistic outflow, A&A, 576, A41. 2015

Brown, R. L., Precessing Jets in Sagittarius A - Gas Dynamics in the Central Parsec of the Galaxy, ApJ, 262, 110. 1982

Brown, R. L. & Lo, K. Y., Variability of the compact radio source at the galactic center, ApJ, 253, 108. 1982

Burkert, A., Schartmann, M., Alig, C., et al., Physics of the Galactic Center Cloud G2, on Its Way toward the Supermassive Black Hole, ApJ, 750, 58. 2012

Caldwell, J. A. R., Avruch, J. M., Metzger, M. R., Schechter, P. L., & Keane, J. J., in Astronomical Society of the Pacific Conference Series, Vol. 30, Variable Stars and Galaxies, in honor of M. W. Feast on his retirement, ed. B. Warner, 111. 1992

Capellupo, D. M., Haggard, D., Choux, N., et al., Simultaneous Monitoring of X-Ray and Radio Variability in Sagittarius A*, ApJ, 845, 35. 2017

Cash, W., Parameter estimation in astronomy through application of the likelihood ratio, ApJ, 228, 939. 1979

Chandra X-ray Center, Chandra Project Science, MSFC, & Chandra IPI Teams, The Chandra Proposer's Observatory Guide, Version 21.0. 2018

Coil, A. L. & Ho, P. T. P., The Dynamics of Molecular Material within 15 PARSECS of the Galactic Center, ApJ, 533, 245. 2000

Corrales, L. R., Mon, B., Haggard, D., et al., The Chandra Dust-scattering Halo of Galactic Center Transient Swift J174540.7-290015, ApJ, 839, 76. 2017

Coti Zelati, F., Rea, N., Turolla, R., et al., Chandra monitoring of the Galactic Centre magnetar SGR J1745-2900 during the initial 3.5 years of outburst decay, MNRAS, 471, 1819. 2017

Davis, J. E., Event Pileup in Charge-coupled Devices, ApJ, 562, 575. 2001

de Vaucouleurs, G. & Buta, R., On the distributions of globular clusters in the Galaxy and in Messier 31, AJ, 83, 1383. 1978

Degenaar, N., Miller, J. M., Kennea, J., et al., The X-Ray Flaring Properties of Sgr A* during Six Years of Monitoring with Swift, ApJ, 769, 155. 2013

Degenaar, N., Reynolds, M. T., Wijnands, R., et al., Continued Swift/XRT observations of the new Galactic center transients SWIFT J174540.2-290037 and SWIFT J174540.7-290015, The Astronomer's Telegram, 9196. 2016a

Degenaar, N., Reynolds, M. T., Wijnands, R., et al., Swift/XRT detection of another active X-ray transient close to Sgr A*, The Astronomer's Telegram, 9109. 2016b

Degenaar, N., Wijnands, R., Miller, J. M., et al., The Swift X-ray monitoring campaign of the center of the Milky Way, Journal of High Energy Astrophysics, 7, 137. 2015

Do, T., Ghez, A. M., Morris, M. R., et al., A Near-Infrared Variability Study of the Galactic Black Hole: A Red Noise Source with NO Detected Periodicity, ApJ, 691, 1021. 2009

Dodds-Eden, K., Gillessen, S., Fritz, T. K., et al., The Two States of Sgr A* in the Near-infrared: Bright Episodic Flares on Top of Low-level Continuous Variability, ApJ, 728, 37. 2011

Dodds-Eden, K., Porquet, D., Trap, G., et al., Evidence for X-Ray Synchrotron Emission from Simultaneous Mid-Infrared to X-Ray Observations of a Strong Sgr A* Flare, ApJ, 698, 676. 2009

Dodds-Eden, K., Sharma, P., Quataert, E., et al., Time-Dependent Models of Flares from Sagittarius A*, ApJ, 725, 450. 2010

Dopita, M. A., Jacoby, G. H., & Vassiliadis, E., A theoretical calibration of the planetary nebular cosmic distance scale, ApJ, 389, 27. 1992

Drake, F. D., A high-resolution radio study of the galactic center., AJ, 64, 329. 1959

Duncan, R. C. & Thompson, C., Formation of very strongly magnetized neutron stars - Implications for gamma-ray bursts, ApJL, 392, L9. 1992

Ebisuzaki, T., Hanawa, T., & Sugimoto, D., Are X-ray bursts really of super-Eddington luminosities?, PASJ, 36, 551. 1984

Eisenhauer, F., Schödel, R., Genzel, R., et al., A Geometric Determination of the Distance to the Galactic Center, ApJ, 597, L121. 2003

Ekers, R. D., van Gorkom, J. H., Schwarz, U. J., & Goss, W. M., The radio structure of SGR A, A&A, 122, 143. 1983

ESA: XMM-Newton SOC, "Users Guide to the XMM-Newton Science Analysis System", Issue 14.0. 2018a

ESA: XMM-Newton SOC, "XMM-Newton Users Handbook", Issue 2.16. 2018b

Falcke, H., in Astronomical Society of the Pacific Conference Series, Vol. 186, The Central Parsecs of the Galaxy, ed. H. Falcke, A. Cotera, W. J. Duschl, F. Melia, & M. J. Rieke, 113. 1999

Falcke, H. & Markoff, S., The jet model for Sgr A*: Radio and X-ray spectrum, A&A, 362, 113. 2000

Frenk, C. S. & White, S. D. M., The form of the galactic globular cluster system and the distance to the Galactic Centre, MNRAS, 198, 173. 1982

Fritz, T. K., Gillessen, S., Dodds-Eden, K., et al., Line Derived Infrared Extinction toward the Galactic Center, ApJ, 737, 73. 2011

Genzel, R., Eckart, A., Ott, T., & Eisenhauer, F., On the nature of the dark mass in the centre of the Milky Way, MNRAS, 291, 219. 1997

Genzel, R., Eisenhauer, F., & Gillessen, S., The Galactic Center massive black hole and nuclear star cluster, Reviews of Modern Physics, 82, 3121. 2010

Genzel, R., Schödel, R., Ott, T., et al., Near-infrared flares from accreting gas around the supermassive black hole at the Galactic Centre, Nature, 425, 934. 2003

Genzel, R., Thatte, N., Krabbe, A., Kroker, H., & Tacconi-Garman, L. E., The Dark Mass Concentration in the Central Parsec of the Milky Way, ApJ, 472, 153. 1996

Ghez, A. M., Klein, B. L., Morris, M., & Becklin, E. E., High Proper-Motion Stars in the Vicinity of Sagittarius A*: Evidence for a Supermassive Black Hole at the Center of Our Galaxy, ApJ, 509, 678. 1998

Ghez, A. M., Salim, S., Weinberg, N. N., et al., Measuring Distance and Properties of the Milky Way's Central Supermassive Black Hole with Stellar Orbits, ApJ, 689, 1044. 2008

Gillessen, S., Eisenhauer, F., Fritz, T. K., et al., The Orbit of the Star S2 Around SGR A* from Very Large Telescope and Keck Data, ApJL, 707, L114. 2009b

Gillessen, S., Eisenhauer, F., Trippe, S., et al., Monitoring Stellar Orbits Around the Massive Black Hole in the Galactic Center, ApJ, 692, 1075. 2009a

Gillessen, S., Genzel, R., Fritz, T. K., et al., A gas cloud on its way towards the supermassive black hole at the Galactic Centre, Nature, 481, 51. 2012

Gravity Collaboration, Abuter, R., Amorim, A., et al., Detection of the gravitational redshift in the orbit of the star S2 near the Galactic centre massive black hole, A&A, 615, L15. 2018

Güsten, R., Genzel, R., Wright, M. C. H., et al., Aperture synthesis observations of the circumnuclear ring in the Galactic center, ApJ, 318, 124. 1987

Haggard, D., Baganoff, F. K., Rea, N., et al., 2014 Chandra X-ray Monitoring of Sgr A*/G2 and SGR J1745-29, The Astronomer's Telegram, 6242. 2014

Herrnstein, R. M. & Ho, P. T. P., The Nature of the Molecular Environment within 5 Parsecs of the Galactic Center, ApJ, 620, 287. 2005

Herrnstein, R. M., Zhao, J.-H., Bower, G. C., & Goss, W. M., The Variability of Sagittarius A* at Centimeter Wavelengths, AJ, 127, 3399. 2004

Ho, L. C., The Spectral Energy Distributions of Low-Luminosity Active Galactic Nuclei, ApJ, 516, 672. 1999

Jansky, K. G., Electrical phenomena that apparently are of interstellar origin, Popular Astronomy, 41, 548. 1933

Karssen, G. D., Bursa, M., Eckart, A., et al., Bright X-ray flares from Sgr A*, MNRAS, 472, 4422. 2017

Kassim, N. E., Larosa, T. N., Lazio, T. J. W., & Hyman, S. D., in Astronomical Society of the Pacific Conference Series, Vol. 186, The Central Parsecs of the Galaxy, ed. H. Falcke, A. Cotera, W. J. Duschl, F. Melia, & M. J. Rieke, 403. 1999

Kawashima, T., Matsumoto, Y., & Matsumoto, R., A possible time-delayed brightening of the Sgr A* accretion flow after the pericenter passage of the G2 cloud, PASJ, 69, 43. 2017

Kennea, J. A., Burrows, D. N., Kouveliotou, C., et al., Swift Discovery of a New Soft Gamma Repeater, SGR J1745-29, near Sagittarius A*, ApJL, 770, L24. 2013

Li, J., Shen, Z.-Q., Miyazaki, A., et al., The Variability of Sagittarius A* at 3 Millimeter, ApJ, 700, 417. 2009

Liu, S., Petrosian, V., & Melia, F., Electron Acceleration around the Supermassive Black Hole at the Galactic Center, ApJL, 611, L101. 2004

Lo, K. Y. & Claussen, M. J., High-resolution observations of ionized gas in central 3 parsecs of the Galaxy - Possible evidence for infall, Nature, 306, 647. 1983

Loeb, A. & Waxman, E., Properties of the radio-emitting gas around Sgr A*, JCAP, 3, 011. 2007

López-Corredoira, M., Allende Prieto, C., Garzón, F., et al., Disk stars in the Milky Way detected beyond 25 kpc from its center, A&A, 612, L8. 2018

Ma, R.-Y., Roberts, S. R., Li, Y.-P., & Wang, Q. D., Spectral energy distribution of the inner accretion flow around Sgr A* - clue for a weak outflow in the innermost region, MNRAS, 483, 5614. 2019

Macquart, J.-P. & Bower, G. C., Understanding the Radio Variability of Sagittarius A*, ApJ, 641, 302. 2006

Maeda, Y., Baganoff, F. K., Feigelson, E. D., et al., A Chandra Study of Sagittarius A East: A Supernova Remnant Regulating the Activity of Our Galactic Center?, ApJ, 570, 671. 2002

Magain, P., Lecture notes of the course "Extragalactic astrophysics", Université de Liège. 2018

Maitra, D., Markoff, S., & Falcke, H., A time-dependent jet model for the emission from Sagittarius A*, A&A, 508, L13. 2009

Markoff, S., Falcke, H., Yuan, F., & Biermann, P. L., The Nature of the 10 kilosecond X-ray flare in Sgr A*, A&A, 379, L13. 2001

Marrone, D. P., Moran, J. M., Zhao, J.-H., & Rao, R., An Unambiguous Detection of Faraday Rotation in Sagittarius A*, ApJL, 654, L57. 2007

Meyer, L., Ghez, A. M., Schödel, R., et al., The Shortest-Known-Period Star Orbiting Our Galaxy's Supermassive Black Hole, Science, 338, 84. 2012

Meyer, L., Witzel, G., Longstaff, F. A., & Ghez, A. M., A Formal Method for Identifying Distinct States of Variability in Time-varying Sources: Sgr A* as an Example, ApJ, 791, 24. 2014

Mori, K., Gotthelf, E. V., Zhang, S., et al., NuSTAR Discovery of a 3.76 s Transient Magnetar Near Sagittarius A*, ApJL, 770, L23. 2013

Morris, M. & Serabyn, E., The Galactic Center Environment, ARA&A, 34, 645. 1996

Morrison, R. & McCammon, D., Interstellar photoelectric absorption cross sections, 0.03-10 keV, ApJ, 270, 119. 1983

Mościbrodzka, M. & Falcke, H., Coupled jet-disk model for Sagittarius A*: explaining the flat-spectrum radio core with GRMHD simulations of jets, A&A, 559, L3. 2013

Mossoux, E., Multiwavelength Study of the Flaring Activity of the Supermassive Black Hole Sgr A* at the Center of the Milky Way, PhD thesis, Université de Strasbourg. 2016

Mossoux, E. & Eckart, A., The X-ray footprint of the circumnuclear disc, MNRAS, 474, 3787. 2018

Mossoux, E. & Grosso, N., Sixteen years of X-ray monitoring of Sagittarius A*: Evidence for a decay of the faint flaring rate from 2013 August, 13 months before a rise in the bright flaring rate, A&A, 604, A85. 2017

Mossoux, E., Grosso, N., Bushouse, H., et al., Multiwavelength study of the flaring activity of Sagittarius A in 2014 February-April, A&A, 589, A116. 2016

Mossoux, E., Grosso, N., Vincent, F. H., & Porquet, D., Study of the X-ray activity of Sagittarius A* during the 2011 XMM-Newton campaign (Corrigendum), A&A, 580, C2. 2015a

Mossoux, E., Grosso, N., Vincent, F. H., & Porquet, D., Study of the X-ray activity of Sagittarius A*during the 2011 XMM-Newton campaign, A&A, 573, A46. 2015b

Narayan, R., Mahadevan, R., Grindlay, J. E., Popham, R. G., & Gammie, C., Advection-dominated accretion model of Sagittarius A*: evidence for a black hole at the Galactic center., ApJ, 492, 554. 1998

Narayan, R., Yi, I., & Mahadevan, R., Explaining the spectrum of Sagittarius A* with a model of an accreting black hole, Nature, 374, 623. 1995

Nayakshin, S., Cuadra, J., & Sunyaev, R., X-ray flares from Sgr A*: Star-disk interactions?, A&A, 413, 173. 2004

Neilsen, J., Markoff, S., Nowak, M. A., et al., The X-Ray Flux Distribution of Sagittarius A* as Seen by Chandra, ApJ, 799, 199. 2015

Neilsen, J., Nowak, M. A., Gammie, C., et al., A Chandra/HETGS Census of X-Ray Variability from Sgr A* during 2012, ApJ, 774, 42. 2013

Nishiyama, S., Tamura, M., Hatano, H., et al., Near-Infrared Polarimetry of Flares from Sgr A* with Subaru/-CIAO, ApJL, 702, L56. 2009

Nowak, M. A., Neilsen, J., Markoff, S. B., et al., Chandra/HETGS Observations of the Brightest Flare Seen from Sgr A*, ApJ, 759, 95. 2012

Oort, J. H. & Plaut, L., The distance to the galactic centre derived from RR Lyrae variables, the distribution of these variables in the galaxy's inner region and halo, and a rediscussion of the galactic rotation constants, A&A, 41, 71. 1975

Özel, F., Psaltis, D., & Narayan, R., Hybrid Thermal-Nonthermal Synchrotron Emission from Hot Accretion Flows, ApJ, 541, 234. 2000

Paumard, T., Genzel, R., Martins, F., et al., The Two Young Star Disks in the Central Parsec of the Galaxy: Properties, Dynamics, and Formation, ApJ, 643, 1011. 2006

Paumard, T., Maillard, J. P., Morris, M., & Rigaut, F., New results on the helium stars in the galactic center using BEAR spectro-imagery, A&A, 366, 466. 2001

Petrov, L., Kovalev, Y. Y., Fomalont, E. B., & Gordon, D., The Very Long Baseline Array Galactic Plane Survey - VGaPS, AJ, 142, 35. 2011

Ponti, G., De Marco, B., Morris, M. R., et al., Fifteen years of XMM-Newton and Chandra monitoring of Sgr A*: evidence for a recent increase in the bright flaring rate, MNRAS, 454, 1525. 2015

Ponti, G., George, E., Scaringi, S., et al., A powerful flare from Sgr A* confirms the synchrotron nature of the X-ray emission, MNRAS, 468, 2447. 2017

Ponti, G., Jin, C., De Marco, B., et al., Swift J174540.7-290015: a new accreting binary in the Galactic Centre, MNRAS, 461, 2688. 2016

Porquet, D., Grosso, N., Predehl, P., et al., X-ray hiccups from Sagittarius A* observed by XMM-Newton. The second brightest flare and three moderate flares caught in half a day, A&A, 488, 549. 2008

Porquet, D., Predehl, P., Aschenbach, B., et al., XMM-Newton observation of the brightest X-ray flare detected so far from Sgr A*, A&A, 407, L17. 2003

Predehl, P. & Schmitt, J. H. M. M., X-raying the interstellar medium: ROSAT observations of dust scattering halos., A&A, 293, 889. 1995

Rauw, G., Lecture notes of the course "High-energy astrophysics", Université de Liège. 2017

Reid, M. J., The distance to the center of the Galaxy, ARA&A, 31, 345. 1993

Reid, M. J. & Brunthaler, A., The Proper Motion of Sagittarius A*. II. The Mass of Sagittarius A*, ApJ, 616, 872. 2004

Reid, M. J., Readhead, A. C. S., Vermeulen, R. C., & Treuhaft, R. N., The Proper Motion of Sagittarius A*. I. First VLBA Results, ApJ, 524, 816. 1999

Ressler, S. M., Quataert, E., & Stone, J. M., Hydrodynamic simulations of the inner accretion flow of Sagittarius A* fuelled by stellar winds, MNRAS, 478, 3544. 2018

Ressler, S. M., Tchekhovskoy, A., Quataert, E., & Gammie, C. F., The disc-jet symbiosis emerges: modelling the emission of Sagittarius A* with electron thermodynamics, MNRAS, 467, 3604. 2017

Reynolds, M., Kennea, J., Degenaar, N., Wijnands, R., & Miller, J., New Galactic Center X-ray Transient Detected by Swift: SWIFT J174540.7-290015, The Astronomer's Telegram, 8649. 2016

Rieke, G. H., Rieke, M. J., & Paul, A. E., Origin of the excitation of the galactic center, ApJ, 336, 752. 1989

Roberts, S. R., Jiang, Y.-F., Wang, Q. D., & Ostriker, J. P., Towards self-consistent modelling of the Sgr A* accretion flow: linking theory and observation, MNRAS, 466, 1477. 2017

Russeil, D., Star-forming complexes and the spiral structure of our Galaxy, A&A, 397, 133. 2003

Rybicki, G. & Lightman, A. 1979, Radiative Processes in Astrophysics, ed. N. Y. J. Wiley & sons [1979]

Sabha, N., Witzel, G., Eckart, A., et al., The extreme luminosity states of Sagittarius A*, A&A, 512, A2. 2010

Scargle, J. D., Studies in Astronomical Time Series Analysis. V. Bayesian Blocks, a New Method to Analyze Structure in Photon Counting Data, ApJ, 504, 405. 1998

Scargle, J. D., Norris, J. P., Jackson, B., & Chiang, J., Studies in Astronomical Time Series Analysis. VI. Bayesian Block Representations, ApJ, 764, 167. 2013

Schwarzschild, K., Über das Gravitationsfeld eines Massenpunktes nach der Einsteinschen Theorie, Sitzungsberichte der Königlich Preußischen Akademie der Wissenschaften (Berlin), 1916, Seite 189-196. 1916

Serabyn, E., Carlstrom, J., Lay, O., et al., High-Frequency Measurements of the Spectrum of Sagittarius A*, ApJL, 490, L77. 1997

Shahzamanian, B., Eckart, A., Valencia-S., M., et al., Polarized light from Sagittarius A* in the near-infrared K_s-band, A&A, 576, A20. 2015

Shapley, H., Studies Based on the Colors and Magnitudes in Stellar Clusters. VII. The Distances, Distribution in Space, and Dimensions of 69 Globular Clusters., ApJ, 48. 1918

Shcherbakov, R. V. & Baganoff, F. K., Inflow-Outflow Model with Conduction and Self-consistent Feeding for Sgr A*, ApJ, 716, 504. 2010

Swift Science Center, The Swift Technical Handbook, Version 14.0. 2017

Tagger, M. & Melia, F., A Possible Rossby Wave Instability Origin for the Flares in Sagittarius A*, ApJL, 636, L33. 2006

Trap, G., Goldwurm, A., Dodds-Eden, K., et al., Concurrent X-ray, near-infrared, sub-millimeter, and GeV gamma-ray observations of Sagittarius A*, A&A, 528, A140. 2011

Trippe, S., Paumard, T., Ott, T., et al., A polarized infrared flare from Sagittarius A* and the signatures of orbiting plasma hotspots, MNRAS, 375, 764. 2007

Trumpler, R. J., Absorption of Light in the Galactic System, PASP, 42, 214. 1930

Valencia-S., M., Eckart, A., Zajaček, M., et al., Monitoring the Dusty S-cluster Object (DSO/G2) on its Orbit toward the Galactic Center Black Hole, ApJ, 800, 125. 2015

van de Weygaert, R. & Schaap, W., in Lecture Notes in Physics, Berlin Springer Verlag, Vol. 665, Data Analysis in Cosmology, ed. V. J. Martínez, E. Saar, E. Martínez-González, & M.-J. Pons-Bordería, 291–413. 2009

van der Laan, H., A Model for Variable Extragalactic Radio Sources, Nature, 211, 1131. 1966

Verner, D. A., Ferland, G. J., Korista, K. T., & Yakovlev, D. G., Atomic Data for Astrophysics. II. New Analytic FITS for Photoionization Cross Sections of Atoms and Ions, ApJ, 465, 487. 1996

Wilms, J., Allen, A., & McCray, R., On the Absorption of X-Rays in the Interstellar Medium, ApJ, 542, 914. 2000

Witzel, G., Eckart, A., Bremer, M., et al., Source-intrinsic Near-infrared Properties of Sgr A*: Total Intensity Measurements, ApJS, 203, 18. 2012

Witzel, G., Ghez, A. M., Morris, M. R., et al., Detection of Galactic Center Source G2 at 3.8 μm during Periapse Passage, ApJL, 796, L8. 2014b

Witzel, G., Morris, M., Ghez, A., et al., in IAU Symposium, Vol. 303, The Galactic Center: Feeding and Feedback in a Normal Galactic Nucleus, ed. L. O. Sjouwerman, C. C. Lang, & J. Ott, 274–282. 2014a

Yuan, F., Quataert, E., & Narayan, R., Nonthermal Electrons in Radiatively Inefficient Accretion Flow Models of Sagittarius A*, ApJ, 598, 301. 2003

Yuan, Q., Wang, Q. D., Liu, S., & Wu, K., A systematic Chandra study of Sgr A*: II. X-ray flare statistics, MNRAS, 473, 306. 2018

Yusef-Zadeh, F., Bushouse, H., Dowell, C. D., et al., A Multiwavelength Study of Sgr A*: The Role of Near-IR Flares in Production of X-Ray, Soft γ-Ray, and Submillimeter Emission, ApJ, 644, 198. 2006

Yusef-Zadeh, F., Hewitt, J. W., & Cotton, W., A 20 Centimeter Survey of the Galactic Center Region. I. Detection of Numerous Linear Filaments, ApJS, 155, 421. 2004

Yusef-Zadeh, F. & Königl, A., in Astronomical Society of the Pacific Conference Series, Vol. 322, The Formation and Evolution of Massive Young Star Clusters, ed. H. J. G. L. M. Lamers, L. J. Smith, & A. Nota, 201. 2004

Yusef-Zadeh, F., Morris, M., & Chance, D., Large, highly organized radio structures near the galactic centre, Nature, 310, 557. 1984

Yusef-Zadeh, F. & Wardle, M., The Underluminous Nature of Sgr A*, X-ray Astronomy 2009; Present Status, Multi-Wavelength Approach and Future Perspectives, 1248, 233. 2010

Zhang, S., Baganoff, F. K., Ponti, G., et al., Sagittarius A* High-energy X-Ray Flare Properties during NuSTAR Monitoring of the Galactic Center from 2012 to 2015, ApJ, 843, 96. 2017

Zubovas, K., Nayakshin, S., & Markoff, S., Sgr A* flares: tidal disruption of asteroids and planets?, MNRAS, 421, 1315. 2012

Appendix A

Light curves of XMM-Newton and Chandra observations

This appendix shows the light curves obtained from observations with XMM-Newton and Chandra during the years 2016-2018.

On each observation, the Bayesian Blocks algorithm (Section 4.1) has been applied to detect flares from Sgr A*. Because of the contamination of a very bright transient close to the target, it has not been possible to see any flare in the observation from XMM-Newton (Figure A.1). However, 9 flares have been detected in the observations of Chandra (Figures A.2 and A.3, details in Section 4.1.4).

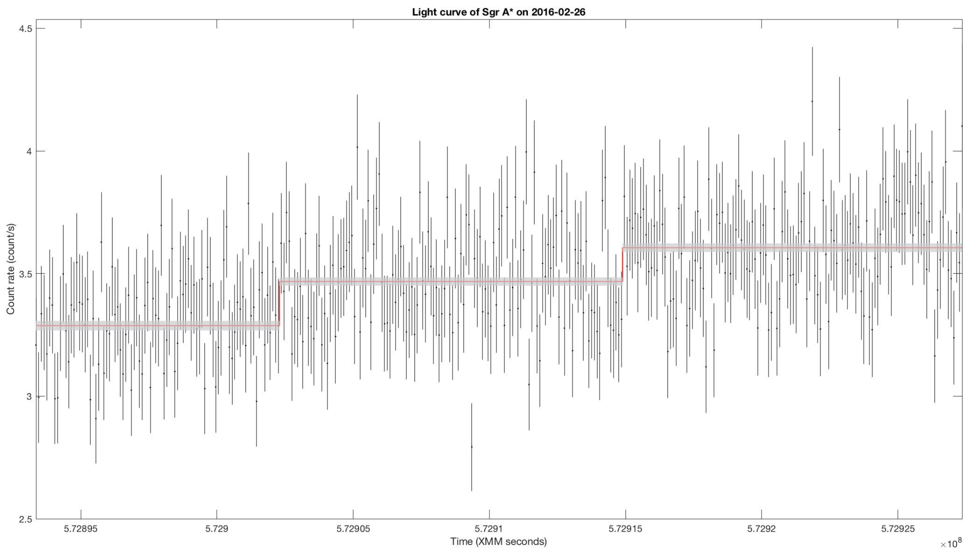

Figure A.1: Light curve of the XMM-Newton observation got with EPIC/pn instrument on 2016 February 26. The red lines corresponds to the Bayesian Blocks with the grey boxes representing the uncertainties on these blocks.

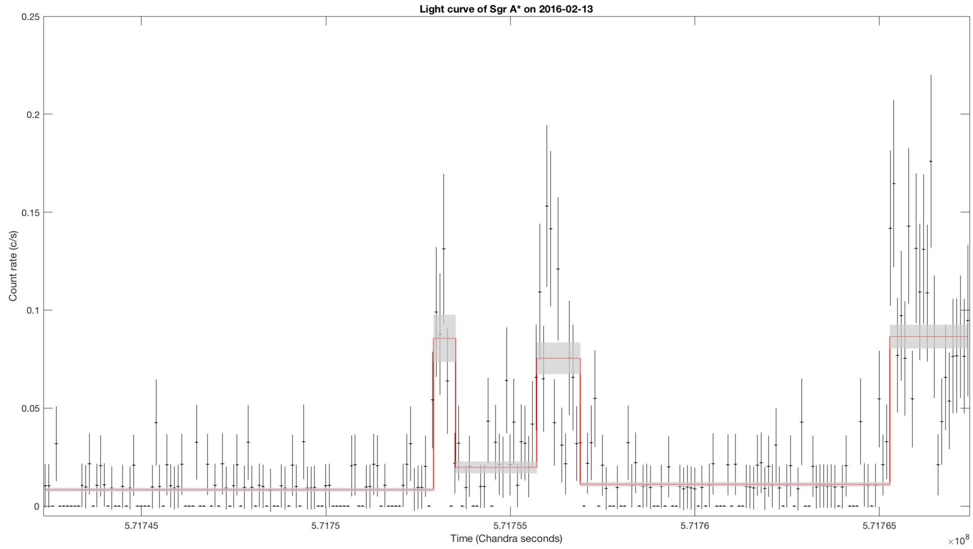

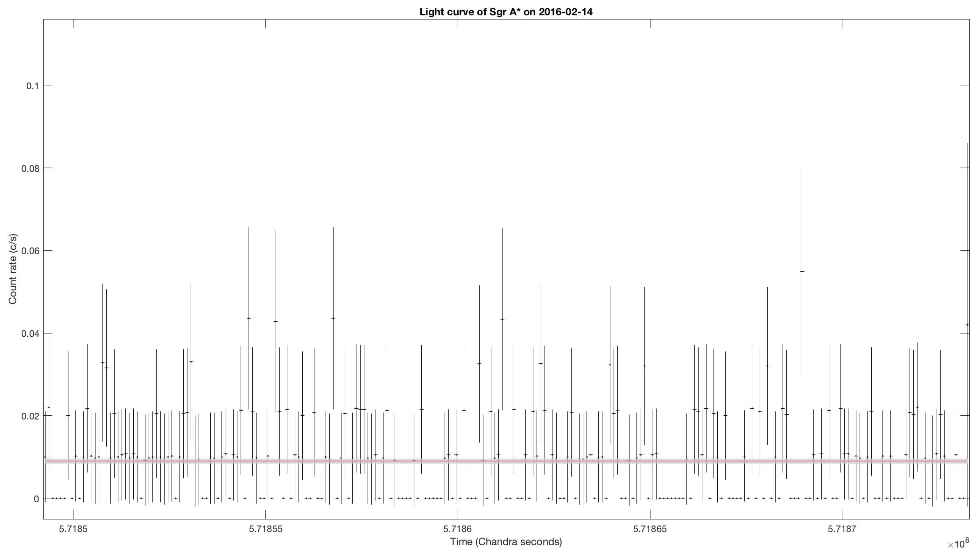

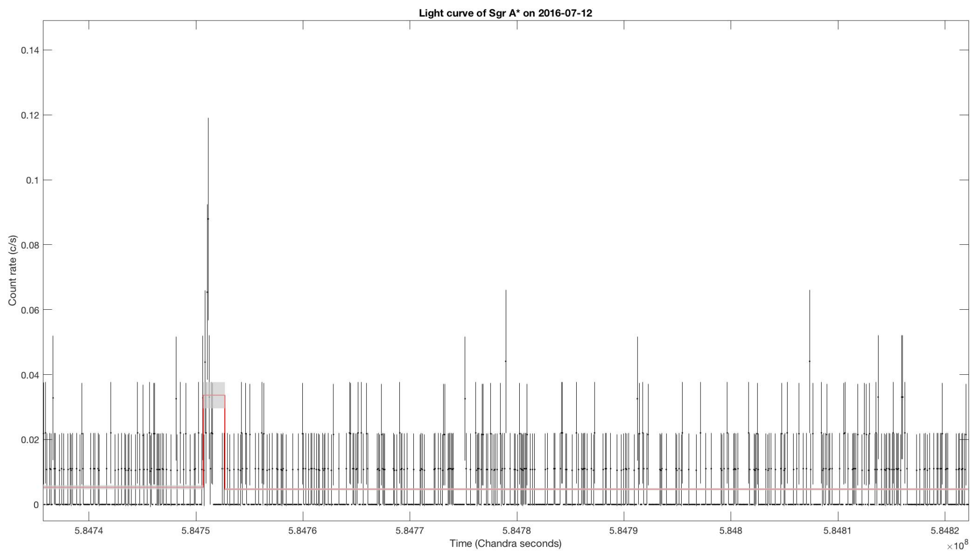

Figure A.2: Light curves of Chandra observations in 2016. The red lines corresponds to the Bayesian blocks. The grey boxes are the uncertainties on the value of the count rate of the Bayesian blocks.

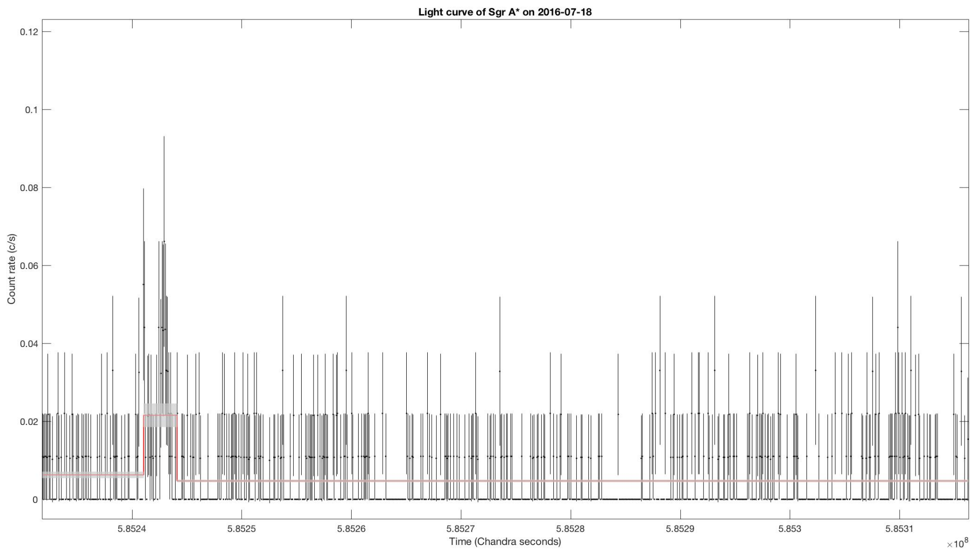

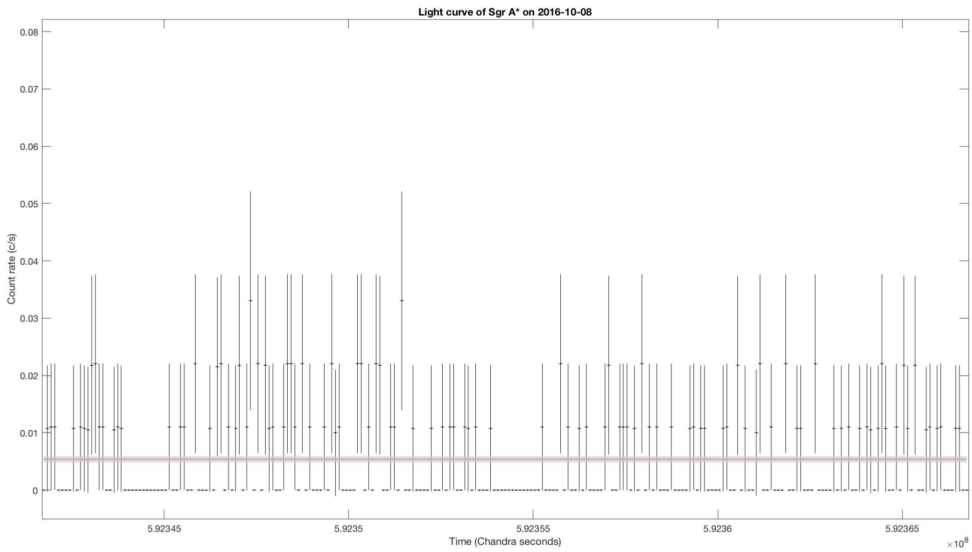

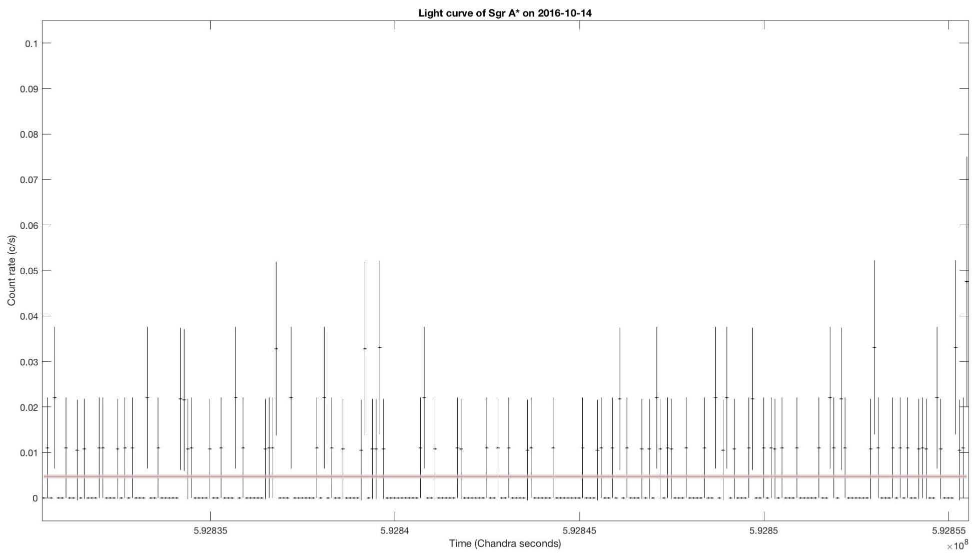

Figure A.2: Continued

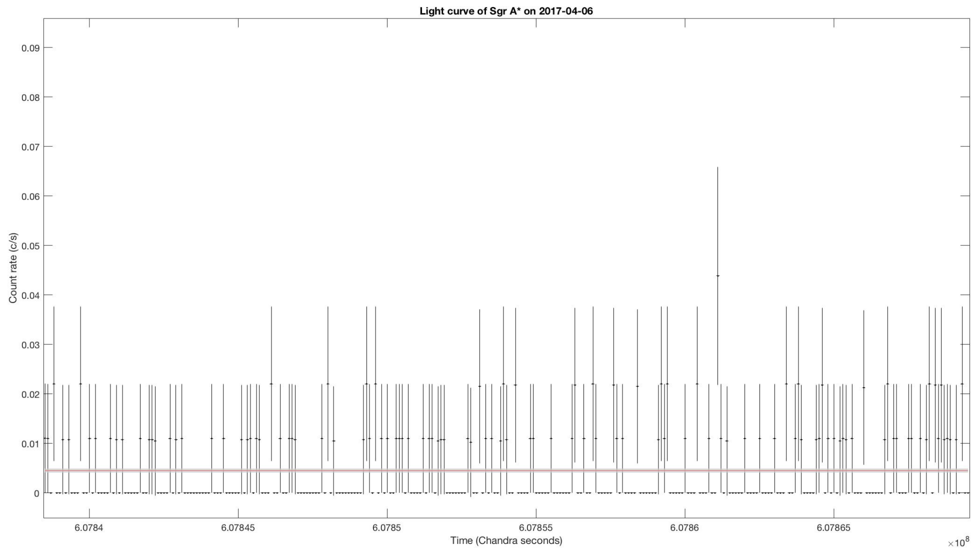

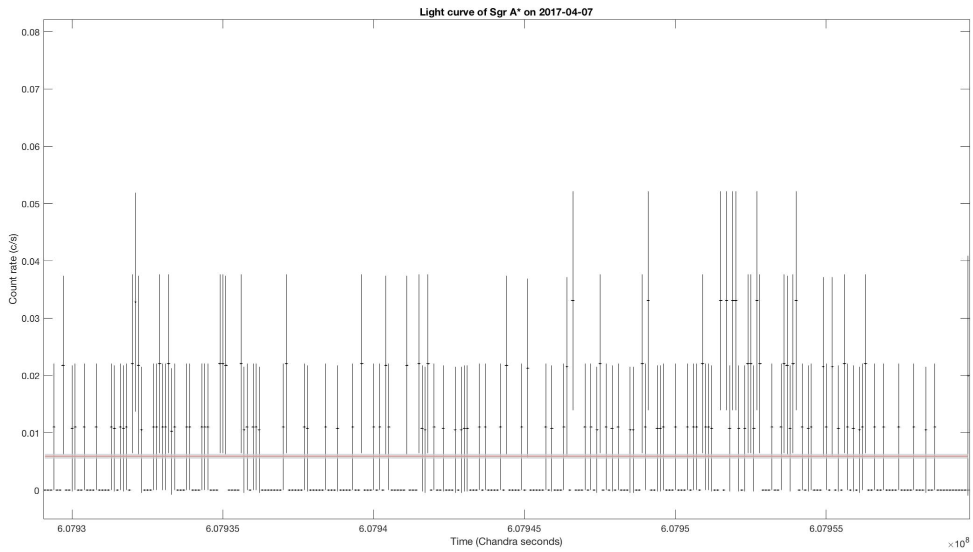

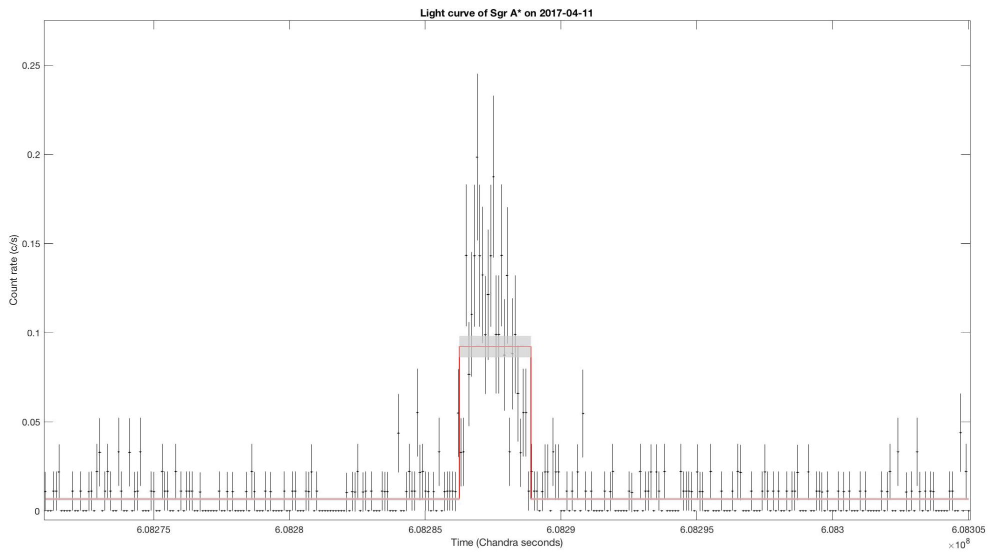

Figure A.3: Light curves of Chandra observations in 2017. The red lines corresponds to the Bayesian blocks. The grey boxes are the uncertainties on the value of the count rate of the Bayesian blocks.

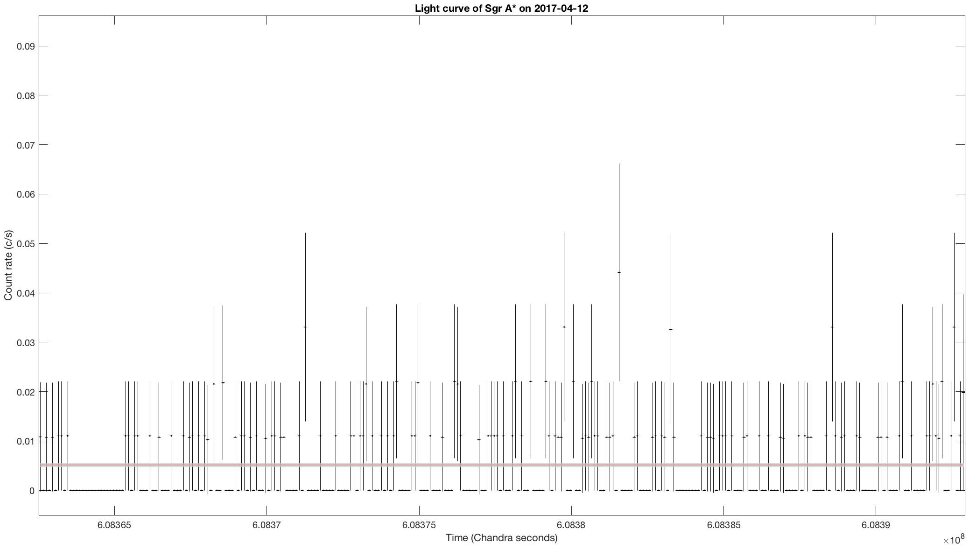

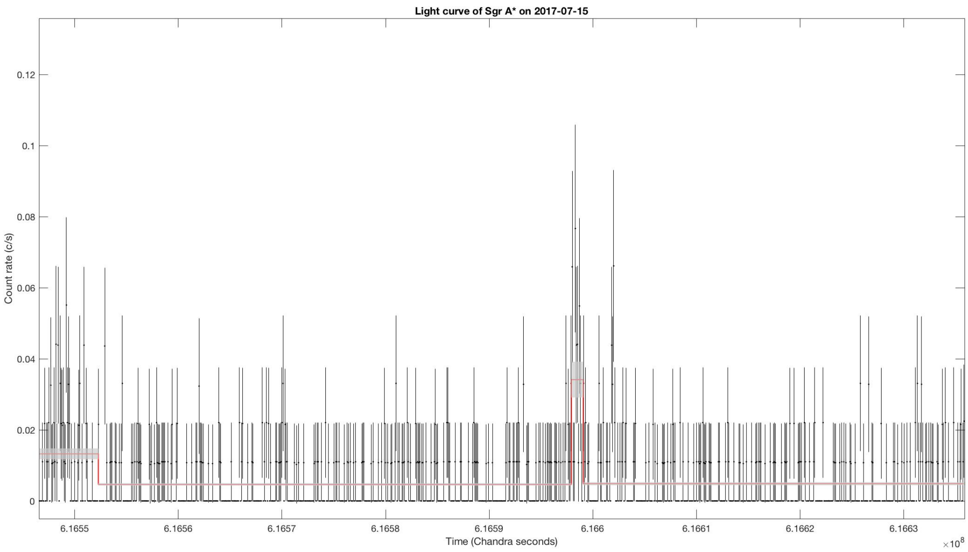

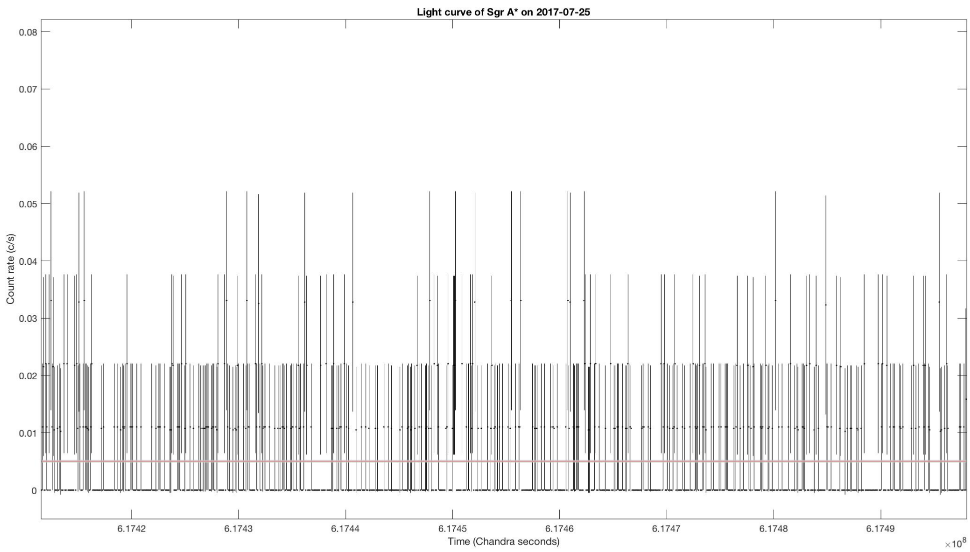

Figure A.3: Continued

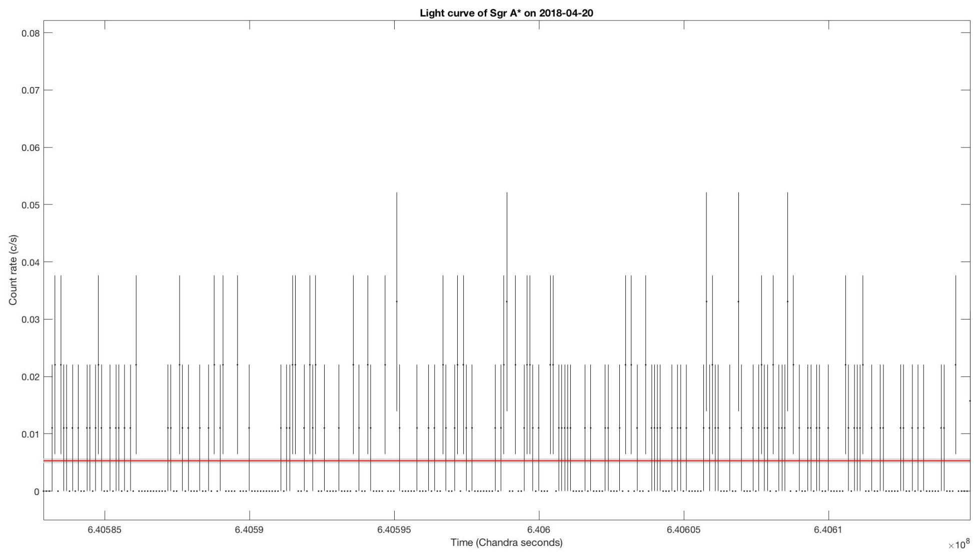

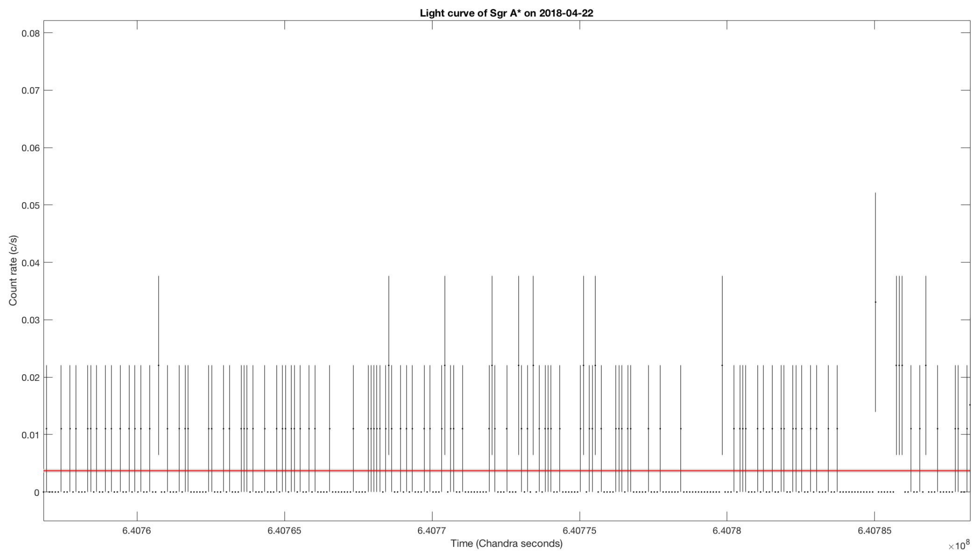

Figure A.4: Light curves of Chandra observations in 2018. The red lines corresponds to the Bayesian blocks. The grey boxes are the uncertainties on the value of the count rate of the Bayesian blocks.

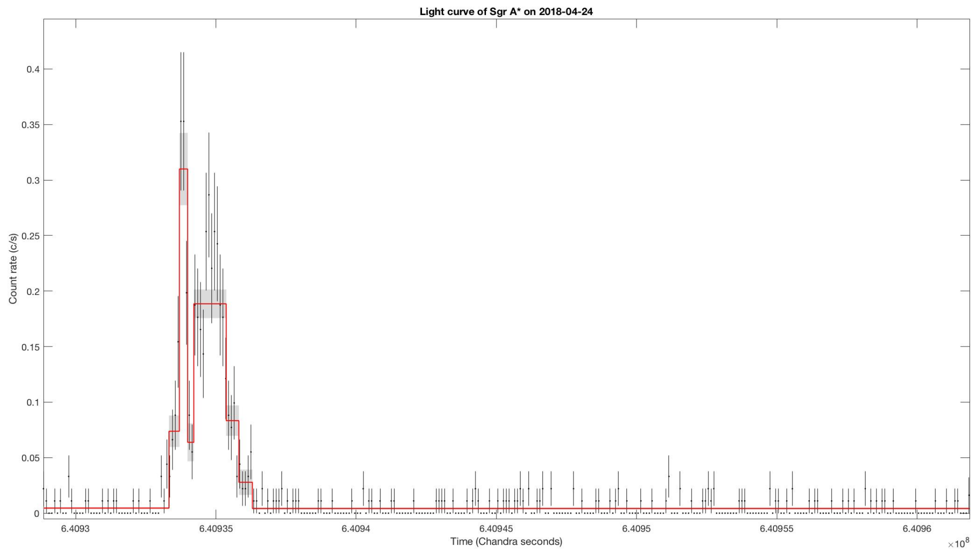

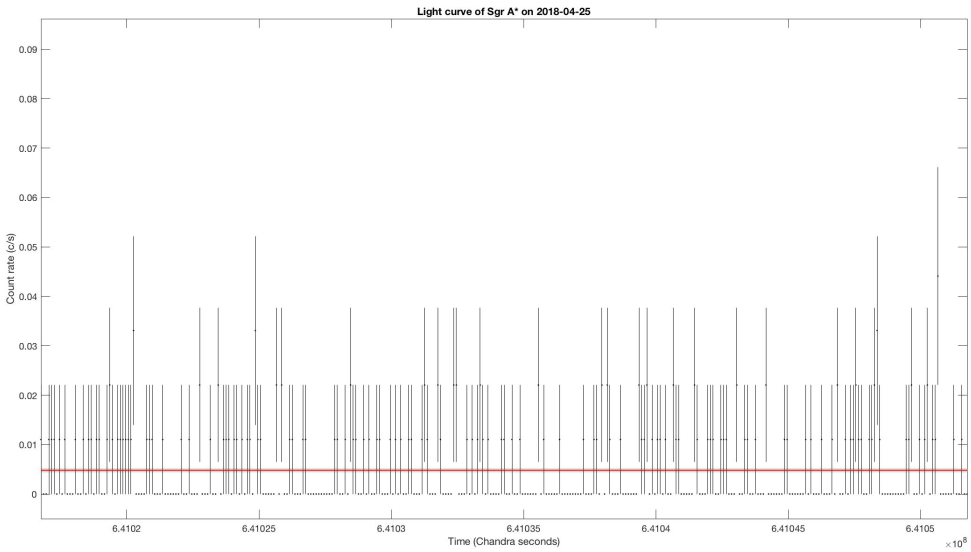

Figure A.4: Continued

Appendix B

The Degenaar's method with the median

In a first attempt, I adapted the Degenaar et al.'s method by using the median annual count rate with its associated standard deviation instead of the mean, because the median is less sensitive to extreme values. However, several factors indicated that this choice was not relevant once applied on the data of 2017 and 2018. The first one is that the use of the median led to a too large number of detected flares (8 in 2017, 7 in 2018) compared to previous studies that indicates up to three flares in a year (Degenaar et al. 2013,2015; Mossoux & Grosso 2017).

On 2017 April 07 Swift and Chandra observed the Galactic Centre at the same time. The observation of Swift is much shorter and is superimposed on the one of Chandra only at the end where a small, but not significant, increase of flux appears (between 10:58 (UTC) and 12:22 (UTC)). With the median, the Swift observation was considered as a flare while no flare has been detected with the Bayesian blocks applied on Chandra's observation. As mentioned in Chapter 3, the correction factor applied on the Swift count rates must be close to 2.3 for an observation to be "valid". If the correction factor is too large, this means that Sgr A* is too close from a bad pixel or a CCD edge and the observation is not usable or the count rate is not relevant. I thus checked the correction factor on 2017 April 07, which was equal to 2.2. This factor thus did not explain why one telescope observed a flare and not the other.

On the image of Chandra at that date, one can distinguish a single very bright pixel close to the projected location of Sgr A* not present in other observations. This pixel is encircled by the extraction region for Swift but not for Chandra. One hypothesis could be that a source on this pixel was varying and would be responsible of the high count rate of the Swift observation. I thus extracted the events from a $1''.25$-radius circle centred on this pixel in the Chandra observation to see if an increase of flux appears at the end of the observation, which could explain the detection of the flare with Swift and the very small increase of flux in the light curve of Chandra. By viewing the light curve of the bright pixel, no significant increase appears at the end of the observation (Figure B.1). Thus this hypothesis does not seem sufficient to explain the difference in the detection of flare.

I decided to focus only on April 2017. During that period, Swift observed more regularly the Galactic Centre and more data were provided. Thus, it would be interesting to analyse just that time interval. In particular, one idea is that the dispersion could be higher at that time, and if it is the case the flare could actually not be detected with Swift. By checking the presence of flares during that period, the two flares are still detected. The problem of detection was thus not solved and I concluded that the median method tested here is not reliable.

Because of all these factors, I decided to keep only the results obtained with the pure Degenaar et al.'s method based on the evaluation of the mean count rate during a yearly campaign.

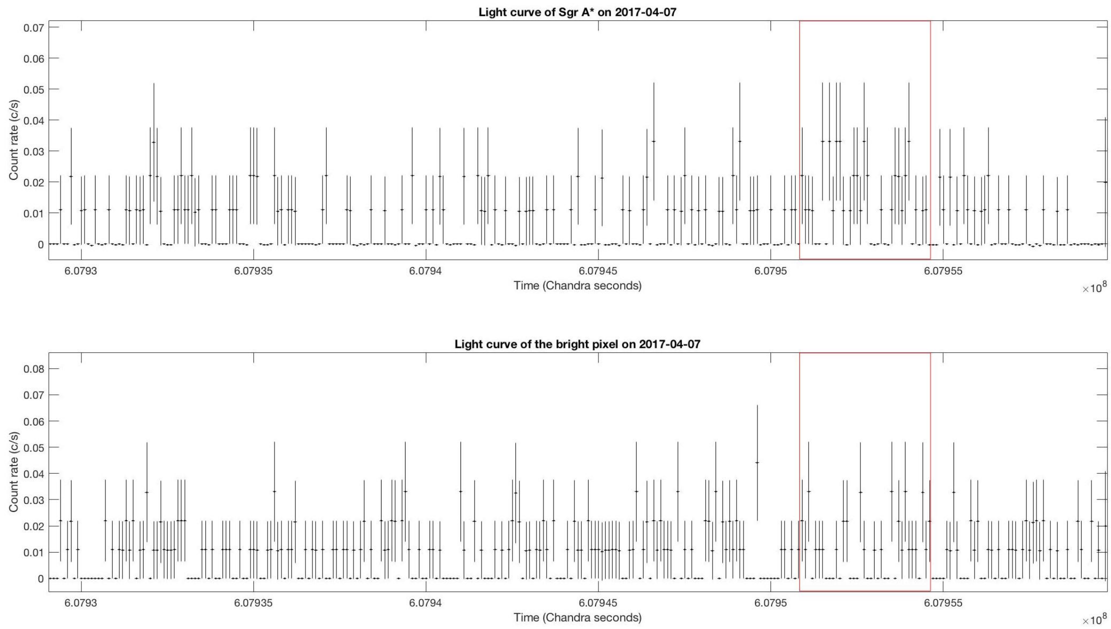

Figure B.1: Comparison between the Chandra light curve of Sgr A* (*top panel*) and the one of the very bright pixel (*bottom panel*) on 2017 April 07. The red boxes correspond to the time interval of interest during which Swift observed Sgr A*. No significant increase of flux from the pixel appears at that time.

Appendix C

Recap charts

This appendix shows the recap chart about the average flare detection efficiency for the different non-flaring levels observed from 1999 with the three telescopes as well as recap charts of all the observations done during the period 2016-2018.

Table C.1: Average flare detection efficiency associated with the different non-flaring levels observed by Chandra, XMM-Newton and Swift

Telescope	Non-flaring level (count s^{-1})	Observing dates[a]	Total exposure[b] (ks)	η[c] (%)
Chandra	0.0046	2016-07-12 - 2016-07-18 and 2016-10-14 and 2017-04-06 and 2017-07-15 and 2018-04-22 - 2018-04-25	378.2	51.0
————	0.005	1999-09-21 - 2011-07-30 and 2015-04-25 and 2017-04-12 and 2017-07-25	1746	71.9
————	0.0054	2016-10-08 and 2018-04-20	51.8	49.5
————	0.0059	2017-04-07	27.8	49.7
————	0.0064	2012-02-06 - 2012-10-31 and 2017-04-11	3137	49.6
————	0.0073	2014-03-14 - 2015-05-14	476.6	48.8
————	0.0083	2016-02-13	22.7	45.0
————	0.009	2013-05-25 and 2013-06-04 – 2013-06-09 and 2013-07-02 and 2013-08-31 – 2013-09-14 and 2013-10-04 – 2014-02-22 and 2016-02-14	237.8	46.6
————	0.014	2013-07-27 – 2013-08-12 and 2013-09-20	119.6	41.6
————	0.0236	2013-05-12	15.1	49.0
————	0.045	2013-04-06 - 2013-04-14	56.4	43.2
XMM-Newton	0.1	2000-09-17 - 2002-10-03 and 2006-02-27 - 2012-08-31	1058	34.7
————	0.170	2004-03-28 - 2004-09-03 and 2014-08-30 - 2015-04-02	633.1	29.7
————	0.287	2014-04-02	54.9	23.8
————	0.294	2014-04-03	83.5	23.5
————	0.312	2014-03-10	54.0	23.2
————	0.320	2014-02-28	51.9	22.8
————	0.506	2013-09-22	39.4	19.8
————	0.535	2013-08-30 - 2013-09-10	91.3	19.7
————	3.5	2016-02-26	37.0	0.002
Swift	0.019	2006 and 2012	335.7	47.2
————	0.028	2007 - 2011 and 2015 and 2016 (after August 01) and 2017 - 2018	1397	30.2
————	0.044	2013 (September-October) and 2016 (before August)	335.7	39.5
————	0.056	2014	231.4	37.6
————	0.11	2013 (July-August)	60.1	27.0
————	0.15	2013 (June)	62.3	28.6
————	0.21	2013 (May) and 2016 (before August)	47.6	26.1
————	0.29	2013 (April-May) and 2016 (before August)	37.2	23.4
————	0.74	2016 (before August)	36.5	17.5

Notes: [(a)] In the case of Swift, the average flare detection efficiency in 2013 and 2016 is computed for different non-flaring levels due to the activity of the magnetar or X-ray transients; [(b)] Sum of the GTIs of the corresponding observations; [(c)] The average flare detection efficiency above the corresponding non-flaring level.

Table C.2: Recap chart of the observations from 2016 to 2018 with Chandra

Observations								Flares					
												Mean	
ObsID	PI	Start (UT)	End (UT)	Exposure (ks)	Instrument	Non-flaring level (count s^{-1})	η_{obs} [a] (%)	#	Start (UT)	End (UT)	Duration (s)	Count rate [b] (count s^{-1})	Flux [c] (10^{-12} erg s^{-1} cm^{-2})
18055	Garmire	2016-02-13 08:59:23	2016-02-13 16:26:00	22.7	ACIS-S	0.0083 ± 0.0009	45	1	2016-02-13 12:14:10	2016-02-13 12:24:07	597	0.078 ± 0.012	11.6 ± 1.80
——	——	——	——	——	——	——	——	2	2016-02-13 13:00:45	2016-02-13 13:20:23	1178	0.067 ± 0.008	9.92 ± 1.18
——	——	——	——	——	——	——	——	3	2016-02-13 15:40:17	>2016-02-13 16:15:46	>2129	0.078 ± 0.006	11.6 ± 0.89
18056	Garmire	2016-02-14 14:46:01	2016-02-14 21:44:19	21.8	ACIS-S	0.0090 ± 0.0006	46.6		....	....	....	......	....
18731	Baganoff	2016-07-12 18:23:59	2016-07-13 18:42:51	78.4	ACIS-S	0.0047 ± 0.0003	51	4	2016-07-12 22:43:30	2016-07-12 23:17:06	2076	0.029 ± 0.004	4.29 ± 0.59
18732	Baganoff	2016-07-18 12:01:38	2016-07-19 12:09:00	76.6	ACIS-S	0.0047 ± 0.0003	51	5	2016-07-18 14:56:24	2016-07-18 15:47:03	3039	0.017 ± 0.003	2.52 ± 0.44
18057	Garmire	2016-10-08 19:07:12	2016-10-09 02:38:59	22.7	ACIS-S	0.0054 ± 0.0005	49.5		....	....	....	......	....
18058	Garmire	2016-10-14 10:47:43	2016-10-14 18:16:44	22.7	ACIS-S	0.0047 ± 0.0004	51		....	....	....	......	....
19726	Garmire	2017-04-06 03:47:13	2017-04-06 12:51:35	28.2	ACIS-S	0.0045 ± 0.0004	51		....	....	....	......	....
19727	Garmire	2017-04-07 04:57:18	2017-04-07 13:53:40	27.8	ACIS-S	0.0059 ± 0.0004	49.7		....	....	....	......	....
20041	Garmire	2017-04-11 03:51:22	2017-04-11 13:56:48	30.9	ACIS-S	0.0066 ± 0.0006	49.6	6	2017-04-11 08:23:04	2017-04-11 09:56:59	2635	0.085 ± 0.006	12.6 ± 0.89
20040	Garmire	2017-04-12 05:18:22	2017-04-12 14:15:52	27.5	ACIS-S	0.0051 ± 0.0004	71.9		....	....	....	......	....
19703	Baganoff	2017-07-15 22:36:07	2017-07-17 00:01:34	81.0	ACIS-S	0.0046 ± 0.0003	51	7	<2017-07-15 22:54:42	2017-07-16 00:30:18	>5736	0.008 ± 0.002	1.18 ± 0.22
——	——	——	——	——	——	——	——	8	2017-07-16 13:10:52	2017-07-16 13:29:56	1144	0.029 ± 0.005	4.29 ± 0.74
19704	Baganoff	2017-07-25 22:57:27	2017-07-26 23:28:30	78.4	ACIS-S	0.0050 ± 0.0002	71.9		....	....	....	......	....
20344	Neilsen	2018-04-20 03:17:44	2018-04-20 12:59:33	29.1	ACIS-S	0.0053 ± 0.0004	49.5		....	....	....	......	....
20345	Neilsen	2018-04-22 03:31:16	2018-04-22 12:57:15	28.5	ACIS-S	0.0037 ± 0.0003	51		....	....	....	......	....
20346	Neilsen	2018-04-24 03:33:43	2018-04-24 13:21:29	29.0	ACIS-S	0.0042 ± 0.0004	51	9	2018-04-24 05:00:57	2018-04-24 05:42:27	2490	0.124 ± 0.006	18.4 ± 0.89
20347	Neilsen	2018-04-25 03:37:23	2018-04-25 14:13:22	32.8	ACIS-S	0.0048 ± 0.0004	51		....	....	....	......	....

Notes: $^{(a)}$ Average flare detection efficiency above the corresponding non-flaring level (see Table C.1); $^{(b)}$ The given mean count rate during the flare has been obtained after subtraction of the non-flaring level; $^{(c)}$ Mean unabsorbed flux obtained after conversion of the mean count rate with the factor 148.1×10^{-12} erg s^{-1} cm^{-2} / count s^{-1} corresponding to the ACIS-S instrument.

Table C.3: Recap chart of the observations from 2016 to 2018 with XMM-Newton

Observations								Flares					
												Mean	
ObsID	PI	Start (UT)	End (UT)	Exposure (ks)	Instrument	Non-flaring level (count s^{-1})	η_{obs} [a] (%)	#	Start (UT)	End (UT)	Duration (s)	Count rate (count s^{-1})	Flux (10^{-12} erg s^{-1} cm^{-2})
0790180401	Schartel	2016-02-26 16:20:13	2016-02-27 02:36:53	37.0	EPIC/pn [b]	3.5 ± 0.02	0.002		..	..	....	.....	....

Notes: $^{(a)}$ Average flare detection efficiency above the corresponding non-flaring level (see Table C.1); $^{(b)}$ The central CCD of the two MOS instruments (on which would be Sgr A*) was deactivated because of the timing mode.

Table C.4: Recap chart of the observations from 2016 to 2018 with Swift

Observations							Flares					
											Mean	
First (UT)	Last (UT)	Number	Total exposure (ks)	Non-flaring level [a] (count s^{-1})	η_{obs} [b] (%)	#	Start [c] (UT)	End [c] (UT)	Duration [c] (s)	Count rate [d] (count s^{-1})	Flux [e] (10^{-12} erg s^{-1} cm^{-2})
2016-02-06 20:58:58	2016-07-30 13:11:57	153	142.6	0.377 ± 0.089	23.4	1	2016-03-24 19:29:41	2016-03-24 19:43:54	853	0.483 ± 0.094	141.8 ± 27.6
——	——	——	——	0.238 ± 0.065	26.1	2	2016-05-05 00:36:01	2016-05-05 00:43:53	472	0.300 ± 0.073	88.1 ± 21.4
——	——	——	——	0.061 ± 0.024	26.1	3	2016-05-19 10:23:39	2016-05-19 10:39:40	961	0.116 ± 0.0.028	34.1 ± 8.2
——	——	——	——	0.068 ± 0.015	26.1	4	2016-05-30 09:42:54	2016-05-30 09:58:54	960	0.080 ± 0.0.019	23.5 ± 5.6
2016-08-01 17:31:57	2016-11-01 07:06:58	78	75.4	0.028 ± 0.0001	30.2		....	....	....	....	....
2017-02-02 23:31:57	2017-11-02 00:26:57	291	248.5	0.026 ± 0.0003	30.2	5	2017-06-12 15:59:41	2017-06-12 16:20:52	1271	0.096 ± 0.010	28.2 ± 2.94
2018-02-02 17:58:56	2018-11-02 04:27:57	233	222.7	0.025 ± 0.0003	30.2	6	2018-02-17 00:45:29	2018-02-17 01:01:52	983	0.069 ± 0.010	20.2 ± 2.94
——	——	——	——	——	——	7	2018-08-22 19:17:33	2018-08-22 19:29:53	740	0.083 ± 0.012	24.4 ± 3.52

Notes: $^{(a)}$ In the first part of 2016, it was impossible to determine an unique non-flaring level because of the activity of X-ray transients. Are shown only the non-flaring level associated with the four flares, computed as the mean count-rate produced by the transients; $^{(b)}$ Average flare detection efficiency above the corresponding non-flaring level (see Table C.1); $^{(c)}$ The dates and durations correspond to the one of the observation since the flare duration is generally longer; $^{(d)}$ The given mean count rate during the flare has been obtained after subtraction of the non-flaring level; $^{(e)}$ Mean unabsorbed flux obtained after conversion of the mean count rate with the factor 293.5×10^{-12} erg s^{-1} cm^{-2} / count s^{-1} corresponding to the XRT instrument.

Appendix D

Spectra of the 9 Chandra flares

This appendix shows the spectra obtained for the nine flares detected with Chandra during 2016-2018. Each fit has been done with the software XSPEC, using the Cash statistic. Only the flux was fitted and I fixed the hydrogen colum $N_H = 14.3 \times 10^{22} \mathrm{cm}^{-2}$ and the photon index $\Gamma = 2$ as in Mossoux & Grosso (2017). I adjusted the minimum number of counts per bin depending on the considered spectrum for more visual clarity:

Table D.1: Minimum number of counts per bin for the different flares

Flare 1	2 counts per bin
Flare 2	3 counts per bin
Flare 3	4 counts per bin
Flare 4	4 counts per bin
Flare 5	4 counts per bin
Flare 6	3 counts per bin
Flare 7	8 counts per bin
Flare 8	3 counts per bin
Flare 9	2 counts per bin

Notes: The flare number refers to the one in Table C.2.

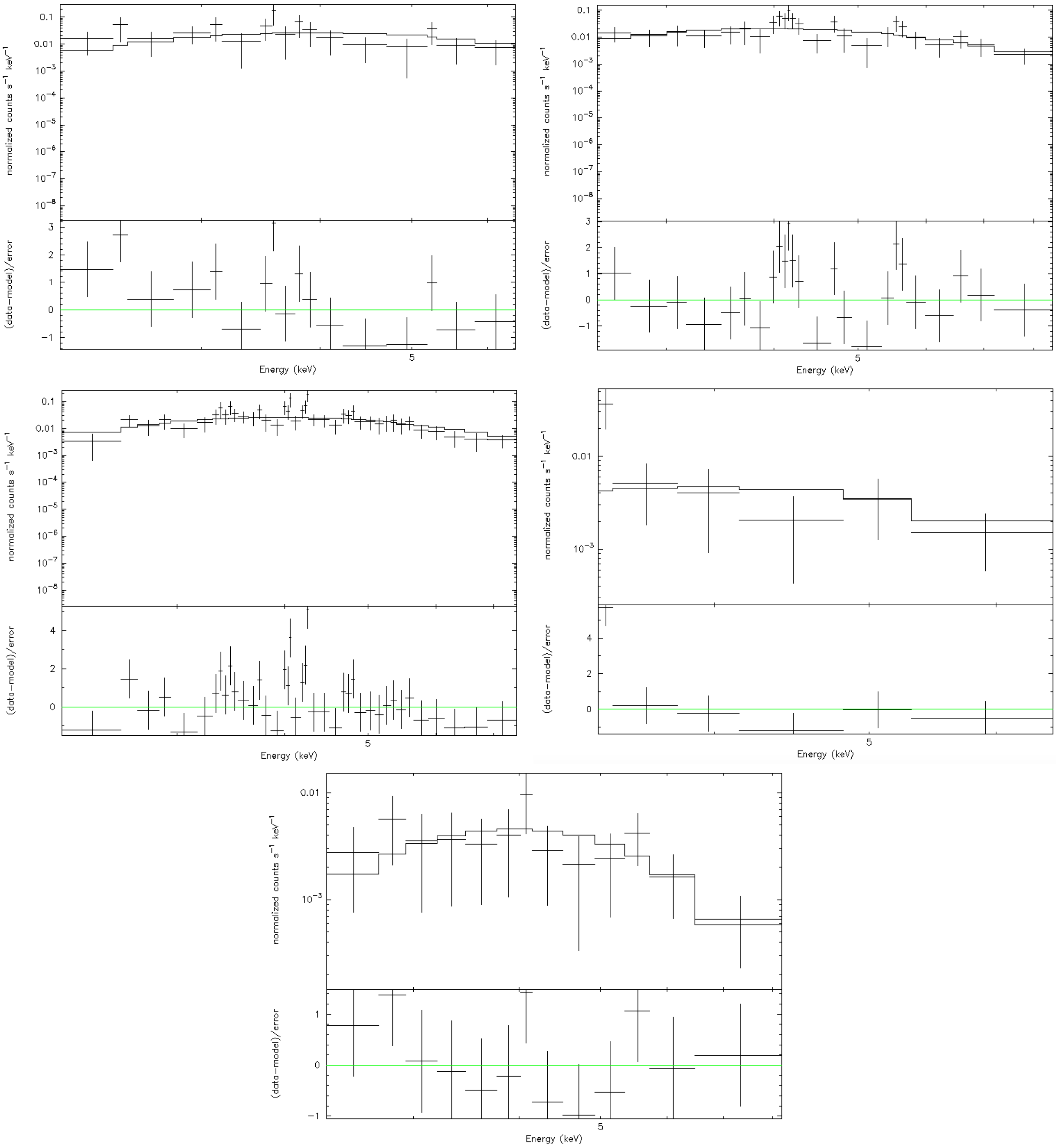

Figure D.1: Chandra spectra in 2016. They are shown by order of flare arrival from the left to the right and from the top to the bottom. The bottom part of each panel represents the residuals between the fit and the observational data.

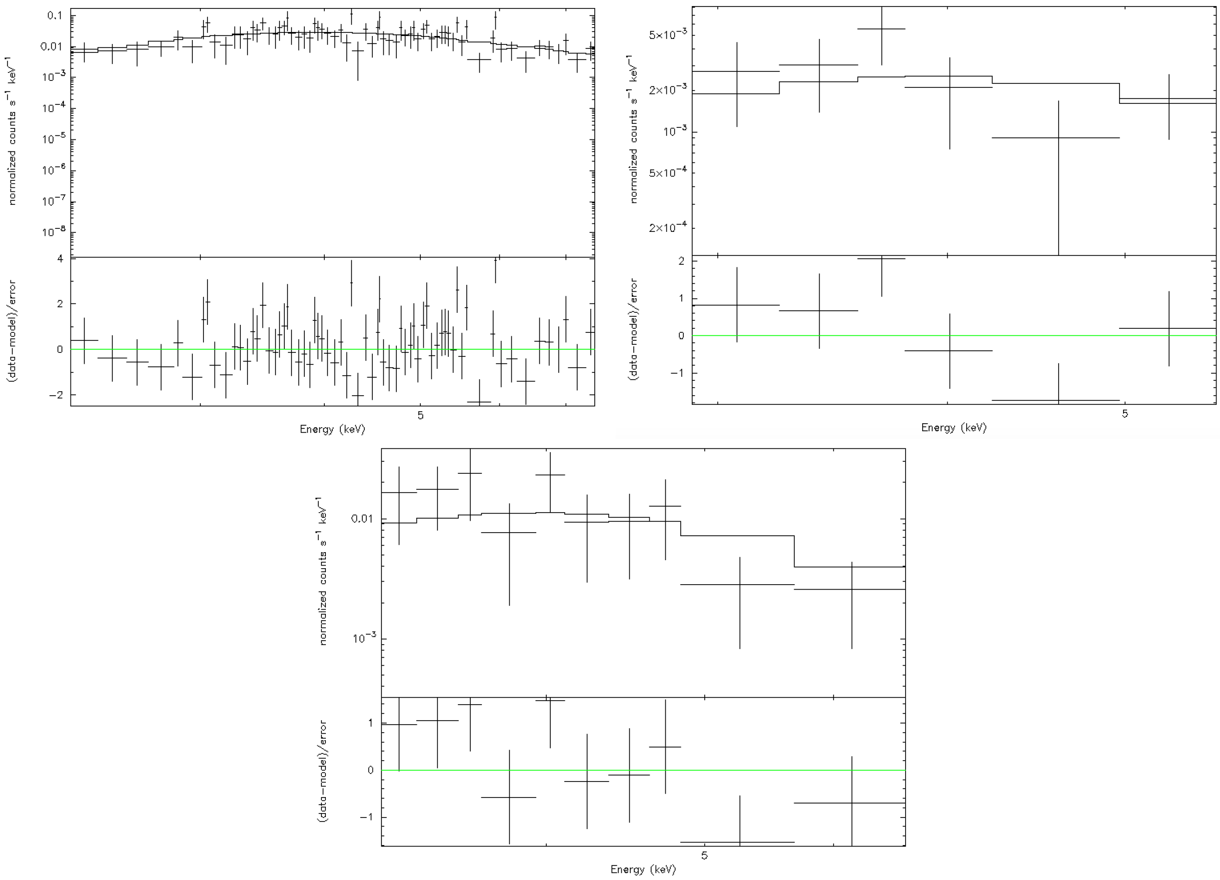

Figure D.2: Chandra spectra in 2017. They are shown by order of flare arrival from the left to the right and from the top to the bottom. The bottom part of each panel represents the residuals between the fit and the observational data.

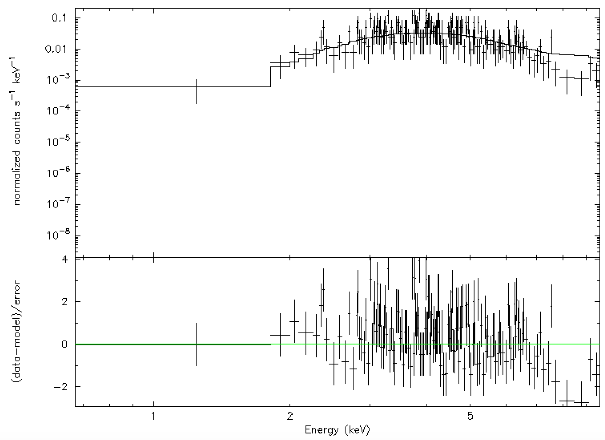

Figure D.3: Chandra spectrum in 2018. The bottom part of the panel represents the residuals between the fit and the observational data.